

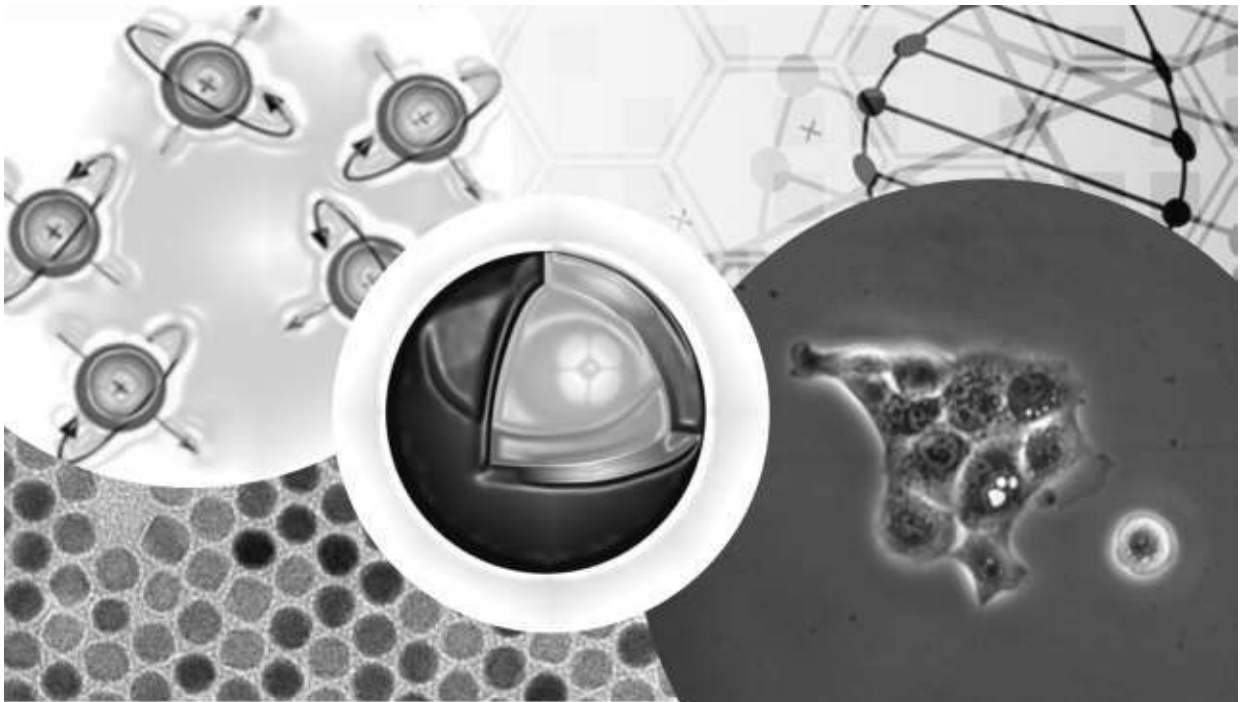
UNIVERSITÀ DEGLI STUDI DI PAVIA  
DOTTORATO DI RICERCA IN FISICA – XXXIII CICLO

---

# Multifunctional modalities of Iron Oxide Magnetic Nanoparticles

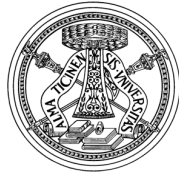
Application in diagnostics and magnetic fluid hyperthermia

Francesca Brero



Tesi per il conseguimento del titolo





UNIVERSITÀ DEGLI STUDI DI PAVIA  
DOTTORATO DI RICERCA IN FISICA – XXXIII CICLO

MULTIFUNCTIONAL MODALITIES OF  
IRON OXIDE MAGNETIC  
NANOPARTICLES

APPLICATIONS IN DIAGNOSTICS AND MAGNETIC FLUID HYPERTHERMIA

FRANCESCA BRERO

Advisors: Prof. Alessandro Lascialfari & Dr. Manuel Mariani

Submitted to the Graduate School of Physics  
in partial fulfillment of the requirements for the degree of  
DOTTORE DI RICERCA IN FISICA  
DOCTOR OF PHILOSOPHY IN PHYSICS  
at the  
University of Pavia

COVER:

*Pictorial representation of the techniques this work is based upon.*

Top left: scheme for nuclear magnetic resonance; right: graphical rendition of a sample DNA double helix under observation for damage caused by hyperthermia and/or exposition to a hadron flux; bottom left: TEM picture of spherical iron oxide magnetic nanoparticles; bottom right: nanoparticles injected in the cells employed in this work.

TITLE:

*Multifunctional modalities of iron oxide magnetic nanoparticles:  
applications in diagnostics and magnetic fluid hyperthermia*

AUTHOR:

Francesca Brero

PhD Thesis – Università degli Studi di Pavia  
Pavia, Italy, June 2021



Non sempre le nuvole offuscano il cielo: a volte lo illuminano.

— Elsa Morante, *La storia*



---

## ABSTRACT

---

This PhD thesis, *Multifunctional modalities of iron oxide magnetic nanoparticles: applications in diagnostics and magnetic fluid hyperthermia*, has two major purposes. The first goal is to assess the anti-tumor efficacy and the potential of combining Hadron Therapy and Magnetic Fluid Hyperthermia (MFH) against pancreatic tumor cells; this is carried out with a perspective to establishing solid protocols for desirable future clinical applications. The second goal is to evaluate the Magnetic Resonance Imaging (MRI) image contrast efficiency of magnetic nanoparticles. This is accomplished by means of  $^1\text{H}$  Nuclear Magnetic Resonance relaxometry, magnetometry and morpho-dimensional characterization techniques, with a particular focus on the effect of size and coating. Data for this research were collected thanks to cross-collaborations between national and international research groups and hospital structures.

For the MFH therapy, the properties of the magnetic nanoparticles that were employed have been optimized in order to maximize their heat release, and, at the same time, to give the patient an amount of magnetic material as low as possible, thus reducing any risk of detrimental side effects to his health. Cell culture conditions and hyperthermic treatment (partly of magnetic origin) were optimized to maximize the efficacy of the therapy, with the aim of decreasing the survival of cancer cells. Given the advantages of hadron therapy over conventional radiotherapy, it was decided to combine the hyperthermic treatment with the first one. This was possible thanks to the fact that Pavia, where most of the work behind this thesis was performed, hosts a state-of-the-art hadron therapy center, the CNAO foundation. This center is the only one in Italy where cancer patients can be treated with both protons and carbon ions. Two main results can be highlighted from the Clonogenic Survival (CS) data collected at 15 days after the combined therapeutic treatment. Firstly, at all hadrons/photon irradiation doses, an additional killing effect—*i.e.* toxicity—of about 50–60% can be ascribed to the cellular uptake of the nanoparticles, with respect to simple irradiation of culture cells. Secondly, a significant killing effect of hyperthermia was observed for both irradiation protocols, consisting in an additional 15–30% of total survival decrease. The enhanced efficacy of

Hadron Therapy applied immediately after hyperthermia lays the foundations for future preclinical studies. Furthermore, these encouraging results point in the direction of further investigating this combination, with a view to finally translating it to clinical applications.

As to the second goal—*i.e.* the investigation of the properties of magnetic nanoparticles by means of nuclear magnetic resonance relaxometry and magnetometry—this thesis specifically concerned the influence of coating on the nuclear relaxation times. Two sets of samples, each consisting of four samples with different coatings, were obtained by means of the same synthesis procedure, while the nanoparticles coating has been realized with different polymers. A heuristic model for the field dependence of the Nuclear Magnetic Resonance (NMR) relaxivity curves allowed us to evaluate several parameters: among them, the saturation magnetization, the minimum approach distance, etc. Moreover, through the acquisition and analysis of experimental NMR dispersion curves, we observed that the relaxivities  $r_1$  and  $r_2$  of the four samples analyzed, for both sets, did not show significant differences in the whole range of frequencies investigated, at least within the experimental errors. Thus, we concluded that the four different coatings we analyzed on our spherical MNPs give essentially similar magnetic and relaxometric behavior.

---

# CONTENTS

---

List of Figures	xi
Acronyms	xvi
1 INTRODUCTION	1
2 MAGNETISM OF SMALL PARTICLES	7
2.1 Introduction	7
2.2 Coercive Field and Magnetic Behavior	9
2.3 Superparamagnetism	9
2.4 Magnetic Anisotropy	11
2.5 The Stoner–Wohlfarth Theory	12
3 MAGNETIC FLUID HYPERTHERMIA	17
3.1 Introduction	17
3.2 Magnetic Fluid Hyperthermia	18
3.3 Physics of Heating with MNPs	21
3.3.1 Stoner-Wohlfarth theory	21
3.3.2 Linear Response Theory (LRT)	22
3.3.3 Rayleigh Model	23
3.4 Experimental SAR evaluation	25
3.4.1 Intrinsic loss parameter	27
4 NUCLEAR MAGNETIC RESONANCE	29
4.1 Introduction	29
4.2 NMR experiments - Bloch equations	32
4.3 NMR Signal	34
4.4 Nuclear Relaxation Theory in Presence of Superparamagnetic NPs	35
4.5 Theory of Proton Relaxation induced by Superparamagnetic NPs	37
5 HADRON THERAPY AND HYPERTHERMIA	43
5.1 Rationale	43

---

5.2	Conventional Radiotherapy . . . . .	44
5.2.1	Photon-tissue interaction . . . . .	45
5.2.2	Dose distribution . . . . .	46
5.3	Hadron Therapy . . . . .	47
5.3.1	Interaction Mechanisms . . . . .	47
5.4	Biological Effects . . . . .	48
5.5	Advantages of Hadron Therapy . . . . .	52
5.6	Hadron Therapy and Hyperthermia . . . . .	53
5.7	Experimental Treatment Protocol . . . . .	54
5.7.1	Magnetic Nanoparticles - Synthesis and Carachteriza- tion . . . . .	57
5.7.2	BxPC <sub>3</sub> tumor cell line . . . . .	61
5.7.3	Optimization of the experimental setup . . . . .	63
5.8	Conclusions . . . . .	73
6	COATING EFFECTS IN NANOPARTICLES . . . . .	75
6.1	Rationale . . . . .	75
6.2	SPM Nanoparticles: Synthesis and Characterization . . . . .	78
6.2.1	Fabrication Procedure of MNPs . . . . .	78
6.2.2	Morphological Characterization . . . . .	79
6.2.3	Magnetic Characterization . . . . .	82
6.3	<sup>1</sup> H NMR Relaxation . . . . .	83
6.3.1	Fast-Field-Cycling technique . . . . .	84
6.3.2	Longitudinal relaxation time T <sub>1</sub> measurements . . . . .	85
6.3.3	Transverse relaxation time T <sub>2</sub> measurements . . . . .	85
6.3.4	NMRD profiles . . . . .	87
6.4	Conclusions . . . . .	91
	CONCLUSIONS AND PERSPECTIVES . . . . .	95
	LIST OF PUBLICATIONS . . . . .	99
	BIBLIOGRAPHY . . . . .	107

---

## LIST OF FIGURES

---

Figure 1	A representation of the energy of a uniaxial magnetic nanoparticle as a function of the direction of the magnetization with respect to the anisotropy axis in the absence (a) and in the presence (b) of an applied external magnetic field [9]. . . . .	8
Figure 2	Qualitative dependence of the coercivity $H_c$ on the particle diameter $d$ , indicating blocked and superparamagnetic regions below the critical diameter $d_{cr}$ [9]. . . . .	10
Figure 3	Atomic moments of the atoms in a NP are locked together (single <i>giant</i> cluster moment, left side). The moment can be treated as a classical vector (right side), being the energy states of the different $\mu_z$ values form a quasi-continuum [13]. . . . .	11
Figure 4	Schematic representation of a MNP when the magnetization is uniformly defined by collinear spins only (a) and where surface anisotropy is considered (b). . . . .	12
Figure 5	Single-domain ellipsoidal particle in a magnetic field $H$ , showing the relevant angles between this field, the anisotropy axis and the magnetization $\vec{M}$ . . . . .	12
Figure 6	Hysteresis cycle for single-domain particles with uniaxial anisotropy for different values of the $\vartheta$ angle between the magnetic field and the easy axis [14]. . . . .	15
Figure 7	Size scale of nanoparticles compared to other biological structures. . . . .	17
Figure 8	Schematic representation of most of the pathologies treated with iron oxide nanoparticles. Inspired from [15]. . . . .	18
Figure 9	Schematic representation of the MFH treatment. (a) direct injection of MNPs into the tumor. (b) MNP diffusion in tumor cells and not in healthy tissues. (c) MNP uptake by tumor cells. (d) Exposure to an alternating magnetic field in order to reach the desired temperature [8]. . . . .	20

Figure 10	Schematic representation of the models for the SAR of MNPs. The validity ranges of the model are underlined, as a function of the particles diameter and the magneto-thermal quantity $\xi = \mu_0 M_s V H_{\max} / k_B T$ [34, 36]. . . . .	24
Figure 11	Typical heating curves obtained in calorimetric measurements with an adiabatic and a non-adiabatic setup [38]. . . . .	26
Figure 12	Schematic representation of the Zeeman effect in case of hydrogen atom: split of the energy levels when a magnetic field is applied. . . . .	30
Figure 13	(a) The Boltzmann distribution of an ensemble of hydrogen nuclei. In thermal equilibrium the net magnetization $M_0$ is due to the difference in the number of nuclear spins populating energy levels. (b) The net magnetization $M_0$ precesses in the stationary frame around the z axis and it can be split into two components: the transversal magnetization $M_{x,y}$ and the longitudinal magnetization $M_z$ [45].	31
Figure 14	Bloch equations: (a) Recovery of the longitudinal nuclear magnetization $M_z(t)$ with a characteristic relaxation time $T_1$ . (b) Decay of the transversal magnetization $M_{x,y}(t)$ with a characteristic relaxation time $T_2$ . . . . .	34
Figure 15	$^1\text{H}$ relaxation induced by paramagnetic system: (a) Inner Sphere Mechanism. (b) Outer-Sphere mechanism. $\tau_M$ : exchange time, $\tau_R$ : rotational correlation time, $\tau_S$ : electronic spin correlation time, $\tau_D$ : diffusion time. . . . .	36
Figure 16	Superparamagnetic MNPs in water: longitudinal NMR dispersion profile. Both experimental data on magnetite MNPs and the theoretical fit (RMG model) are reported [46].	38
Figure 17	Longitudinal NMRD profile for the $^1\text{H}$ relaxation in the case of a SPM nanoparticle (high anisotropy energy limit), according to Roch's theory. . . . .	39
Figure 18	Photoelectric effect . . . . .	45
Figure 19	Compton effect . . . . .	46
Figure 20	Pair production . . . . .	46
Figure 21	Profile dose vs depth using a photon beam. $D_s$ is the dose at surface, $D_{\text{ex}}$ is the dose at the exit side and $D_{\text{max}}$ the maximum one [53]. . . . .	47
Figure 22	Stopping power of protons and carbon ions as a function of their energy [56]. . . . .	49
Figure 23	The principle of the construction of a Spread Out Bragg Peak (SOBP) in hadron therapy [57]. . . . .	49
Figure 24	Schematic representation of DNA damage produced by x-rays, protons and carbon-ions. [58]. . . . .	50



Figure 25	(a) RBE-LET plot for V79 cells for carbon ions. (b) RBE-LET plot for V79 cells for different particles type [60]. . . . .	51
Figure 26	Linear Quadratic curves in case of high and low $\alpha/\beta$ ratios. High $\alpha/\beta$ : cell killing rate is constant for all doses, low $\alpha/\beta$ : greater killing per unit dose at higher doses [61].	51
Figure 27	The three different treatment modalities employed in the experiments. In mode 1, the clonogenic survival (CS) was determined after simple irradiation; in mode 2, CS was determined after administering MNPs and irradiation; in mode 3, CS was determined after administering MNPs, then performing irradiation and subsequent hyperthermia (Hyp). The acronym DSB corresponds to the breaking of both strands of DNA. . . . .	55
Figure 28	(a) Water phantom used at CNAO for carbon ions irradiation. (b) Synchrotron-based facility at CNAO, in Pavia, Italy. . . . .	56
Figure 29	Powders XRD patterns of $\text{Fe}_3\text{O}_4$ MNP; comparison of diffraction peaks with the reference pattern (red vertical bars) of magnetite (JCPDS 19-0629). . . . .	58
Figure 30	TEM image of magnetite MNPs. Histogram reporting the core size distribution was obtained by TEM statistical analysis, and fitted with a Log-Normal function. . . . .	59
Figure 31	(a) DLS diameter ( $d_{\text{DLS}}$ ) measurements at pH 7.4. (b) Zeta potential measurements at pH 7.4. Three different measurements have been performed (green, blue, red lines). . . . .	60
Figure 32	Hysteresis loop measured at 300 K (left) and 5 K (right), in the field range $\pm 5$ T. In the insets: low field regions. . . . .	61
Figure 33	Schematization of NanoTherics MagneTherm <sup>TM</sup> setup for Magnetic Fluid Hyperthermia experiments. . . . .	64
Figure 34	Representation of the hyperthermia setup. The setup consists of a heat bath, <i>i.e.</i> a thermalization system that circulates water around the two vials where the samples are stored. One of the vials is sterile, and is employed for the clonogenic survival assay and DSBs detection; the second vial is used to register the temperature by means of a optic-fiber probe. . . . .	65
Figure 35	Clonogenic survival of BxPC <sub>3</sub> cells culture for three different mode (see above): hadron therapy only (orange circles), hadron therapy + MNPs (navy blue triangles), hadron therapy + MNPs administration + Hyp (green stars).	67

Figure 36	Clonogenic survival (CS) of BxPC <sub>3</sub> cells both incubating and non incubating MNPs, exposed to photon irradiation in the energy range 0–7 Gy, either combined or not-combined with hyperthermia. . . . .	68
Figure 37	Evaluation of relative biological effectiveness (RBE) for carbon ions. In red, the CS versus Dose profile obtained with photon irradiation; in blue, the one for carbon ions. . . . .	70
Figure 38	Analysis of 53BP1 and $\gamma$ -H2AX foci induction after 6 and 24 hours from the exposure to 0.75 and 1.5 Gy of carbon-ions alone (a) and in combination with MNPs uptake and/or Hyp in BxPC <sub>3</sub> pancreatic tumor cells (b). . . . .	72
Figure 39	Structures of the investigated MNPs as a function of their core diameter and polyelectrolyte coating, depicted as PAA-A (poly(methacrylic acid)), PEG-B (PMAA-g-PEG <sub>2000</sub> ), PEG-C and PEG-D (P(MAA-stat-MAPEG <sub>2000</sub> ) with two different transfer agent). . . . .	78
Figure 40	Core-size distribution associated to the two nanoparticle series investigated as obtained by TEM (A-8 on the right and A-17 on the left). A log-normal function was used to fit the results; the mean and the standard deviation can be found in Table 6. . . . .	80
Figure 42	Representative images of sample A-17 obtained by means of bright field TEM. . . . .	81
Figure 42	a) ZFC/FC magnetization curves collected with a magnetic field $\mu_0 H = 5 \cdot 10^{-3}$ T and (b) low field hysteresis loops at 2.5 K for A-17 and A-8. . . . .	83
Figure 43	Magnetization curves at 2.5 K (left panel) and 300 K (right panel) for the first series. Details at low magnetic fields are shown in the insets. . . . .	83
Figure 44	Pre-polarized Spin Echo sequence for low field T <sub>2</sub> measurements with Fast-Field Cycling technique. . . . .	84
Figure 45	Saturation Recovery sequence for T <sub>1</sub> measurements. . . . .	85
Figure 46	Carr-Purcell-Meiboom-Gill sequence for T <sub>2</sub> measurements. This sequence includes a first $\pi/2$ pulse, followed by a train of $\pi$ pulses. The signal follows an exponential decay law with a typical time T <sub>2</sub> - see Eq. (81). . . . .	87
Figure 47	NMRD profiles collected at room temperature for the first series (17 nm) of polymer-coated MNPs, with the Larmor frequency ranging between $0.01 \leq \nu_L \leq 60$ MHz: longitudinal $r_1$ (a) and transverse $r_2$ (b). As a reference, the relaxivity values of Endorem reported by Basini et al. are shown [116]. . . . .	88

Figure 48	NMRD profiles collected at room temperature for the second series (8 nm) of polymer-coated MNPs, with the Larmor frequency ranging between $0.01 \leq \nu_L \leq 60$ MHz: longitudinal $r_1$ (a) and transverse $r_2$ (b). As a reference, the relaxivity values of Endorem reported by Basini et al. are shown [116]. . . . .	90
Figure 49	Room-temperature NMRD longitudinal $r_1$ profiles for the 8 nm series of polymer-coated MNPs; different samples are shown as different symbols. The Larmor frequencies vary in the range $0.01 \leq \nu_L \leq 60$ MHz. The best fits given by the application of Roch's model are shown as solid-line curves. . . . .	92

---

## ACRONYMS

---

**AFM** Atomic Force Microscopy

**AMF** Alternating Magnetic Field

**CA** Contrast Agent

**CNAO** National Centre for Oncological Hadron Therapy

**CS** Clonogenic Survival

**DLS** Dynamic Light Scattering

**DMSA** meso 2, 3-dimercaptosuccinic acid

**DMSO** Dimethyl Sulfoxide

**DSB** Double Strand Break

**FID** Free Induction Decay

**FM** ferromagnetic

**HT** Hadron Therapy

**HYP** Hyperthermia

**ILP** Intrinsic Loss Parameter

**INFN** Italian National Institute for Nuclear Physics

**INT** National Institute of Tumours

**LET** Linear Energy Transfer

**LRT** Linear Response Theory

**LQ** Linear Quadratic

<b>MFH</b>	Magnetic Fluid Hyperthermia
<b>MNP</b>	Magnetic Nanoparticle
<b>MRI</b>	Magnetic Resonance Imaging
<b>NMR</b>	Nuclear Magnetic Resonance
<b>NP</b>	nanoparticle
<b>OA</b>	Oleic Acid
<b>PE</b>	Plating Efficiency
<b>PEG</b>	Polyethylene Glycol
<b>RBE</b>	Relative Biological Effectiveness
<b>RMG</b>	Roch-Muller-Gillis
<b>RT</b>	Radiotherapy
<b>SAR</b>	Specific Absorption Rate
<b>SOBP</b>	Spread Out Bragg Peak
<b>SPION</b>	Superparamagnetic Iron Oxide Nanoparticle
<b>SPM</b>	Superparamagnetism
<b>SQUID</b>	Superconducting Quantum Interference device
<b>SSB</b>	Single Strand Break
<b>SW</b>	Stoner-Wohlfarth
<b>TEM</b>	Transmission Electron Microscopy
<b>USPIO</b>	Ultrasmall Superparamagnetic Iron Oxide
<b>XRD</b>	X-ray Diffraction



# 1

---

## INTRODUCTION

---

A comprehensive list of possible nanomaterials applications should include electronics, technology, nanomedicine, chemical industry, optics, aviation, cosmetics, and space science [1].

As far as the biomedical applications are concerned, the last decades have seen huge advances in the synthesis of Magnetic Nanoparticles (MNPs) whose applications come with strict requisites on their size, surface and colloidal stability; all these features can be tailor-made according to the different applications for which they can be used. Under certain conditions, MNPs are already applied in clinics, as is the case of Magnetic Resonance Imaging (MRI) Contrast Agents (CAs), or Magnetic Fluid Hyperthermia (MFH) treatments [2, 3]. However, for other purposes, *e.g.* tissue regeneration or drug delivery, the use of nanoparticles (NPs) in an effective and biocompatible way is not fully evaluated yet. The impediment in most cases is due to the wide particles' size distribution, the scarcity of aggregation control, the poor/weak functionality of the NP surface, the protein-corona effect which depends on physico-chemical properties of the NPs, the rapid sequester of NPs by macrophages once they are injected into the body. The most used nanomaterials in biomedical applications are the iron oxide-based ones, among which magnetite and maghemite are by far the two most commonly studied. MNPs are nanosized tools, mainly ranging from few nanometers up to tens of nanometers, whose magnetic properties make them versatile and effective, both in diagnostics and therapeutics. Since *in vivo* applications are the ultimate purpose, MNPs are generally synthesized with a core-shell structure: the magnetic core is surrounded by an organic coating, *i.e.* a biocompatible organic medium, whose aim is to avoid the uptake by the reticular endothelial system, to guarantee biocompatibility and colloidal stability minimizing the inter-particle interactions, to increase cell penetration, to perform drug delivery, and, in some cases, thanks to the the high surface to volume ratio, to functionalize the NPs with drugs/ligands to endow them with site specificity. The magnetic properties of NPs are affected by many factors, *e.g.* the degree of disper-

sion/aggregation, the strength of inter-particle interactions, the surface of the NP, features of the synthesis method, etc. All these features enable their application for theranostics, *i.e.* the use of a single object to pursue a combination of goals: identifying/diagnosing and delivering a therapy [4, 5]. In particular, because of their high magnetization and superparamagnetic behaviour, iron oxide-based MNPs can be employed as contrast agents for MRI and heat-mediators for MFH. Since MRI does not expose patients to ionizing radiations and their potentially harmful side-effects, it has become a helpful tool to acquire anatomy images safely. The only drawback, besides high costs, is its low sensitivity, which ultimately leads to poor resolution, contrast and long scan times. Contrast agents reduce the longitudinal ( $T_1$ ) and transverse ( $T_2$ ) relaxation times of the water protons in the region where they accumulate, which is generally a lesion, allowing its better detection in the MR image. Although the potential effectiveness of CAs appears endless in laboratory research, only a small percentage of synthesized MNPs has been approved for clinical use. The U.S. Food and Drug Administration and the European Medicines Agency, which adopts contrast agents for clinical use, indeed, rightly requires evidence of safety - including pharmacology, absorption, distribution, metabolism, toxicity - and efficacy. The majority of the iron oxide-based CAs that were approved in the past, are now withdrawn from the market; nevertheless, *Feraheme* is used for treat the iron deficiency in patients affected by chronic kidney failure, and the selling of *Resovist* is still allowed in few countries [6, 7]. As to the therapeutic purposes, MNPs can be exploited as heat mediators in magnetic fluid hyperthermia. When injected into the tumors and exposed to an Alternating Magnetic Field (AMF) whose amplitude is in the order of tens of mTesla and whose frequency amounts to some hundreds of kHz, they release heat in the surrounding environment, because of the interaction between the field and their magnetization. In the therapeutic window 40–44 °C, MFH has an anti-tumor effect: these temperatures kill cancer cells by damaging their fundamental structures, such as the membrane, the organelles, and the DNA. As a consequence, cancer patients receiving MFH treatment and chemotherapy/radiotherapy or surgery have a better life expectancy. To date, MFH is employed in clinics by the German company MagForce for glioblastomas, prostate cancers and poor-prognosis tumor therapy [8]. Although MFH offers a better control of energy deposition in the tumors by heating only the vicinity of particles, when compared to other hypertermic treatment, one of the main issues is the unwanted formation of hot spots in the targeted area due to a non homogeneous MNPs distribution. Moreover, large amounts of particles have to be injected into the tumor to reach the therapeutic goal (ca. 50 mg per cm<sup>3</sup> of target volume). Many improvements are therefore necessary before reaching a wide clinical use of MNPs, *e.g.* an increased Specific Absorption Rate (SAR), an



increased cellular uptake, a diminution of the dose/concentration, and so forth.

This thesis focuses on the multifunctional modalities of iron oxide magnetic nanoparticles; in particular, two main topics are investigated: (i) the effects of the size/coating of spherical MNPs on their relaxometric efficiencies; (ii) the efficacy of magnetite MNPs as heat mediators in magnetic fluid hyperthermia, combined with hadron therapy on pancreatic cancer cells. An overview of the thesis content and structure is given in the next paragraph.

### THESIS OVERVIEW

In Chapter 1, the physical laws governing magnetism in MNPs are presented, with a focus on the superparamagnetism phenomenon and the magnetic anisotropy of particles. The Stoner-Wohlfarth theory, describing the magnetic behavior of a single domain NP is described. Moreover, the dependence of the magnetic behavior on the MNPs size deserves to be highlighted.

In Chapter 2, the physical mechanisms of magnetic nanoparticle-mediated hyperthermia are presented. An aspect on which particular stress will be laid is that of the theoretical models available to date in the scientific literature for describing the SAR trend as a function of the MNP features and field parameters. Furthermore, a section is dedicated to the experimental procedure suitable for the SAR evaluation, flanked by an excursus on the method available in literature to extract SAR values from the temperature vs field's time application curve.

Chapter 3 focuses on nuclear magnetic resonance (NMR). Physical principles of NMR are summarised, both with classical and quantum approaches. The Bloch equations will be recalled: they describe the evolution of the nuclear magnetization after a pulse as a function of time accounting for relaxation; the meanings of the longitudinal relaxation time  $T_1$  and the transverse relaxation time  $T_2$  will be explained. In addition, nuclear relaxation theory in presence of superparamagnetic nanoparticles and the Roch-Muller-Gillis (RMG) theory of proton relaxation are presented, as they allow the description of nuclear magnetic resonance dispersion profiles.

Chapter 4 deals with the results of the INFN Hadromag project, whose main goal was to assess the anti-tumor efficacy of a combined action of two therapeutic techniques: Hadron Therapy (HT) and MNP-mediated hyperthermia. An overview of the different types and biological effects of radiation therapies is provided in the first part of the chapter, *i.e.* conventional Radiotherapy (RT), which makes use of photon beams, and hadron therapy, which exploits protons and carbon ions beams. Since 2017, HT has become part of the Italian Basic Benefit Package provided by the Ital-

ian National Health System, and it offers several advantages with respect to RT, thanks to the particular physical properties of the particles used. In the second part, the effects of the combination of HT, MNP administration and hyperthermia treatment on *in vitro* pancreatic cancer cells (BxPC<sub>3</sub>) are reported. MNPs used as heat mediators during the hyperthermic treatment—*i.e.* thirty minutes at  $T = 42\text{ }^{\circ}\text{C}$  under the application of an alternating magnetic field with frequency  $f = 109.8\text{ kHz}$ , and amplitude  $H = 19.5\text{ mT}$ —have a magnetite core ( $\text{Fe}_3\text{O}_4$ ) with mean diameter of 19 nm coated with meso 2, 3-dimercaptosuccinic acid (DMSA), a biocompatible ligand that ensures stability in physiological media, and are characterized by a specific absorption rate equal to  $110 \pm 30\text{ W/g}_{\text{Fe}_3\text{O}_4}$ . The radiation doses that were employed are 0–2 Gy for carbon ions (National Center for Oncological Hadron Therapy facility in Pavia, Italy) and 0–7 Gy for 6 MV photons (Istituto Nazionale dei Tumori in Milan, Italy), which are used for a comparison with conventional RT. The biological effect of the treatment is assessed by means of two methods: firstly, a clonogenic assay is performed after two weeks to evaluate the cells' ability to give rise to a viable colony of at least 50 cells; secondly, the amount of non-repairable Double Strand Breaks (DSBs) per cell is evaluated after both 6 and 24 h; this is achieved by detecting and counting persistent repair foci, which are the signature of DSBs. The clonogenic-survival results show an increase in the efficacy of hadron therapy when combined with hyperthermia, applied immediately afterwards. This lays the foundations for perspective preclinical studies. Furthermore, these encouraging results call for further investigations on this combined technique, with a view to finally translating it into a clinical application.

Finally, in Chapter 5 we investigate the dependence of the Magnetic Resonance Imaging contrast efficiency—*i.e.* the nuclear relaxivity—on the organic coating shield by means of NMR relaxometry. More specifically, two series of magnetic nanoparticles are studied, consisting of a maghemite core with a mean diameter  $d_{\text{TEM}} = 17 \pm 2.5\text{ nm}$  and  $8 \pm 0.4\text{ nm}$ , respectively, and coated with four different negative polyelectrolytes. The first half of the chapter focuses on the synthesis of MNPs and their characterization; this is achieved by means of different techniques, such as Transmission Electron Microscopy (TEM), Atomic Force Microscopy (AFM), Superconducting Quantum Interference device (SQUID) magnetometry, and Dynamic Light Scattering (DLS) method, so as to have a proper overview of the significant properties of the MNPs one may wish to compare against the NMR results. In the second half, we show the experimental procedure used to obtain the nuclear magnetic resonance dispersion (NMRD) profiles, *i.e.* the longitudinal ( $r_1$ ) and the transversal ( $r_2$ ) relaxivities as a function of the magnetic field  $0.2\text{ mT} < \mu_0 H_0 < 1.41\text{ T}$ . The Fast-Field-Cycling technique for measurements at low field is presented and the sequences used

to evaluate  $T_1$  and  $T_2$  are described. The NMRD profiles collected at room temperature for all samples are analyzed and the behavior is commented on the basis of the size and magnetic properties. For each series,  $^1\text{H}$  NMR relaxivities is found to depend very slightly on the surface coating. Higher  $r_2$  values are observed, at all investigated frequencies, for the series associated to the larger diameter, together with a very different frequency behavior for  $r_1$  between the two series. In particular, the first one ( $d_{\text{TEM}} = 17 \text{ nm}$ ) displays an anomalous increase of  $r_1$  towards the lowest frequencies, possibly due to high magnetic anisotropy together with spin disorder effects. The other series ( $d_{\text{TEM}} = 8 \text{ nm}$ ) displayed a  $r_1$  vs  $\nu_L$  behavior that can be described according to Roch's heuristic model. The fitting procedure provided the distance of minimum approach and the value of the Néel reversal time at room temperature; the latter confirmed the superparamagnetic nature of these compounds.



# 2

---

## MAGNETISM OF SMALL PARTICLES

---

**M**AGNETIC nanoparticles (MNP) are a class of nanotechnology-based materials whose applications range from biomedical engineering to magnetic storage and sensing, nanomedicine, and many more. Their size can be employed to tailor a variety of different features, such as their magnetic response, their surface area, etc. In particular, MNPs spin configuration can be single-domain, or multi-domain, with consequent variation in their magnetic behavior. Moreover, the phenomenon of *superparamagnetism* occurs with nanoparticles in the smaller range of diameters, allowing the NPs magnetization to randomly flip direction under the influence of thermal energy. In this chapter the *Stoner–Wohlfarth theory* is presented.

### 2.1 INTRODUCTION

The magnetic behavior of MNPs is strongly dependent on their size. When the size of the particle is small, its constituent magnetic moments are aligned along a single direction; if, however, the size is larger, *i.e.*  $d > d_{cr}$  for a certain critical diameter  $d_{cr}$ , the minimization of dipolar energy causes magnetic domains to form inside the particle (multi-domain configuration). As the size of the MNP decreases further, the magnetic energy becomes of the order of the thermal energy ( $k_B T$ ) or even smaller. In this scenario, the magnetization direction can fluctuate. This state is called *superparamagnetism* by analogy with classical paramagnetism, *i.e.* disordered state of magnetic atoms. The transition from the superparamagnetic state to the blocked one (that happens when temperature is decrease and it depends also on the value of the applied magnetic field) depends on the local anisotropies of the particles and on the strength of the local magnetization.

Nanoparticles are usually assumed to have a uniaxial magneto-crystalline anisotropy (even though in general terms is not the only case) given by:

$$E_B = K_u V \sin^2 \vartheta, \quad (1)$$

where  $K_u$  is the magnetic anisotropy constant,  $\vartheta$  is the angle among the magnetization direction and the anisotropy axis (easy axis) and  $V$  the particle volume. The origin of this  $E_B$  term is the spin-orbit interaction and has two minima, at  $\vartheta = 0$  and  $\vartheta = \pi$ , separated by an energy barrier  $K_u V$  (see Fig. 1).

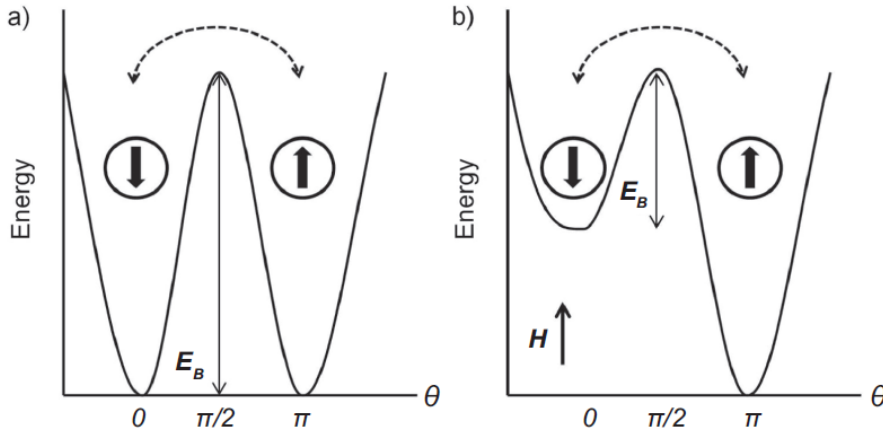


**Figure 1:** A representation of the energy of a uniaxial magnetic nanoparticle as a function of the direction of the magnetization with respect to the anisotropy axis in the absence (a) and in the presence (b) of an applied external magnetic field [9].

As the magnetic-field intensity ( $H$ ) is increased, the shape of the Energy vs  $\vartheta$  curve changes, from symmetric with two minima ( $H = 0$ ) to asymmetric with one single minimum for  $\vartheta = \pi$ .

Below a defined diameter, the nanoparticles become single-domain. Single-domain magnetic particles with diameter less than or equal to a critical length  $d_{spm}$ , have the magnetization vector that jumps between two possible orientations, being the thermal energy ( $k_B T$ ) comparable to the height of the potential barrier  $E_B$  (superparamagnetism). On one hand, particles with a diameter greater than  $d_{spm}$  (but still single-domain) will have a stable direction of magnetization, whose behavior is described by the Stoner-Wohlfarth model. Individual magnetic moments turn through the action of the magnetic field (*Néel rotation*) regardless of the orientation of the whole particle. On the other hand, a different phenomenon called *Brown rotation* can be observed when considering small particles that are free to rotate as a whole, *e.g.* particles in suspension in a fluid [10].

**Table 1:** Critical diameter  $d_{cr}$  for Fe, Co, Ni,  $\gamma$ -Fe<sub>2</sub>O<sub>3</sub> and Fe<sub>3</sub>O<sub>4</sub> [11].

	$d_{cr}$ (nm)
Fe	14
Co	70
Ni	55
$\gamma$ -Fe <sub>2</sub> O <sub>3</sub>	166
Fe <sub>3</sub> O <sub>4</sub>	128

The critical radius  $r_{cr}$ , defined as the length below which the nanoparticle undergoes a transition from multidomain to single domain, for a NP with uniaxial anisotropy  $K_u$  is

$$r_{cr} = \frac{9\pi\sqrt{AK_u}}{\mu_0 M_s^2}, \quad (2)$$

where  $A$  is the exchange stiffness constant ( $J \cdot m^{-1}$ ) and  $M_s$  is the saturation magnetization. Typical values of  $r_{cr}$  are reported in Table 1.

Finally, the multidomain configuration is typical of the largest particles ( $r > r_c$  and/or  $d > d_{spm}$ ), where a variation in the magnetization is due to a reorganization of the domain structure (motion of the magnetic domain walls, or changes in their shape).

## 2.2 COERCIVE FIELD AND MAGNETIC BEHAVIOR

The coercivity ( $H_c$ ), *i.e.* the applied field required to reduce the total magnetization to zero, depends on the size of the MNPs. It's possible to distinguish three main regions (Fig. 2):

- $d < d_{spm}$ : the magnetic moment thermally fluctuates,  $H_c = 0$ ;
- $d_{spm} < d < d_{cr}$ : the magnetic moment is stable, the particle is single-domain and the coercivity increases with  $d$ .
- $d > d_{cr}$ : the particle is in multi-domain regime and  $H_c$  decreases with increasing diameter.

## 2.3 SUPERPARAMAGNETISM

Superparamagnetism (SPM) is a possible result of the competition between the magnetic energy ( $KV$ ) trying to align the particle magnetic moments

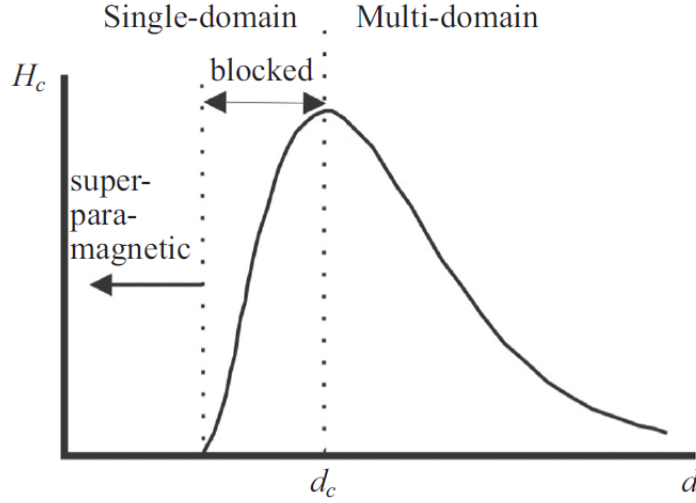


Figure 2: Qualitative dependence of the coercivity  $H_c$  on the particle diameter  $d$ , indicating blocked and superparamagnetic regions below the critical diameter  $d_{cr}$  [9].

with the applied field and thermal fluctuations ( $k_B T$ ) that tend to demagnetize them. If we consider an ideal system, where the nanoparticles are non-interacting, the characteristic relaxation of the magnetization (*i.e.* the reversal time) time is the Néel time, given by the Néel–Arrhenius expression [12]

$$\tau = \tau_0 e^{\frac{E_B}{k_B T}}, \quad (3)$$

where  $\tau_0$  is the inverse of the *attempt frequency*, and it's usually in the range  $10^{-12}$ – $10^{-9}$  s. For  $k_B T \gg KV$ , a system of superparamagnetic nanoparticles behaves as a paramagnet, where instead of considering the single magnetic moments of the atoms in the paramagnet one should consider the giant spins of each nanoparticle. A peculiar trait of superparamagnetism is the presence of a closed hysteresis loop in the magnetization curve. As in the case of paramagnets, the field dependence of the superspins' magnetization of a MNPs system in SPM regime can be described by means of the *Langevin function*.

The total angular momentum quantum number for the cluster is very large compared with an atom and so the quantized states for the whole nanoparticle form a quasi-continuum with tiny increments between the allowed pointing directions. The average magnetic moment per particle along the field direction is given by

$$\bar{\mu} = \mu \langle \cos \vartheta \rangle = \mu L(x), \quad (4)$$



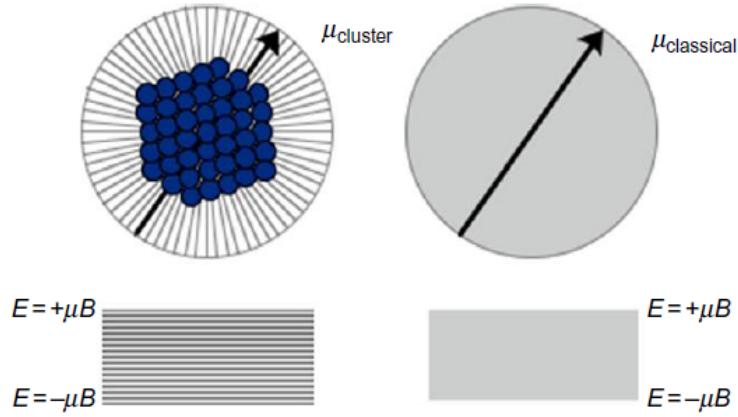


Figure 3: Atomic moments of the atoms in a NP are locked together (single *giant* cluster moment, left side). The moment can be treated as a classical vector (right side), being the energy states of the different  $\mu_z$  values form a quasi-continuum [13].

where  $\vartheta$  varies between 0 and  $\pi$ , and  $L(x)$  is the Langevin function, which describes the magnetization of small particles formed of clusters of atoms,

$$L(x) = \coth(x) - \frac{1}{x} \quad (5)$$

$$\text{and } x = \frac{\mu H}{k_B T}.$$

## 2.4 MAGNETIC ANISOTROPY

As shown in Section 2.1 the magnetic anisotropy of magnetic nanoparticles is commonly assumed as uniaxial. Due to their small size, both the surface anisotropy and the shape anisotropy need to be considered as additive terms. The latter becomes relevant for anisotropic nanoparticles, and its contribution to the total anisotropy, for some kind of MNP shapes, is the dominant one.

The surface anisotropy is due to the translational symmetry breaking on the MNP surface, which causes lattice distortion and moves the spins in non-equilibrium states (see Fig. 4); thus, another term appears in the total amount of anisotropy energy [10]:

$$\mathcal{H} = K_s S_{\perp}^2, \quad (6)$$

where  $S_{\perp}$  is the perpendicular component of the spin and  $K_s$  the surface anisotropy. For spherical particles, with diameter  $d$ , an effective anisotropy

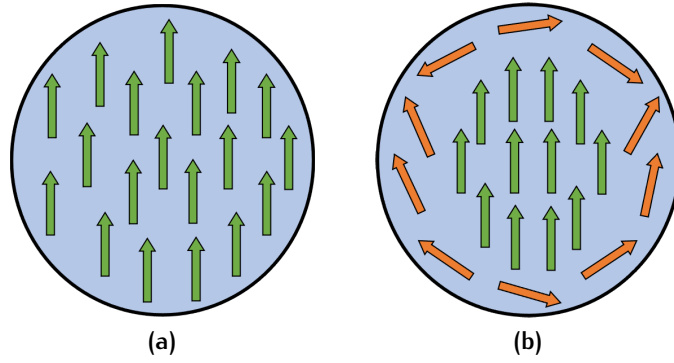


Figure 4: Schematic representation of a MNP when the magnetization is uniformly defined by collinear spins only (a) and where surface anisotropy is considered (b).

constant is generally defined according to

$$K_{\text{eff}} = K_{\text{vol}} + 6 \frac{K_s}{d}, \quad (7)$$

where  $K_{\text{vol}}$  is the bulk anisotropy constant of the core and  $K_s$  is the surface anisotropy constant. The effective anisotropy of a small NP scales as  $d^{-1}$ , increasing as its diameter is reduced.

## 2.5 THE STONER–WOHLFARTH THEORY

The model developed in 1948 by Stoner and Wohlfarth considers the single-domain MNPs with the shape of elongated ellipsoids (Fig. 5). All multi-

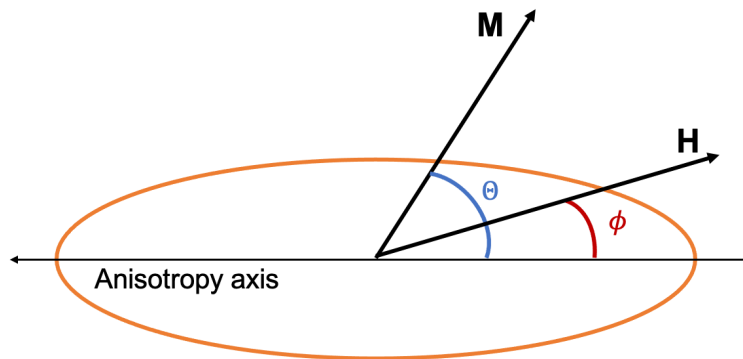


Figure 5: Single-domain ellipsoidal particle in a magnetic field  $H$ , showing the relevant angles between this field, the anisotropy axis and the magnetization  $\vec{M}$ .

domain related effects, non-uniformities or inhomogeneities are not considered. At  $T = 0$ , the total energy of the ellipsoid when  $H \neq 0$  is:

$$E = E_A + E_Z = KV \sin^2 \vartheta - \mu_0 H V M_s \cos(\vartheta - \varphi), \quad (8)$$

where

$E_A$ : anisotropy energy,

$E_Z$ : Zeeman Energy  $= -\vec{M} \cdot \vec{H}$ ,

$\vartheta$ : angle between the magnetization and the easy axis,

$\varphi$ : angle between the field and the direction of easy magnetization z-axis.

By adding the demagnetization energy ( $2\pi N_{i,j} M_i M_j$ ) to the anisotropy contribution, the total energy can be written as

$$E = K_{\text{eff}} V \sin^2 \vartheta - \mu_0 M_s V H \cos(\vartheta - \varphi), \quad (9)$$

where  $K_{\text{eff}} = [K + 2\pi M_s^2 (N_{\parallel} - N_{\perp})]$ ,  $N_{\parallel}$  and  $N_{\perp}$  being the demagnetization coefficients parallel and perpendicular to the z-axis, respectively. The minimum condition at  $\vartheta^*$  is

$$\left( \frac{\partial E}{\partial \vartheta} \right)_{\vartheta=\vartheta^*} = 0 \quad \text{and} \quad \left( \frac{\partial^2 E}{\partial \vartheta^2} \right)_{\vartheta=\vartheta^*} > 0, \quad (10)$$

so that

$$[2KV \sin \vartheta \cos \vartheta - \mu_0 M_s V H \sin(\vartheta - \varphi)]_{\vartheta=\vartheta^*} = 0, \quad (11)$$

$$[2KV \cos(2 \cdot \vartheta) - \cos(\vartheta - \varphi)]_{\vartheta=\vartheta^*} > 0. \quad (12)$$

If the field is applied perpendicularly to the easy axis, *i.e.*  $\varphi = \pi/2$ ,  $\sin(\vartheta - \varphi) = \cos \vartheta$ , then from the Eq. (11), it is possible to get  $H_K$ , namely the value of the field  $H$  for which  $\vartheta = \pi/2$ , called anisotropy field:

$$H_K = \frac{2K \sin \vartheta}{\mu_0 M_s} = \frac{2K}{\mu_0 M_s}. \quad (13)$$

If the magnetic field is applied along the same direction as the easy axis but in the opposite direction to the magnetic moment of the particle, which is initially at the  $\vartheta = 0$  position, we have  $\sin(\varphi - \vartheta) = \sin \vartheta$ , and from Eq. (11) we can deduce that the minimum value of the energy can be obtained for  $\vartheta = \pi$ , *i.e.* for the condition in which the superspin lies on the easy axis with the direction coinciding with the external field. When a particle starts with magnetization initially at  $\vartheta = 0$ , it is instead in the second minimum. The minimum is not absolute due to the asymmetry of the two minima. As

mentioned, the asymmetry between the two minima occurs in the presence of an external field, and the energy is

$$E_{\min} = \mu_0 M_s H. \quad (14)$$

To determine the maximum value of the particle energy, it is necessary to evaluate Eq. (8) for  $\vartheta = \pi/2$ , and with some substitutions we obtain:

$$E_{\max} = KV \left( 1 + \frac{\mu_0^2 M_s^2 H^2}{4K^2} \right). \quad (15)$$

The height of the energy barrier, that the superspin of the particle must cross to orient itself with the external field parallel or anti-parallel to the easy axis, can thus be calculated simply as the difference between the maximum and the minimum energy of the particle:

$$E_B = E_{\max} - E_{\min} = KV \left( 1 + \frac{\mu_0^2 M_s^2 H^2}{4K^2} - \frac{\mu_0 M_s H}{K} \right). \quad (16)$$

By replacing the value of the  $H_K$  anisotropy field found in Eq. (13), the expression is reduced to the simple form:

$$E_B = Kv \left( 1 - \frac{H}{H_K} \right)^2. \quad (17)$$

As it is apparent that this barrier energy value is valid only for  $\vartheta = \pi$ , as seen from the simplifications made during the different steps of the calculation. The equation can be generalized in the following approximate form:

$$E_B = E_B^0 \left( 1 - \frac{H}{H_{sw}^0} \right)^k, \quad (18)$$

where  $k$  is a phenomenological parameter that depends on the  $\vartheta$  angle and  $H_{sw}^0$  is the inversion field at zero temperature that representing the minimum field for which the energy barrier disappears at zero temperature and the magnetization reverses its orientation. For  $\vartheta = \pi$  we have  $k = 2$ , as found in Eq. (17), whereas for small values of  $\vartheta$  (of a few degrees)  $k = 1.5$ . For large  $\vartheta$  angles, no simple analytical expression for the energy barrier can be derived.

The amplitude of the angle  $\vartheta$  affects the shape of the hysteresis loop of the particle system. This effect is shown in Fig. 6 for different values of  $\vartheta$ , where  $h$  represents the reduced magnetic field  $h = H/H_K$  and  $m$  the normalized magnetization  $m = M/M_s$ . For  $\vartheta = 0$ , we have  $H_c = H_K$  and the hysteresis cycle has a maximum area, but a misalignment of 20%

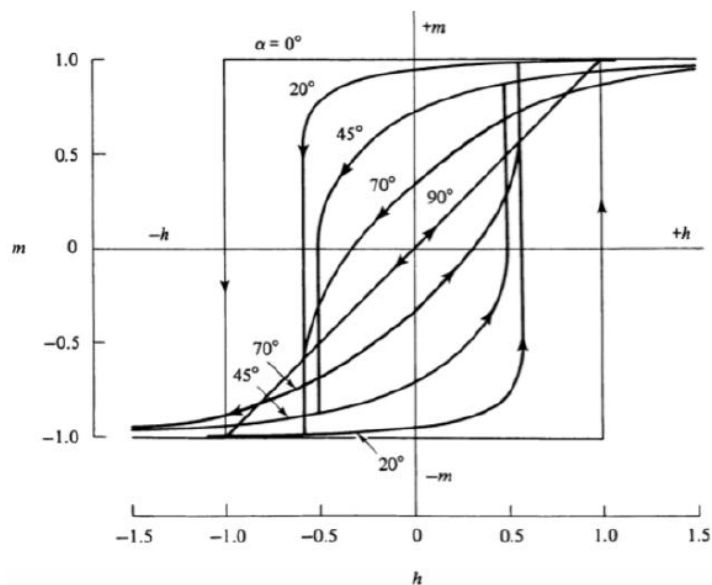


**Figure 6:** Hysteresis cycle for single-domain particles with uniaxial anisotropy for different values of the  $\vartheta$  angle between the magnetic field and the easy axis [14].

between the field and the easy axis is sufficient to cause a 30% reduction in the value of the coercive field  $H_c$ .



# 3

## MAGNETIC FLUID HYPERTHERMIA

IN this Chapter, the Magnetic Fluid Hyperthermia technique will be presented, with particular attention to the physical mechanisms of heating, to the definition of the MNP's Specific Absorption Rate (SAR) and to the theoretical models (*i.e.* *Linear Response Theory*, *Stoner–Wohlfarth* and *Rayleigh*) that describe the behaviour of the SAR as a function of the diameter of the magnetic nanoparticles and their magnetic configuration.

### 3.1 INTRODUCTION

Magnetic nanoparticles are being extensively studied especially for their potential applications in nanomedicine. Their sizes typically range from 1 to 100 nm and the number of atoms they consist of varies from a few hundreds to about  $10^5$  atoms. This allows the nanoparticles to have a good interaction with biological structures (Fig. 7).

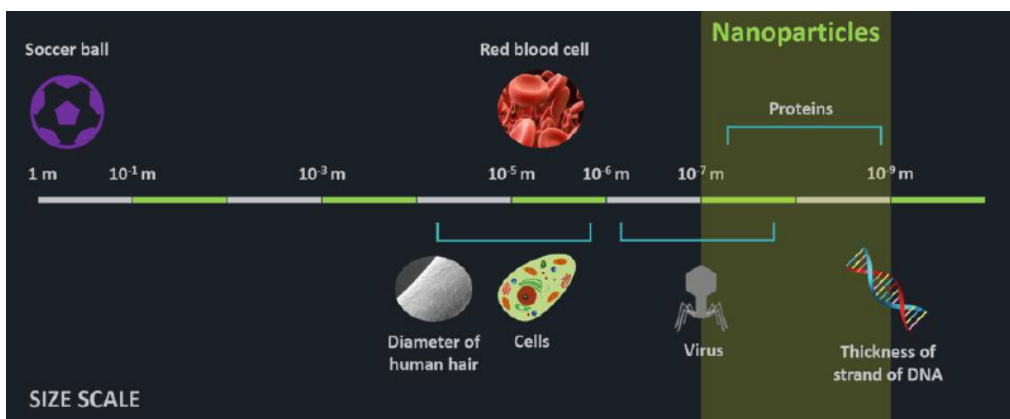
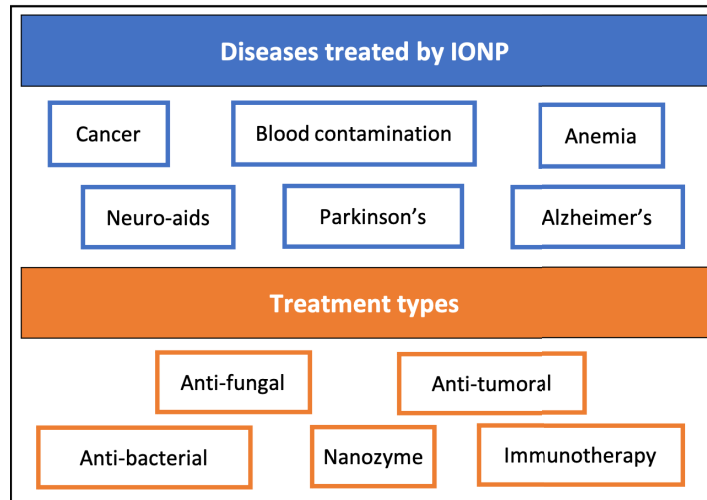


Figure 7: Size scale of nanoparticles compared to other biological structures.

MNPs can be used in diagnostic and therapeutic applications (Fig. 8). Their versatility allows also for a hybrid approach (*theranostics*), where they



**Figure 8:** Schematic representation of most of the pathologies treated with iron oxide nanoparticles. Inspired from [15].

are employed leveraging both the diagnostic and the therapeutic advantages.

MNPs are currently used as biosensors for *in vitro* diagnosis, as contrast agents in magnetic resonance imaging, as therapeutic carriers, as a therapeutic tool in magnetic fluid hyperthermia and to heal or replace tissues and organs. Typically, iron-oxide based MNPs are preferred for biomedical applications because of their magnetic properties and their biocompatibility; each nanoparticle has a core-shell structure, *i.e.* it is composed of a magnetic core and a coating—usually a biocompatible material allowing the MNP to be injected into the body, bypassing biological barriers—that avoids aggregation, guarantee colloidal stability and that can be functionalized with antibodies, fluorophores, peptides or other target-specific molecules.

In spite of these various fields of applicability and high biocompatibility, some open questions still hinder the exploitation of the potential offered by iron oxide nanoparticles: among them, which materials would be best, the standardization of synthesis procedures, and general safety issues. Many diagnostic formulations approved by the FDA (US Food and Drug Administration) and EMA (European Medicines Agency) over the years have been discontinued [16].

### 3.2 MAGNETIC FLUID HYPERTHERMIA

Thanks to the constant progress in nanotechnological research, in recent years *Magnetic Fluid Hyperthermia* (MFH) has garnered a lot of interest as



a thermo-therapeutic approach for cancer treatment, because of the advantages it offers also in conjunction with other therapies [17]. Today, cancer is the second cause of death worldwide, with increasing mortality rates. Hyperthermia (Hyp) is a promising alternative/ally to conventional therapies, such as surgery, radiation, gene therapy, chemotherapy and immunotherapy [18]. This medical modality uses heat (cells are exposed to high temperature, 40–44 °C) to selectively disrupt cells/intracellular structures, by exploiting the fact that cancer cells are more susceptible to heat stress due to their increased metabolic rates. The heat shock modifies the cellular processes thereby altering the protein structure and function of the cancer cells, eventually leading them to apoptosis/necrosis (cell deaths). Necrosis of the tumor mass is a process that is to be avoided when hyperthermia is applied, as the cell dies by disintegrating and spreading its cytoplasmic material in the intercellular space (unlike apoptosis, which occurs in an organized way), as the risk is that of triggering an inflammatory response in the body [19]. To avoid this, the temperature increase undergone by the tumor region must guarantee a temperature below 45 °C.

Recently papers have pointed out that hyperthermia both amplifies immune responses against cancer both decreases the immune suppression and immune escape of cancer. Moreover, it has also been shown that hyperthermia inhibits the repair mechanisms of cells after chemotherapy or radiotherapy [20].

Among hyperthermia-based therapies, MNPS-mediated hyperthermia offers some advantages, the most significant of which is deep penetration into tissues and selective killing of tumor cells without harming surrounding healthy tissues [21]. MFH dates back to 1957, when Gilchrist et al. [22] treated animal lymph nodes with MFH demonstrating that heat could kill the remaining metastases left behind after surgery.

Nowadays MFH is performed in clinic by MagForce, a German company specialized in nanocancer therapy for the treatment of tumors, which in 1997 initiated a decades-long study on the best materials and treatment methods, finally receiving the CE marking for its MFH system in 2010. To date, it can claim the treatment of more than a hundred patients with different types of cancer, *e.g.* prostate cancer and glioblastoma, spreading the MFH protocol to German, Polish and US hospitals. It is worth mentioning that in all successful cases (expectation of life enhance up to 1.5 times), MFH is not the only treatment administered; indeed, it is applied in combination with photon radiation therapy/chemotherapy. The MNPs injected into the tumor consist of iron-oxide based MNPs, with diameter  $d \simeq 12\text{--}15\text{ nm}$ , coated with aminosilane and dispersed in an aqueous solution [8, 23–28]. The MFH treatment procedure optimized by MagForce (Fig. 9) consists of a direct injection of MNPs into the tumor (usually 0.3 mL of ferrofluid—at concentration of about  $112\text{ mg mL}^{-1}$ —per  $\text{cm}^3$  of tar-

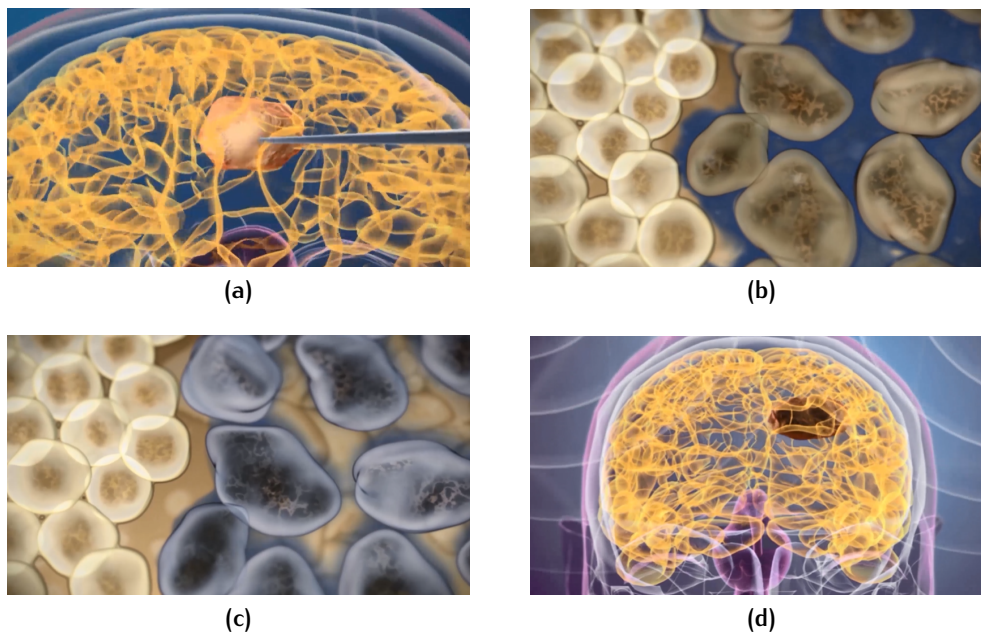


**Figure 9:** Schematic representation of the MFH treatment. (a) direct injection of MNPs into the tumor. (b) MNP diffusion in tumor cells and not in healthy tissues. (c) MNP uptake by tumor cells. (d) Exposure to an alternating magnetic field in order to reach the desired temperature [8].

get volume) and the application of an alternating magnetic field (AMF) at frequency  $f = 100$  kHz and amplitude  $H_{AMF} = 4\text{--}15$  kA/m. The treatment temperature is kept constant for 1 hour, and usually the treatment is repeated two times a week for three weeks, period in which MNPs remain into the tumor.

The safety limit (Brezovich criterion [29]), based on some clinical-tolerance tests on healthy volunteers whose thorax was exposed to an AMF by means of a single-turn induction coil [30] came in 1988 and is considered an upper limit that guarantees the patient's safety. This reads

$$H \cdot f < 4.85 \cdot 10^8 \text{ Am}^{-1} \text{ s}^{-1}. \quad (19)$$

Usually, in practice, different conditions (smaller coils, inhomogeneous field, different electrical conductivity of the tumor/different parts of the body etc) are used during the MFH treatment; this is the reason why this limit is currently under discussion and other criterions have been suggested [31–33].

### 3.3 PHYSICS OF HEATING WITH MNPS

When exposed to an AMF ( $H = H_{\max} \sin(2\pi ft)$ ), MNPs release heat; the amount of heat generated ( $A$ ) during one cycle of AC magnetic field is [30, 34]:

$$A = \mu_0 \oint M(H) dH, \quad (20)$$

where  $M(H)$  is the nano-object magnetization.  $P$ , the heating power of a MNP, is proportional to  $A$ , *i.e.* to the area of the hysteresis loop, and to  $f$ , the frequency of the field:

$$P = A \cdot f. \quad (21)$$

#### 3.3.1 Stoner-Wohlfarth theory

Under specific conditions (see below), the Stoner-Wohlfarth model gives a simple expression for the calculation of the MNP's *Specific Absorption Rate* (SAR). According to the Stoner-Wohlfarth theory (Section 2.5), in single-domain MNPs with an effective uniaxial anisotropy  $K_{\text{eff}}$  exposed to an external magnetic field, the magnetic energy, starting from Eq. (8) and normalized to  $k_B T$ , can be shown to be:

$$\frac{E(\vartheta, \varphi)}{k_B T} = \sigma \sin^2 \vartheta - \xi \cos(\vartheta - \varphi), \quad (22)$$

where

$$\begin{aligned} \sigma &:= \frac{K_{\text{eff}} V}{k_B T}, \\ \xi &:= \frac{\mu_0 M_s V H_{\max}}{k_B T}, \end{aligned}$$

and  $V$  is the MNP volume,  $\vartheta$  is the angle between the easy axis and the magnetization,  $\varphi$  is the angle between the easy axis and the magnetic field. If the direction of  $H$  is along the easy axis ( $\varphi = 0$ ), and the anisotropy field  $H_K = 2K_{\text{eff}}/\mu_0 M_s$  is less than the applied field maximum amplitude, the hysteresis loop is a square ( $H_c = H_K$ , with  $H_c$  the coercive field), whose area  $A_{\max}$  is:

$$A_{\max} = 4\mu_0 H_c M_s = 4\mu_0 H_K M_s = 8K_{\text{eff}}. \quad (23)$$

In this case the SAR turns out to be:

$$\text{SAR} = \frac{A \cdot f}{\rho}, \quad (24)$$

where  $f$  is the frequency of the alternating magnetic field and  $\rho$  is the MNPs concentration. The value of  $A$  decreases as the angle between the easy axis and the magnetic field increases; eventually  $A = 0$  when  $\vartheta$  is equal to  $\pi/2$ . For MNP-based systems with many random orientations, the hysteresis loop area turns out to be  $A < A_{\max}$ , as it is an average over all particle  $M(H)$  loops, and thus the SAR is smaller than in the previous case. In particular

$$A = 4\mu_0 H_c M_r = 2\mu_0 H_c M_s = 1.92 K_{\text{eff}}, \quad (25)$$

where  $M_r$  is the remanent magnetization  $M_r = 0.5 M_s$  and  $H_c = 0.48 H_K$ . The use of Stoner–Wohlfarth model to calculate the area  $A$  requires that  $H_c < H_{\max}$ , for  $\varphi = 0$  and  $2H_c < H_{\max}$  for random  $\varphi$ .

### 3.3.2 Linear Response Theory (LRT)

For SPM NPs, the heat dissipation is mainly due to the energy loss resulting from overcoming the energy barrier when an AMF is applied [17]. The Linear Response Theory (LRT) model is suitable to calculate the MNP hysteresis area and shape using the Néel–Brown relaxation time when the magnetic response is linear with the applied alternating magnetic field, namely [34]

$$M(t) = |\chi| H_{\max} \cos(\omega t + \varphi) = |\chi| H_{\max} \cos(2\pi f t + \varphi), \quad (26)$$

where  $|\chi|$  is the magnitude of the complex susceptibility and  $\varphi$  the phase between the AMF  $H(t) = H_{\max} \cos(\omega t)$  and the magnetization. The hysteresis loop area is

$$A = \pi H_{\max}^2 |\chi| \sin \varphi. \quad (27)$$

By rewriting the complex susceptibility as

$$\chi = \chi_0 \frac{1}{1 + i\omega\tau}, \quad (28)$$

with  $\chi_0$  the static susceptibility, and  $\tau$  the Néel–Brown relaxation time, it follows that

$$|\chi| = \frac{\chi_0}{\sqrt{1 + \omega^2\tau^2}}, \quad (29)$$

and, from its imaginary part is

$$\sin \varphi = \frac{\omega\tau}{\sqrt{1 + \omega^2\tau^2}}. \quad (30)$$

Consequently, the area of the elliptical hysteresis loop can be rewritten as:

$$A = \pi H_{\max}^2 \chi_0 \frac{\omega\tau}{1 + \omega^2\tau^2}. \quad (31)$$

The static susceptibility, introduced in Eq. (28) is:

$$\chi_0 = \frac{\mu_0 M_S^2 V}{\alpha k_B T}, \quad (32)$$

where

$\alpha$  is a  $M(H)$  shape and anisotropy dependent parameter,  
 $\alpha = 3$  for low anisotropy system –  $\sigma \ll 1$ ,  
 $\alpha = 1$  for high anisotropy system –  $\sigma \gg 1$ .

The SAR can be derived from Eq. (24). By including the expression of the imaginary part of the magnetic susceptibility

$$\chi''(\omega) = \chi_0 \frac{\omega \tau}{1 + (\omega \tau)^2} = \chi_0 \frac{2 \pi f \tau}{1 + (2 \pi f \tau)^2}, \quad (33)$$

it follows that

$$\text{SAR} = \mu_0 \pi f \chi''(f) \frac{H_{\max}^2}{\rho}. \quad (34)$$

The formula for the SAR in LRT is given by Eq. (34). The domain of validity of LRT is  $\xi < 1$  (*i.e.* thermal energy  $k_B T$  greater than the magnetic energy  $\mu_0 M_S H V$ ). When the superspin and the AMF experience the maximum dephasing (for  $\tau = 1/2\pi f$ ), the SAR reaches its maximum; this condition signals the transition from the superparamagnetic (SPM) regime to the ferromagnetic (FM) one. Looking at Eq. (33), it can be noticed that for  $f \tau \ll 1$ , the SAR  $\propto f^2$ , while at high frequencies, *i.e.* for  $f \tau \gg 1$ , SAR  $\rightarrow \mu_0 \chi_0 H^2 / 2 \tau \rho$ .

### 3.3.3 Rayleigh Model

Multi-domain MNP hysteresis losses, under the exposure to a magnetic field, are the results of the motion of the Weiss domains, and can be described through the so-called *Rayleigh losses*, which, for low magnetic-field values, are proportional to the cube of the amplitude of the field itself. A semi-empirical model was proposed by Hergt et al. [35] to describe hysteresis losses similar to the Rayleigh one in single domain ferromagnetic magnetic nanoparticles under the exciting field (amplitude  $H$  and frequency  $f$ ) when coherent reversal occurs; two cases can be distinguished:

$$\text{SAR}(H, D) = \begin{cases} \alpha \cdot D \cdot f \cdot H^3, & \text{if } H \leq H_C, \\ \frac{4 B_R \cdot H_C(D)}{\rho} \cdot f \cdot \left(1 - \frac{H_C(D)}{H}\right)^5, & \text{if } H > H_C, \end{cases}$$

where

- $\alpha$ : parameter that quantifies the Rayleigh losses supplement;
- $B_R = \mu_0 M_r$  with  $M_r$  the remanent magnetization;
- $H_C(D) = H_M \cdot \left(\frac{D}{D_1}\right)^{-0.6} \cdot \left(1 - \exp\left(-\frac{D}{D_1}\right)^5\right)$ ;
- $D$ : particle diameter;
- $D_1$ : diameter for transition of single-domain FM regime to the SPM regime.

For low field strengths, the dependence on  $H$  of hysteresis losses is of order three.

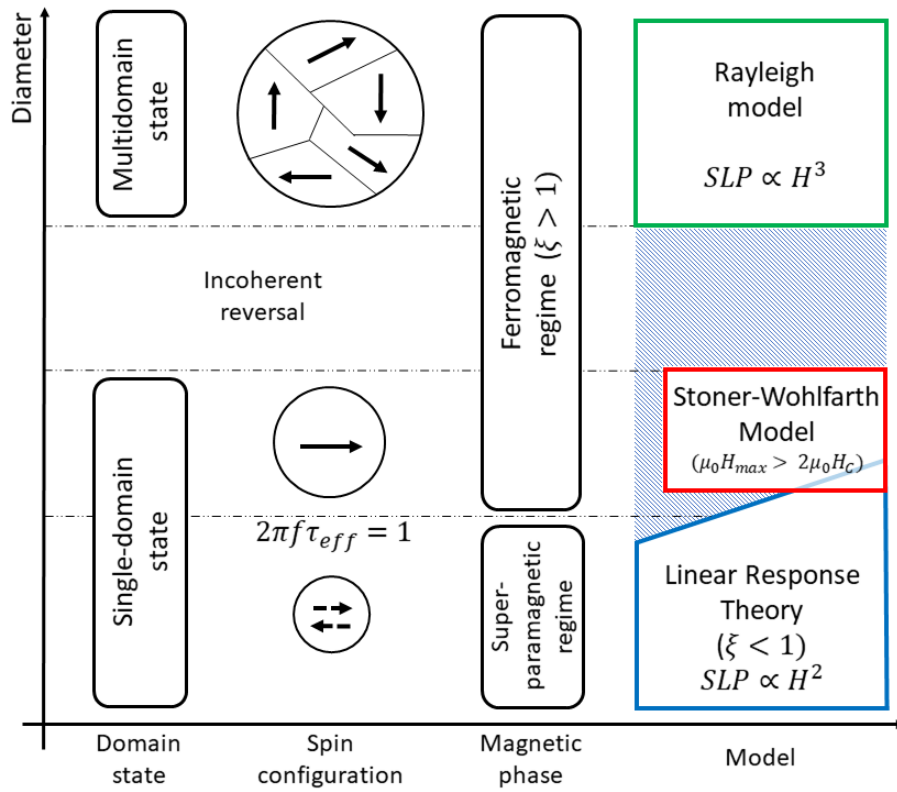


Figure 10: Schematic representation of the models for the SAR of MNPs. The validity ranges of the model are underlined, as a function of the particles diameter and the magneto-thermal quantity  $\xi = \mu_0 M_s V H_{\max} / k_B T$  [34, 36].

**SPECIFIC ABSORPTION RATE MODELS** Fig. 10 summarizes the models for the MNPs' Specific Absorption Rate presented in the previous paragraphs. Every model is valid in a different range, according to the size of the MNPs

and on  $\xi = \mu_0 M_s V H_{\max} / k_B T$ , where  $M_s$  is the saturation magnetization, and  $H_{\max}$  is the maximum applied field. If Linear Response Theory is valid,  $\xi \ll 1$ , a linear approximation of  $\xi$  is used for the Langevin function, which describes the relationship between  $M$  and  $H$ , and  $\text{SAR} \propto H^2$ . When  $\xi > 1$ , a non-linear modification of the Langevin function must be considered and the Rayleigh model,  $\text{SAR} \propto H^3$  is applied. The latter is useful to describe multi-domain MNP behavior and for ferromagnetic single-domain particles, in case of coherent reversal. For single-domain MNPs, the LRT model can be used only in the superparamagnetic regime, while in the FM or blocked regime the Stoner-Wohlfarth model (SWM) is used for SAR calculation, when  $\mu_0 H_{\max} > 2\mu_0 H_c$  is satisfied,  $H_c$  being the coercive field of the MNPs. However, due to the dependence of the coercive field  $H_c$  on the volume of the MNPs, there exists a volume range, formally in the FM regime, where the LRT model still holds. Therefore, in this region, there is not a single model for the SAR, and thus also the exponent that describes the SAR( $H$ ) behaviour is not univocally defined.

### 3.4 EXPERIMENTAL SAR EVALUATION

The specific absorption rate is a key parameter in quantifying the MNP's heating efficiency when an alternating magnetic field is applied. In the actual experimental measure, the sample placed in a vial, is positioned inside a coil of variable sizes according to the equipment being employed. The curve one typically acquires is temperature, generally measured by optical fiber probes, versus the application time of the AMF. SAR is defined as the heating power generated per unit mass:

$$\text{SAR} = \frac{P}{m_{\text{MNP}}}, \quad (35)$$

and several methods are available in literature to extract SAR value from the temperature vs AFM interval application curve.

The *Initial slope method*, which is the most used one, assumes that the initial slope of the curve is not affected by the heat losses (adiabatic condition). In this case, one can write

$$C \cdot \left. \frac{dT}{dt} \right|_{t=0} = P, \quad (36)$$

where  $C$  is the heat capacity of the sample; therefore,

$$\text{SAR}_{\text{MNP}} = \frac{m_{\text{MNP}} c_{\text{MNP}} + m_{\text{sol}} c_{\text{sol}}}{m_{\text{MNP}}} \cdot \left. \frac{dT}{dt} \right|_{t=0} \quad (37)$$

where, according to Cervadoro et al. [37], the SAR of the MNPs alone is obtained by introducing  $c_{\text{sol}}$  as the specific heat of solvent (mostly water),  $c_{\text{MNP}}$  as the specific heat of the MNPs in the colloidal solution and  $m_{\text{sol}}$ ,  $m_{\text{MNP}}$  as the respective masses.

In non-adiabatic conditions, as soon as the sample temperature exceeds that of the environment, the sample loses its thermal energy (by conduction, convection, or radiative phenomena); thus, the heating curve transforms to the one represented in Fig. 11.

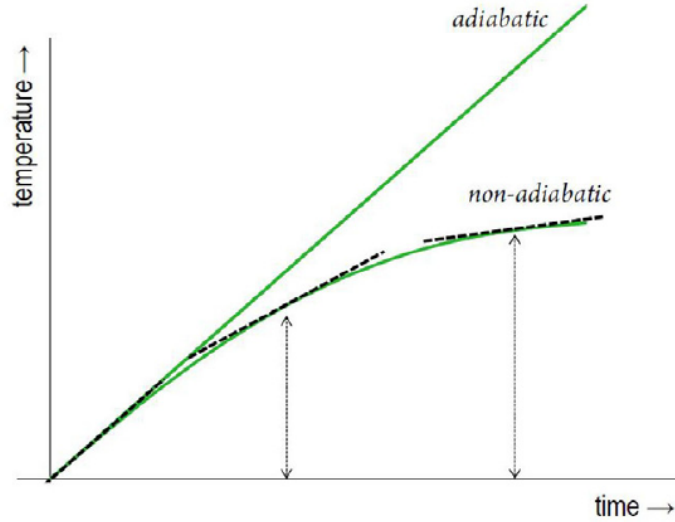


Figure 11: Typical heating curves obtained in calorimetric measurements with an adiabatic and a non-adiabatic setup [38].

The temperature behaviour can be expressed as [38]:

$$C \cdot \frac{dT(t)}{dt} = P - P'(T), \quad (38)$$

where  $P'(T)$  is a function describing the power loss as a function of the temperature; the latter can be a linear function, *i.e.*  $P'(T) = k\Delta T$  or a non-linear one. In the former case, the heating curve can be fitted with the Box–Lucas equation

$$\Delta T = A \cdot (1 - \exp(-\eta(t + t_0))), \quad (39)$$

therefore

$$\text{SAR}_{\text{MNP}} = \frac{m_{\text{MNP}} c_{\text{MNP}} + m_{\text{sol}} c_{\text{sol}}}{m_{\text{MNP}}} \cdot A \cdot \eta \quad (40)$$

where  $t_0$  is needed when the curve starts at non-zero time.

The *corrected slope method*, presented by Wildeboer et al. [38], is designed to



analyze and compensate for the heat losses. More specifically, the SAR is computed by

$$\text{SAR} = \frac{1}{N} \sum_i^N \frac{C(\frac{dT}{dt})_i + k(\Delta T)_i}{m} \quad (41)$$

by dividing—after the cooling analysis to identify the linear-loss region—the heating curve into  $N$  intervals (each about 30–60 s long), in which the  $(dT/dt)_i$  is determined by a linear fit in the  $i$ -th interval and  $\Delta T_i$  is the difference between the mean temperature of the interval  $i$  and the equilibrium temperature of a sample, found by applying an AMF of the chosen amplitude and frequency to a sample of the MNP solvent alone (*e.g.* water), without any MNPs present.

Several factors can influence the determination of the SAR: among these, for example, non-uniformities in the magnetic field, the non-adiabaticity of the measuring system [39], coil geometries, sample preparation (aggregation phenomena have to be avoided),  $dT/dt$  calculation method [40].

Within this framework, the RADIOMAG EU COST action TD 1402.19 [41], of which the author was a participant, recently conducted an interlaboratory study of calorimetry measurements across about twenty European sites. In brief, the results, gathered in a paper that was submitted a few months ago and currently under revision, reveal a current lack of harmonization in MFH characterization of MNPs, and highlights the growing need for standardized, quantitative characterization techniques for this emerging medical technology.

#### 3.4.1 Intrinsic loss parameter

The Intrinsic Loss Parameter (ILP) was introduced for normalization of specific absorption rate (SAR, W/g) values measured at different magnetic field amplitudes ( $H$ , kA/m) and frequencies ( $f$ , kHz), in order to better compare MNP systems, characterized under different experimental conditions. The ILP is indeed defined as

$$\text{ILP} = \frac{\text{SAR}}{fH_{\max}^2}, \quad (42)$$

where  $H_{\max}$  is the maximum amplitude of the AMF. It should be noted that the ILP definition is restricted to the LRT range; the dependence of the SAR on the square of the amplitude of the applied magnetic field is in fact guaranteed only in the linear region. Furthermore, as underlined in the SAR definition of Eq. (34), the imaginary part of the magnetic susceptibility  $\chi''$  is not independent of the frequency, thus the ILP parameter can only be considered constant in relatively low field strength and low frequency regimes [42]. In particular, Rosensweig [43] predicted a field-independent

$\chi''$  at low frequencies such as those currently used in most clinical magnetic hyperthermia systems (100 kHz–1 MHz), and for the case of polydisperse MNPs in a solution (with a crystallite polydispersity index  $\text{PDI} > 0.1$ ).

# 4

---

## NUCLEAR MAGNETIC RESONANCE

---

**I**N this chapter, the physical principles of Nuclear Magnetic Resonance (NMR) will be presented, pointing out the mechanisms of proton relaxation induced by superparamagnetic nanoparticles and presenting the Roch, Muller and Gillis model which explain the shape of the nuclear magnetic resonance dispersion profiles.

### 4.1 INTRODUCTION

In Nuclear Magnetic Resonance experiments, nuclear spins are used as local probes to study the microscopic dynamics experienced by the nuclei and the environment surrounding them.

Certain atomic nuclei possess a nuclear spin and thus a permanent magnetic dipole moment ( $\mu = \gamma\hbar I$ ), where  $I$  can assume integer or semi-integer values  $m = -I, -I + 1, \dots, I$  ( $2I + 1$  values) along the quantization axis.

The Zeeman Hamiltonian in the presence of an external magnetic field is given by

$$\mathcal{H}_Z = -\gamma\hbar\vec{H} \cdot \vec{I} \quad (43)$$

where  $\hbar = \frac{h}{2\pi}$  is Planck's constant divided by  $2\pi$  and  $\gamma$  is the nuclear gyromagnetic ratio; assuming the field is oriented along the  $z$ -axis ( $\vec{H} = H_0\hat{z}$ ),  $E = -\gamma\hbar H_0 m$  are the eigenvalues of Eq. (43).

Consider for simplicity the hydrogen nucleus ( $I = \frac{1}{2}$ ,  $m = \pm\frac{1}{2}$ ). In the absence of a magnetic field, the energy levels of hydrogen are degenerate, *i.e.* they correspond to the same energy value and therefore the spins can indiscriminately choose how to orient themselves. On the contrary, in a static main magnetic field  $H_0$ , the magnetic dipole moments are pointed either in the direction of the main field or in the opposite direction (lower and higher energy state respectively) [44].

$^1\text{H}$	42.58	$\frac{1}{2}$	$^{19}\text{F}$	40.05	$\frac{1}{2}$	$^{63}\text{Cu}$	11.28	$\frac{3}{2}$	$^{121}\text{Sb}$	10.19	$\frac{5}{2}$
$^2\text{H}$	6.535	1	$^{23}\text{Na}$	11.42	$\frac{3}{2}$	$^{65}\text{Cu}$	12.09	$\frac{3}{2}$	$^{127}\text{I}$	8.518	$\frac{5}{2}$
$^7\text{Li}$	16.55	$\frac{3}{2}$	$^{27}\text{Al}$	11.09	$\frac{5}{2}$	$^{75}\text{As}$	7.291	$\frac{3}{2}$	$^{133}\text{Cs}$	5.584	$\frac{7}{2}$
$^9\text{Be}$	5.984	$\frac{3}{2}$	$^{29}\text{Si}$	8.458	$\frac{1}{2}$	$^{77}\text{Se}$	8.118	$\frac{1}{2}$	$^{195}\text{Pt}$	9.153	$\frac{1}{2}$
$^{10}\text{B}$	4.575	3	$^{31}\text{P}$	17.24	$\frac{1}{2}$	$^{79}\text{Br}$	10.67	$\frac{3}{2}$	$^{199}\text{Hg}$	7.590	$\frac{1}{2}$
$^{11}\text{B}$	13.66	$\frac{3}{2}$	$^{35}\text{Cl}$	4.172	$\frac{3}{2}$	$^{81}\text{Br}$	11.50	$\frac{3}{2}$	$^{201}\text{Hg}$	2.809	$\frac{3}{2}$
$^{13}\text{C}$	10.71	$\frac{1}{2}$	$^{37}\text{Cl}$	3.473	$\frac{3}{2}$	$^{87}\text{Rb}$	13.93	$\frac{3}{2}$	$^{203}\text{Tl}$	24.33	$\frac{1}{2}$
$^{14}\text{N}$	3.076	1	$^{51}\text{V}$	11.19	$\frac{7}{2}$	$^{93}\text{Nb}$	10.41	$\frac{9}{2}$	$^{205}\text{Tl}$	24.57	$\frac{1}{2}$
$^{15}\text{N}$	4.314	$\frac{1}{2}$	$^{55}\text{Mn}$	10.50	$\frac{5}{2}$	$^{117}\text{Sn}$	15.17	$\frac{1}{2}$	$^{207}\text{Pb}$	8.907	$\frac{1}{2}$
$^{17}\text{O}$	5.772	$\frac{5}{2}$	$^{59}\text{Co}$	10.05	$\frac{7}{2}$	$^{119}\text{Sn}$	15.87	$\frac{1}{2}$	$^{209}\text{Bi}$	6.841	$\frac{9}{2}$

**Table 2:** Gyromagnetic ratio  $\frac{\gamma}{2\pi}$  (MHz/T) and nuclear spin of a few nuclei. To get the Larmor frequency  $\nu_L$  from  $\frac{\gamma}{2\pi}$ , we have to multiply with the corresponding value of magnetic induction.

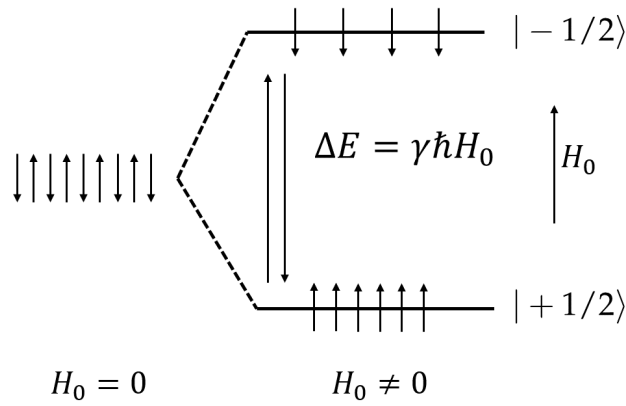


**Figure 12:** Schematic representation of the Zeeman effect in case of hydrogen atom: split of the energy levels when a magnetic field is applied.

The energy of the two levels is

$$E_+ = \frac{-\gamma\hbar H_0}{2} = \frac{-\hbar\gamma_0}{2} \quad \text{and} \quad E_- = \frac{\gamma\hbar H_0}{2} = \frac{\hbar\gamma_0}{2}. \quad (44)$$

The two states are populated according to a Boltzmann distribution by the nuclear spins with a higher population in the lower state at body temperature:

$$\frac{N_+}{N_-} = \exp\left(\frac{\Delta E}{k_B T}\right) = \exp\left(\frac{\gamma_I \hbar H_0}{k_B T}\right) \quad (45)$$

where  $\Delta E$  is the energy level gap between the two levels and  $k_B \approx 1.38 \cdot 10^{-23}$  J/K is the Boltzmann constant. In Eq. (45),  $\Delta E = \gamma \hbar H_0 = \hbar \omega_0 = \hbar \nu_L$ , where the resonant Larmor frequency  $\nu_L$  is named after Joseph Larmor, the Irish physicist who described in 1897 the precession of the magnetic moment of an object about an external magnetic field.

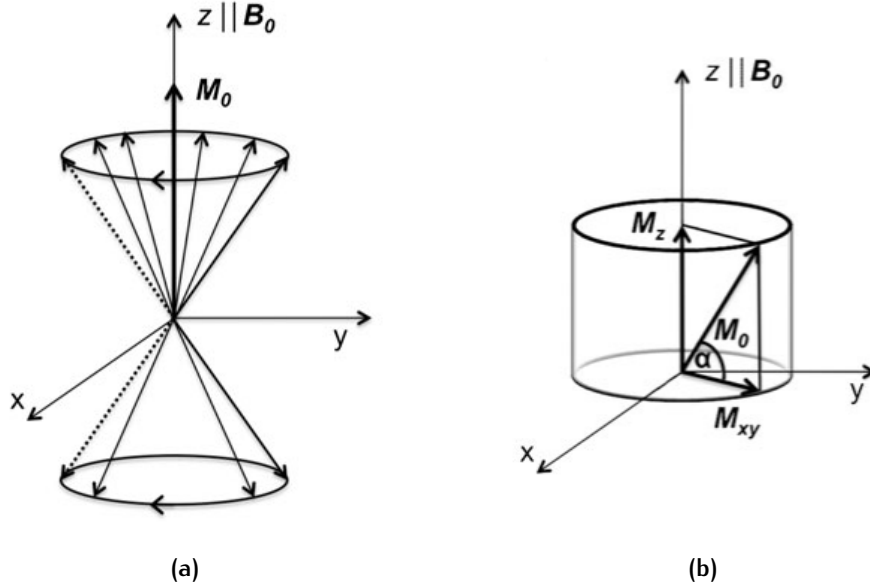


**Figure 13:** (a) The Boltzmann distribution of an ensemble of hydrogen nuclei. In thermal equilibrium the net magnetization  $M_0$  is due to the difference in the number of nuclear spins populating energy levels. (b) The net magnetization  $M_0$  precesses in the stationary frame around the z axis and it can be split into two components: the transversal magnetization  $M_{x,y}$  and the longitudinal magnetization  $M_z$  [45].

It is possible to describe the Larmor precession using a classical model approach. An external magnetic field  $\vec{H}_0 = H_0 \hat{z}$  results in a torque  $\tau = \vec{\mu} \times \vec{H}_0$ . The latter is defined as the time derivative of the angular momentum, so the magnetic moment, under the action of  $H_0$  precesses around  $\hat{z}$ , following

$$\frac{d\vec{\mu}}{dt} = \vec{\mu} \times \gamma \vec{H}_0. \quad (46)$$

The NMR technique does not observe the single nucleus but statistically measures the effect of an external or internal perturbation on the population of an Avogadro number of nuclei of the sample material under examination. We therefore define a magnetization vector  $\vec{M}$ , or local magnetic

moment per unit volume, given by the vector sum of the magnetic moments  $\mu$  of the individual nuclei contained in a sample volume  $V$ :

$$\vec{M} = \frac{1}{V} \sum_{i=1} \vec{\mu}_i, \quad (47)$$

whose motion is governed by:

$$\frac{d\vec{M}}{dt} = \vec{M} \times \gamma \vec{H}_0. \quad (48)$$

Considering a reference frame rotating at a pulse frequency  $\omega$  around  $\hat{z}'$  coincident with  $\hat{z}$  (*i.e.*  $\hat{z}' \equiv \hat{z}$ ). The Eq. (46) becomes:

$$\frac{d\vec{M}}{dt} = \vec{M} \times \gamma \left[ \vec{H}_0 + \frac{\vec{\omega}}{\gamma} \right], \quad (49)$$

where  $\vec{H}_0 + \frac{\vec{\omega}}{\gamma}$  is the effective field  $\vec{H}_{\text{eff}}$  in the rotating frame. This result shows that, in general, in the rotating reference system there is a precession around the axis defined by  $\vec{H}_{\text{eff}}$ . Considering from now a rotating frame  $S'$  at the Larmor frequency ( $\omega = \omega_0$ ), the second term of the vector product in Eq. (49) vanishes and therefore  $\frac{d\vec{M}}{dt} = 0$ . Nuclear magnetization  $\vec{M}$  is therefore stationary in  $S'$ : neglecting the precession, it is possible to study other effects on magnetization.

## 4.2 NMR EXPERIMENTS - BLOCH EQUATIONS

In NMR experiments, a radiofrequency (*rf*) magnetic field  $\vec{H}_1$  is applied to rotate the magnetization  $\vec{M}$  away from the  $\hat{z}$  axis. The resonance condition must be verified, *i.e.*  $\vec{H}_1$  must oscillate at the same precession frequency as  $\vec{M}$ , the Larmor frequency  $\omega_0$ , and must have components in the  $\hat{x}$  and/or  $\hat{y}$  direction in accordance with Eq. (49). Experimentally, a coil is positioned for example along the  $x$  axis and an alternating current at frequency  $\omega_0$  flows through it, thus generating an oscillating magnetic field linearly polarized along the  $\hat{x}$  axis.

$M_0$  is flipped by an angle  $\alpha = \gamma H_1 \tau$  by applying for a certain time interval  $\tau$  a perturbing magnetic field ( $H_1$ ) perpendicular to the static magnetic field  $H_0$ . In the laboratory frame  $\vec{H}_1 = H_1 \cos(\omega_0 t) \hat{x} + H_1 \sin(\omega_0 t) \hat{y}$ . This field rotates in the  $(x, y)$  plane in the lab frame, and it is stationary in the rotating frame. A Free Induction Decay (**FID**) signal, arising from the rotating magnetization (the voltage is induced via Faraday's law), can be

detected immediately after the application of this pulse, using a receiving coil positioned in the  $(x, y)$  plane.

After the application of the rf pulse ( $H_1 = 0$ ), the temporal evolution of the magnetization is described by the *Bloch equations*:

$$\begin{cases} \frac{d\vec{M}_z}{dt} = \gamma_I(\vec{M} \times \vec{H}_0)_z + \frac{M_0 - M_z}{T_1}, \\ \frac{d\vec{M}_{x,y}}{dt} = \gamma_I(\vec{M} \times \vec{H}_0)_{x,y} - \frac{M_{x,y}}{T_2}. \end{cases}$$

These equations are easier to solve in a frame which rotates around the z-axis with  $\omega_{\text{rot}} = \omega_0$ .

We observe (see Fig. 14):

- The recovery of  $M_z$ : due to spin-lattice interaction the system returns to thermal equilibrium (equilibrium condition  $T_S = T_R$ , being  $T_S$  the temperature of the nuclear spin system and  $T_R$  the temperature of the lattice). - *Longitudinal Relaxation*

$$\text{ROTATING FRAME:} \quad M_z(t) = M_{z,0}e^{-\frac{t}{T_1}} + M_0 \left(1 - e^{-\frac{t}{T_1}}\right), \quad (50a)$$

$$\text{LABORATORY FRAME:} \quad M_z(t) = M_{z,0}e^{-\frac{t}{T_1}} + M_0 \left(1 - e^{-\frac{t}{T_1}}\right); \quad (50b)$$

- A decay of the magnetization in the plane  $(x, y)$  (Fig. 14b) - *Transverse Relaxation*

$$\text{ROTATING FRAME:} \quad M_{x,y}(t) = M_{x,y,0}e^{-\frac{t}{T_2}}, \quad (51a)$$

$$\text{LABORATORY FRAME:} \quad M_{x,y}(t) = M_{x,y,0}e^{-\frac{t}{T_2}}e^{-i\omega_0 t}. \quad (51b)$$

As to the longitudinal magnetization, the recovery of  $M_z$  to equilibrium is exponential in form, and the characteristic time for spins to align with the magnetic field is called  $T_1$  (*spin-lattice relaxation time* or longitudinal relaxation time).

$T_2$  is the *spin-spin relaxation time*, the time constant characterizing the  $M_{x,y}$  vanishing.  $T_2$  decay is observed due to the interactions of an ensemble of spins dephasing from each other. In particular, each nucleus constituting the system is affected by a local magnetic field that is the sum of the external static one and an internal field generated by the neighboring nuclei. In general, the value of this field varies over time and space due to the rapid fluctuations to which nuclear spins are subjected; it follows that the magnetic moments in the different points of space do not all resonate at the same frequency, but cover a certain distribution centered in  $\omega_0$ . The time  $T_2$  can be thought of as the time it takes  $M_{x,y}$  to drop to  $1/e \approx 37\%$  of its initial value.

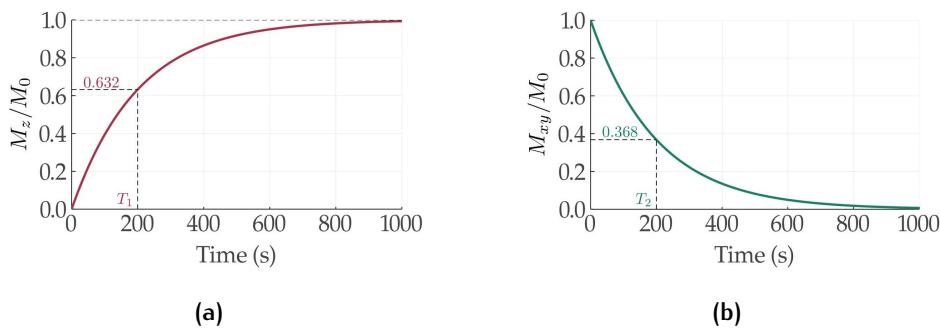


**Figure 14:** Bloch equations: (a) Recovery of the longitudinal nuclear magnetization  $M_z(t)$  with a characteristic relaxation time  $T_1$ . (b) Decay of the transversal magnetization  $M_{x,y}(t)$  with a characteristic relaxation time  $T_2$ .

In solids, the nuclei are not free to displace. Hence, no matter how uniform the applied field is, the local magnetic fields due to neighboring nuclei in the material can cause  $T_2$  to be very short. In contrast, the nuclei in liquids move so fast that they average out the varying local fields so quickly that the only cause for transverse relaxation is the returning of the magnetization to the  $z$ -axis. Thus frequently  $T_2$  equals  $T_1$  in liquids. However,  $T_2$  can never be longer than  $T_1$ .

### 4.3 NMR SIGNAL

The relaxation processes of the nuclear magnetization determine a variation of the magnetic flux in the coil used to apply the  $rf$  pulse and induce an electromotive force on it (for the *Faraday–Neumann–Lenz* law)<sup>1</sup>, of a few  $\mu\text{V}$ , which represents the signal  $S(t)$  of the NMR experiment to be acquired:

$$S(t) = -\frac{d\Phi_M(t)}{dt} = -\frac{d}{dt} \int_{\text{sample}} d^3r \vec{B}^{\text{receive}}(\vec{r}) \cdot \vec{M}(\vec{r}, t), \quad (52)$$

where  $\vec{B}^{\text{receive}}$  is the magnetic field per unit of induced current, generated by the motion of  $\vec{M}$ .

In the simplest NMR experiment, in which a  $\pi/2$  pulse is applied that flips the longitudinal magnetization on the transverse plane and the  $\Delta V$  produced by the variation of the magnetic flux is acquired through the coil, the response signal of the system is called Free Induction Decay.

<sup>1</sup> Faraday's law states that a time-varying magnetic flux through a loop of wire, or any circuit, generates a voltage whose amplitude is proportional to the (negative) rate of change of the flux. The time-varying magnetic fields associated with the precessing magnetization in NMR induce voltages in the  $rf$  receive coil, giving rise to the NMR signal.



The Fourier transform of the received signal  $S$ , produced by the system of nuclei that relax after turning off the excitation pulse, provides the *nuclear absorption spectrum*

$$f(\omega - \omega_0) = \int S(t) e^{i2\pi(\omega - \omega_0)t} dt, \quad (53)$$

which is made up of the set of resonance lines (or, equivalently, absorption) of the investigated nuclei. In fact, even just for the inhomogeneity of the field, nuclei of the same type absorb energy at different frequencies and therefore the frequency spectrum, centered in  $\omega_0$ , is broadened. Therefore, for the success of an NMR experiment, it is important to irradiate all the frequencies of interest simultaneously and uniformly. For this purpose, the excitation pulse transmitted to the system, usually a sampling function  $\text{sinc}(t) = \sin(t)/t$ , must have a duration  $\Delta t$  such that its Fourier transform, corresponding to a rectangular function (or boxcar) of width  $\Delta\omega$ , contains the entire frequency range over which the nuclei under examination precess. According to the theory of the Fourier transform, the shorter the impulse, the wider the boxcar will be and vice versa.

#### 4.4 NUCLEAR RELAXATION THEORY IN PRESENCE OF SUPERPARAMAGNETIC NANOPARTICLES

Increasing spin-lattice relaxation rates ( $1/T_1$ ) or spin-spin relaxation rates ( $1/T_2$ ) is the purpose of magnetic resonance imaging contrast agents (CAs), leading to a loss of signal or hypointensity on MR images (negative CAs) or an increment of the signal (positive CAs). Both cause an increase in the final image contrast. Let us look the signal collected in a typical MRI experiment performed with a classical spin-echo sequence:

$$S(t) \propto \rho(^1\text{H}) e^{-\frac{TE}{T_2}} \left(1 - e^{-\frac{TR}{T_1}}\right) e^{-bD} \quad (54)$$

where  $\rho(^1\text{H})$  is the proton density,  $D$  the diffusion coefficient,  $b$  a constant,  $TE$  the echo time and  $TR$  the repetition time. The increase in contrast is dependent upon both the MRI acquisition parameters ( $TE, TR$ ) and the properties of the nanoparticles, such as their size and magnetic moment.

Superparamagnetic Iron Oxide Nanoparticles (**SPIONs**) lead to magnetic field inhomogeneities when introduced into the system; nearby proton magnetic moments precess at different rates, leading to a reduction in phase coherence. This dephasing of the proton magnetic moments can be characterized by a reduction in transverse relaxation time.

The relaxivity is defined as the increment of the relaxation rate of the protons of the solvent induced by one millimole per litre of the magnetic ion.

$$r_i = \frac{1}{C} \left( \frac{1}{T_{i,obs}} - \frac{1}{T_{i,diam}} \right) \quad (55)$$

where  $i = 1, 2$ , the relaxation rate of the aqueous system is  $1/T_{i,obs}$ , and  $1/T_{i,diam}$  is the relaxation rate of the system without the CA,  $C$  is the molar concentration of the magnetic ions, expressed in mM (mmol/L).

#### 4.4.0.1 Inner Sphere and Outer Sphere Mechanisms

The superparamagnetic relaxation mechanism springs from the original theory developed for paramagnetic systems (such as Gd(III) complexes). Two mechanisms contribute to the proton relaxation: *inner-sphere* and *outer-sphere* relaxations.

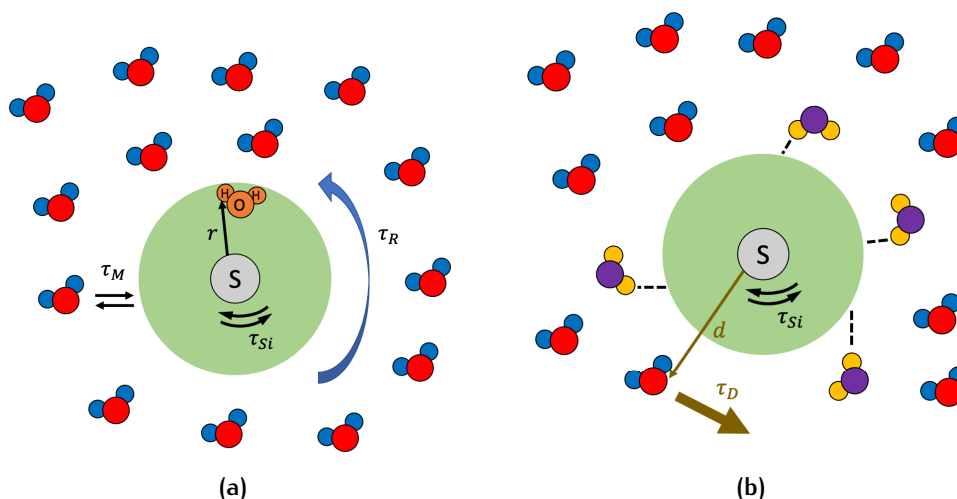


Figure 15:  $^1\text{H}$  relaxation induced by paramagnetic system: (a) Inner Sphere Mechanism. (b) Outer-Sphere mechanism.  $\tau_M$ : exchange time,  $\tau_R$ : rotational correlation time,  $\tau_S$ : electronic spin correlation time,  $\tau_D$ : diffusion time.

The inner-sphere mechanism considers the permanence of the water molecule for a certain time in close vicinity of the magnetic ion, through an exchange time  $\tau_M$ , and takes into account also the rotational correlation time  $\tau_R$  and the nuclear and electronic spin correlation time  $\tau_S$ . The dipolar and scalar coupling of the spins cause the relaxation process also through the direct energy exchange between protons and electrons located in the first hydration sphere of the paramagnetic center (*i.e.* atoms or ions with unpaired electrons).

To characterize the dipolar and contact coupling between the water molecules in the first coordination sphere and the paramagnetic compound, two correlation times  $\tau_{C_1}$  and  $\tau_{C_2}$  are defined, according to the law:

$$\frac{1}{\tau_{C_i}} = \frac{1}{\tau_R} + \frac{1}{\tau_M} + \frac{1}{\tau_{S_i}}, \quad (56)$$

where  $i = 1, 2$ .

The outer-sphere contribution considers the diffusion of the water molecule at a certain distance from the nanoparticle, in the local magnetic field gradient generated by the ion. The interaction between proton spins and the magnetic moment is a dipolar interaction. This mechanism, modeled by Freed, lasts, on average,  $\tau_D$ , named *translational correlation time* that takes into account the relative diffusion of the paramagnetic center and the solvent molecule, and the distance of closest approach.

The diffusion time is given by

$$\tau_D = \frac{r_d^2}{D}, \quad (57)$$

where  $D$  is the relative diffusion coefficient (that depends on the solvent) and  $r_d$  is the minimum approach distance between the water molecules and the paramagnetic center (a spherical symmetry is assumed).

## 4.5 THEORY OF PROTON RELAXATION INDUCED BY SUPERPARAMAGNETIC NANOPARTICLES

A. Roch, R.N. Muller and P. Gillis in the '90s theorized the relaxation mechanism induced by Iron Oxide Nanoparticles. Their model allows to reproduce NMR dispersion curves (NMRD profiles), *i.e.*  $^1\text{H}$  water relaxation rates,  $1/T_1$  and  $1/T_2$ , over an extended range of magnetic fields (from some kHz to hundredths of MHz). If we analyze the NMRD profiles of nanoparticles with a radius less than  $\sim 14\text{nm}$ , one can observe that at low fields a dispersion appears, not present in NMRD profiles of nanoparticles with a larger radius. This dispersion is due to the low energy of anisotropy that characterizes the SPIONs, which is why the magnetization precesses in a direction far from the axis of anisotropy. By introducing the anisotropy energy as a quantitative parameter of the problem, the RMG model, presented for a crystal characterized by a uniaxial symmetry, is able to reproduce the entire dispersion profile.

As a starting point, let us analyze the case of high magnetic anisotropy.

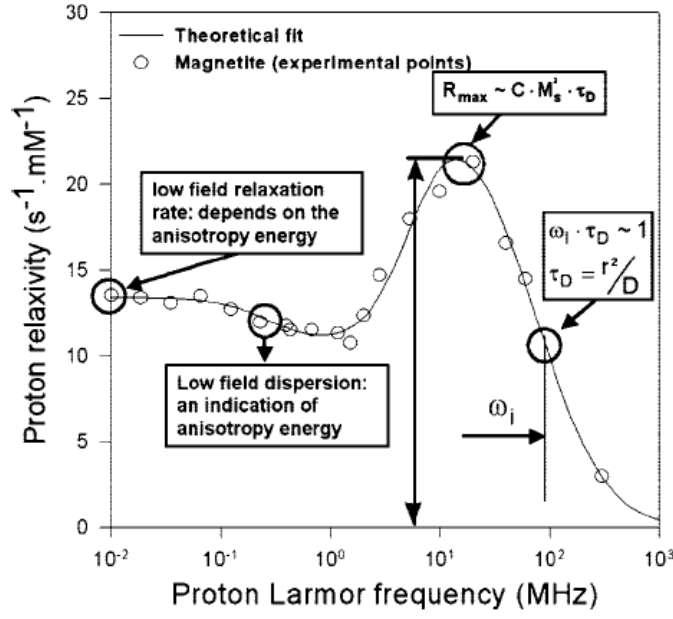


Figure 16: Superparamagnetic MNPs in water: longitudinal NMR dispersion profile. Both experimental data on magnetite MNPs and the theoretical fit (RMG model) are reported [46].

#### 4.5.0.1 High Magnetic Anisotropy SPIONs

At low fields, the magnetic field experienced by protons diffusing in proximity of the superparamagnetic nanoparticles fluctuates because of the super-spin flip along the two easy directions (Néel Relaxation -  $\tau_N$ ). The Néel relaxation and the diffusion of water molecules rule the dipolar interactions between protons and NPs. The total correlation time ( $\tau_C$ ) is given by:

$$\frac{1}{\tau_C} = \frac{1}{\tau_D} + \frac{1}{\tau_N}. \quad (58)$$

Introducing the *Freed spectral density function*  $J^F$ , that accounts for both the Curie and Néel relaxation ( $\nu_L \leq 1 - 10$  MHz), the relaxation rates are:

$$\frac{1}{T_1} = \frac{32\pi}{405} \mu_{SP}^{*2} \gamma_I^2 \left( \frac{N_M}{r_d D} \right) \left[ \frac{10}{3} J^F(\omega_0) \right] \quad (59)$$

and

$$\frac{1}{T_2} = \frac{32\pi}{405} \mu_{SP}^{*2} \gamma_I^2 \left( \frac{N_M}{r_d D} \right) \left[ \frac{4}{3} J^F(\omega_0) + 2J^F(0) \right] \quad (60)$$

where

$$J_F(\omega_L, \tau_D, \tau_N) = \text{Re} \left( \frac{1 + \frac{1}{4}\Omega^{1/2}}{1 + \Omega^{1/2} + \frac{4}{9}\Omega + \frac{1}{9}\Omega^{3/2}} \right), \quad (61)$$

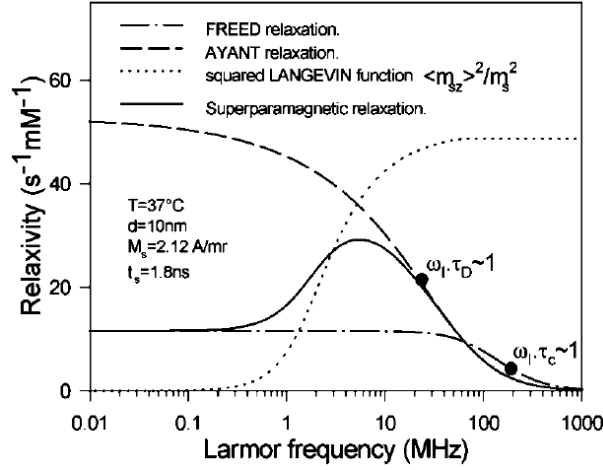


Figure 17: Longitudinal NMRD profile for the  $^1\text{H}$  relaxation in the case of a SPM nanoparticle (high anisotropy energy limit), according to Roch's theory. At high fields the only mechanisms responsible of the relaxation are those of the Curie relaxation (Ayant spectral density function); at low fields, the Néel relaxation also contributes (Freed spectral density function) [46].

with

$$\Omega = i\omega_l\tau_D + \frac{\tau_D}{\tau_N}. \quad (62)$$

In Eq. (59) and Eq. (60)  $N_M$  is the number of particles per unit volume,  $r_d$  the radius of nanoparticles,  $D$  the diffusion coefficient,  $\gamma_I$  the gyromagnetic ratio of the proton,  $\mu_{SP}$  the magnetic moment of the electrons and  $\omega_0$  the proton Larmor frequency.

At high magnetic fields ( $\nu_L > 1-10$  MHz) the Néel relaxation is suppressed, the superspin is blocked and the dipole-dipole interaction between protons and nanoparticles is governed by the diffusing processes. The relaxation rates are

$$\frac{1}{T_1} = \frac{32\pi}{405} \mu_{SP}^* \gamma_I^2 \left( \frac{N_M}{r_d D} \right) \left[ 9J^A(\sqrt{2\omega_0\tau_D}) \right], \quad (63)$$

$$\frac{1}{T_2} = \frac{32\pi}{405} \mu_{SP}^* \gamma_I^2 \left( \frac{N_M}{r_d D} \right) \left[ 4.5J^A(\sqrt{2\omega_0\tau_D}) + 6J^A(0) \right] \quad (64)$$

with

$$J_A(z) = \frac{1 + \frac{5z}{8} + \frac{z^2}{8}}{1 + z + \frac{z^2}{2} + \frac{z^3}{6} + \frac{4z^4}{81} + \frac{z^5}{81} + \frac{z^6}{648}}. \quad (65)$$

A linear combination of the high and low frequencies contribution allows one to express relaxation rates in the intermediate field case:

$$\frac{1}{T_1} = \frac{32\pi}{405} \mu_{SP}^* \gamma_I^2 \left( \frac{N_M}{r_d D} \right) \left[ \left( 1 - \frac{2L(x)}{x} - L^2(x) \right) 10J^F(\omega_0) + L^2(x) 9J^A(\sqrt{2\omega_0 \tau_D}) \right]. \quad (66)$$

#### 4.5.0.2 The Roch–Muller–Gillis Model

Three main assumptions are formulated as a starting point of the theory.

(1) The dominant energy term in the hamiltonian describing superparamagnetic crystals is the exchange interaction (which includes also the anisotropy term and the Zeeman term). This determines the alignment of all the electronic spins within the crystal, the sum of which constitutes the superspin. It must be stressed that this assumption decrees a limitation on the MNPs size, since it neglects the existence of *spin waves* into the system, which energy depends on the particle diameter as  $E_{SW} \propto d^{-1}$ , the first assumption of Roch's theory limits its validity to small MNPs.

(2) The rotational correlation time  $\tau_R$  is much larger than the Néel relaxation time  $\tau_N$ : therefore,  $\vartheta$ , the angle between the external magnetic field and the anisotropy axis is assumed constant for each MNP, and the relaxation is determined by averaging over  $\vartheta$ .  $\tau_N \propto \exp V$  while  $\tau_R \propto V$ , thus also this assumption limits the RMG model validity to small particles, in particular with  $d < 20$  nm for magnetite MNPs [47].

(3)  $\tau_N$  is considered equal for all the electronic spin energy levels, which is true if all the spin states possess the same occupation probability. Again, this assumption is valid for low anisotropy energy MNPs, *i.e.* for small MNPs and not for large MNPs.

Once these three assumptions are verified, the relaxation rates are:

$$\frac{1}{T_1} = \frac{32\pi}{1.35 \times 10^5} \hbar \gamma_I^2 \gamma_S^2 \frac{N_a C}{r_d D} \left\langle \sum_{i,j} \frac{e^{-\beta E_i}}{Z} \bar{S}_{ij} K_{ij}^F - 3 \langle S_z \rangle^2 (J_I^F - J_I^A) \right\rangle \quad (67)$$

$$\frac{1}{T_2} = \frac{32\pi}{1.35 \times 10^5} \hbar \gamma_I^2 \gamma_S^2 \frac{N_a C}{r_d D} \left\langle \sum_{i,j} \frac{e^{-\beta E_i}}{Z} \bar{S}_{ij} P_{ij}^F - 2 \langle S_z \rangle^2 (J_0^F + \frac{3}{4} J_I^F) - (J_0^A + \frac{3}{4} J_I^A) \right\rangle \quad (68)$$

where

$$\begin{aligned} \bar{S}_{ij} &:= \frac{S_{-,ij} S_{+,ij} + S_{+,ij} S_{-,ij}}{2}, \\ K_{ij}^F &:= \frac{1}{2} J_-^F + 3 J_+^F + \frac{3}{2} |S_{z,ij}|^2 (J_-^F + J_+^F); \\ P_{ij}^F &:= \frac{1}{4} J_-^F + \frac{3}{2} J_{ij}^F + \frac{3}{2} J_+^F + |S_{z,ij}|^2 (2 J_{ij}^F + \frac{3}{4} J_-^F + J_+^F); \\ J_{\pm}^F &:= J^F(\omega_I \pm \omega_{ij}, \tau_D, \tau_N); \quad J_I^F := J^F(\omega_I, \tau_D, \tau_N); \quad J_{ij}^F := J^F(\omega_{ij}, \tau_D, \tau_N); \\ J_0^F &:= J^F(0, \tau_D, \tau_N); \quad J_I^A := J^A(\sqrt{2\omega_I \tau_D}); \quad J_0^A := J^A(0). \end{aligned}$$

where:

- $\gamma_I$  and  $\gamma_S$  are the gyromagnetic ratio of proton and electron, respectively;
- $N_a$  is the Avogadro number;
- $C$  is the iron molar concentration of MNPs;
- $r_d$  is the minimum approach distance between the protons and the center of the MNPs;
- $\exp(-\beta E_i)/Z$  is the Boltzmann occupation probability;
- $D$  is the diffusion coefficient of the medium (water);
- $\tau_D$  is the diffusion time;
- $\tau_N$  is the Néel relaxation time;
- $\omega_I$  and  $\omega_S$  are the proton Larmor angular frequencies;
- $S$  is the spin operator;

#### 4.5.0.3 Heuristic Model

The two expressions obtained by Roch et al. (Eq. (67) and Eq. (68)) for the evaluation of the longitudinal and transversal relaxation rates are suitable for exact simulations of relaxivity profiles, but are not sufficiently efficient for experimental data fitting, due to the long computational times involved, especially when the size of the magnetic core (directly proportional to the number of spins) is relatively big, *i.e.*  $d > 5$  nm.

A further heuristic approach to the problem was developed by Roch et al. to overcome computational time constraints. The latter is a linear combination of the relaxation rates in the limit of large anisotropy ( $E_b \rightarrow \infty$ ) and zero anisotropy ( $E_b = 0$ ):

$$\frac{1}{T_1} = \frac{32\pi}{1.35 \times 10^5} \mu_{SP}^{*2} \gamma_I^2 \frac{N_a C}{r_d D} \left\{ 7PL_x J_{\Omega}^F + [7QL_x + 3T_x(P + Q)] J_I^F + 3L_{xx} J_I^A \right\} \quad (69)$$

$$\frac{1}{T_2} = \frac{16\pi}{1.35 \times 10^5} \mu_{SP}^{*2} \gamma_I^2 \frac{N_a C}{r_d D} \cdot \left[ 13PL_x J_{\Omega}^F + QL_x(7J_I^F + 6J_0^F) + T_x(3J_I^F + 4J_0^F) + L_{xx}(3J_I^A + 4J_0^A) \right], \quad (70)$$

where

$$\begin{aligned} T_x &:= 1 - L_{xx} - 2L_x; \\ J_\Omega^F &:= J^F(\Omega(\omega_S, \omega_0), \tau_D, \tau_N); \quad J_I^F := J^F(\omega_I, \tau_D, \tau_N); \quad J_0^F := J^F(0, \tau_D, \tau_N); \\ J_I^A &:= J^A(\sqrt{2\omega_I\tau_D}); \quad J_0^A := J^A(0); \quad L_x := \frac{L(x)}{x}; \quad L_{xx} := L^2(x). \end{aligned}$$

$P$  and  $Q$  weigh the linear combination between the spectral density functions  $J^F$  (*Freed spectral density function*) and  $J^A$  (*Ayant spectral density function*), thus quantifying the Zeeman coupling relative to the the anisotropy energy. In particular,  $P = 0$  and  $Q = 1$  for very high anisotropy energy, while  $P = 1$  and  $Q = 0$  for an anisotropy energy equal to zero. In general,  $P + Q \leq 1$ , and  $1 - (P + Q)$  valuates the magnetization fraction that does not contribute to the relaxation, because of a too fast precession.

While in recent times the ability of the RMG model (Eq. (69)) of reproducing the experimental data of the longitudinal relaxivities ( $r_1$ ) of SPM compounds has been frequently verified by the scientific community, scarce accordance between the experimental data and the theory of transversal relaxation (Eq. (70)) has been pointed out. Consequently there is a need to implement this part of the model.



# 5

---

## HADRON THERAPY AND HYPERTHERMIA

---

**I**N this Chapter, the results of the Italian National Institute for Nuclear Physics (INFN) Hadromag project are presented. The author has been part of this collaboration for the entire duration of her PhD program, in collaboration with the University of Milan, the University of Florence, the University Roma Tre, the Italian National Council for Research - Institute for the Chemistry of Organometallic Compounds, the National Centre for Oncological Hadron Therapy (CNAO) in Pavia, and the National Institute of Tumours (INT) of Milan.

The project aims at investigating the possible cooperative action of Hadron Therapy (HT) and Hyperthermia (Hyp) applied to pancreatic tumour cells. The results were published in [25].

### 5.1 RATIONALE

Hyperthermia can be used "as is" or in combination with further therapies: common goals are increasing the sensitivity of tumor cells to ionizing radiation, leading to an overall enhancement of drug cytotoxicity, facilitating the efficacy of immunotherapy, and so on.

Hyperthermic therapy, when applied by itself, does not appear to be a very effective anti-tumour treatment, thus it is generally used as an adjuvant treatment for cancer. Indeed synergistic treatments have been attempted in recent years with the combined use of hyperthermia and other therapies. As far as these therapies are concerned, cancer can be treated by surgery, chemotherapy, radiation therapy, synthetic lethality, hormonal therapy, targeted therapy and so on. Among these, in conventional radiation therapy, beams of x-rays are delivered to the patient to destroy tumour cells. When, instead, the irradiating beams are made of charged particles (protons and other ions, such as carbon), radiation therapy is called HT.

The main advantage of HT with respect to x-ray radiotherapy is that it allows to maximize the destruction of cancerous tissues while minimizing collateral effects on surrounding healthy tissues. Furthermore, while in conventional radiotherapy the DNA damage is modest, on the contrary, in the HT the number of breaks allows the destruction even of tumors resistant to conventional therapy.

For these reasons we decided to investigate the cooperation of HT and Hyperthermia on pancreatic cancer cells (BxPC<sub>3</sub>). Pancreatic cancer patients have an extremely poor survival prognosis. Despite decades of research, the overall survival rate at five years is still at 5–10%. The cancer spreads rapidly, and it is rarely detected in its early stages: this is the reason why it is often fatal. Because the initial symptoms are vague and nonspecific, most people have advanced-stage disease by the time the diagnosis is made, and complete surgical removal is not always possible. Radiotherapy is often offered to patients, however only limited results are usually achieved: this happens both because pancreatic cancer is radioresistant and due to the radiosensitivity of the normal tissues and organs surrounding the tumor. For all these reasons, a variety of anti-tumoral techniques has been applied to BxPC<sub>3</sub> cells, and their impacts have been studied in others works. For instance, El Shafie et al. [48] evaluated the cytotoxic effect achieved by treating this cell line in vitro with a combination of x-rays/carbon ion irradiation and gemcitabine. Additive effects in cytotoxicity were achieved by combining both photon and carbon irradiation with gemcitabine; neither photon nor carbon ion irradiation led to the observation of radiosensitizing effects. In addition, Ludwig et al. [49] have recently stressed the different effects of magnetic heating mediated on the one hand by nanoparticles, and on the other hand by hot air, highlighting the superiority of the intrinsic form of heating. The latter method essentially increased the number of cells undergoing necrosis, triggered the formation of reactive oxygen species (ROS) and reduced the expression of many proliferation markers (Ki-67, TOP2A, TPX2) at mRNA level. Finally, the development of a novel strategy to strengthen the effect of chemotherapy and/or overcome the chemoresistance has been studied in many works but a systematic study of clonogenic survival of BXPc<sub>3</sub> after chemotherapy seems to be present in literature.

## 5.2 CONVENTIONAL RADIOTHERAPY

Radiation therapy using x-rays plays an important role in the treatment of cancer pathologies since the discovery of x-rays by Röntgen in 1895; it is the most frequent form of post-surgical therapy. The key problem associated to this therapy is that of irradiating the whole target volume so that all cancer

cells can be killed, thus minimizing the dose delivered to the surrounding healthy tissues.

### 5.2.1 Photon-tissue interaction

Photon absorption in tissues can be ascribed to three interactions: *pair production*, the *photoelectric effect* and the *Compton effect* [50–53].

**PHOTOELECTRIC EFFECT** When an incoming photon collides with a tightly bound electron ( $e^-$ ), the photon energy  $h\nu$  is transferred to the electron in its entirety. The electron departs with most of the energy from the photon

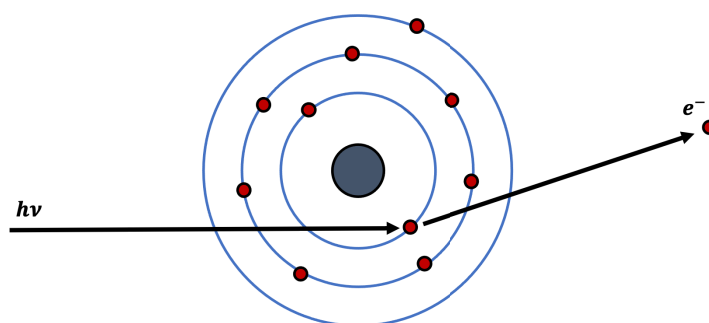


Figure 18: Photoelectric effect

(the energy required to extract an electron from the material needs to be considered) and starts ionizing the surrounding molecules. This interaction depends on  $h\nu$ , as well as the atomic number of the tissue; the lower the energy and the higher the atomic number, the more likely it is that the photoelectric effect will take place.

The energy range in which the photoelectric effect predominates in tissues is about 10–25 keV. A sketch of the process is presented in Fig. 18.

**COMPTON EFFECT** A photon collides with a quasi-free electron, that is not tightly bound to the atom, and, as sketched in Fig. 19, both the photon and electron are scattered. The photon can then continue to have additional interactions, since  $h\nu' < h\nu$ , and the  $e^-$  starts ionizing with the energy acquired from the photon.

The probability of this process diminishes with the energy of the incoming photon, and it does not depend on the atomic number of the material. The Compton effect is the predominant interaction occurring in radiotherapy treatments, since the photon beams for radiation treatments usually have an energy of about 6–20 MeV.

**PAIR PRODUCTION** The photon gives up its energy to the nucleus it is interacting with and a pair of positively and negatively charged electrons ( $e^+$

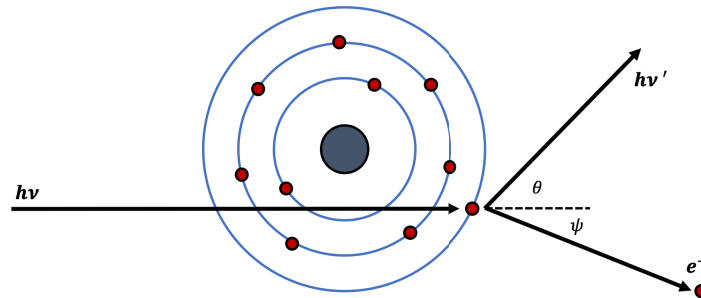


Figure 19: Compton effect

and  $e^-$ ) is produced in the process. The positive electron ( $e^+$ ) ionizes until it combines with a free electron, and two photons scattering in opposite directions (back-to-back) are generated.

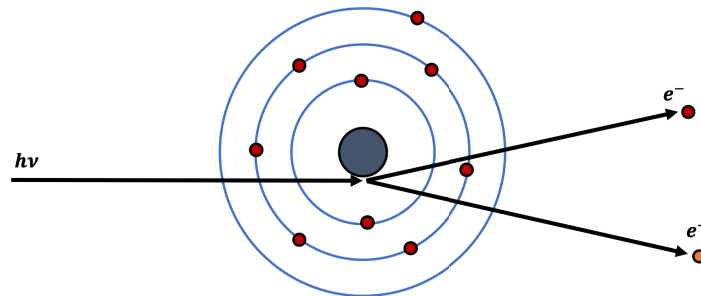


Figure 20: Pair production

The probability of this effect increases with the logarithm of the energy of the photon and depends on the atomic number of the material. For energies lower than 25 MeV, pair production is the main mechanism of photon-matter interaction and, in clinic, it occurs to some extent in routine radiation treatment with high-energy photon beams.

### 5.2.2 Dose distribution

The absorbed radiation dose is directly related to the beam energy. When treating a patient with radiation, accurate measurement of the absorbed dose is of paramount importance. Depositing energy in the tissues causes damage to the DNA and hinders or blocks the ability of the cell to replicate indefinitely, which represents the main goal of the therapeutic treatment. The absorbed radiation dose is defined as the amount of energy (joule) absorbed per unit mass (kg). This unit, known as gray (Gy), has replaced the rad unit used in the past (100 rads = 1 Gy; 1 rad = 1 cGy).

The dose distribution of a photon beam hitting a patient is shown in Fig. 21.

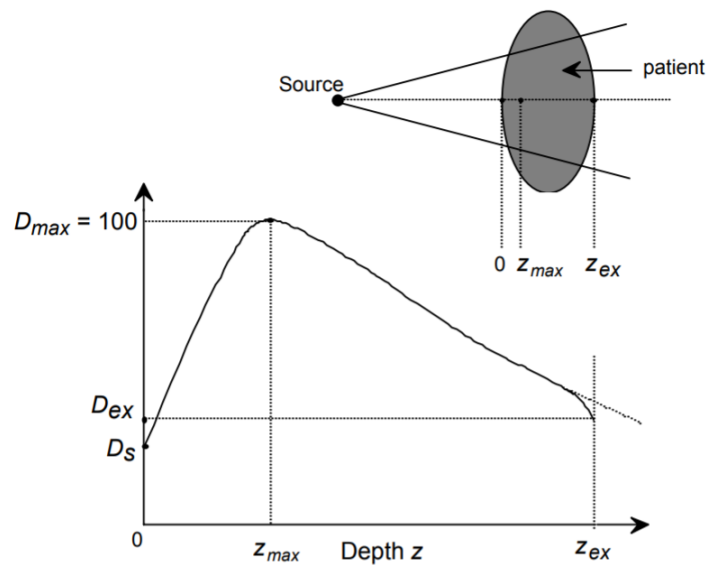


**Figure 21:** Profile dose vs depth using a photon beam.  $D_s$  is the dose at surface,  $D_{ex}$  is the dose at the exit side and  $D_{max}$  the maximum one [53].

At the patient's skin, a certain dose is delivered and, as the beam penetrates the patient, the dose increases rapidly at first (an effect caused by the range of the secondary electrons), reaches a maximum and then decreases almost exponentially. The maximum of the energy deposition for x-rays is located at a small depth of penetration; this is the main reason why it is difficult to accurately treat tumors located deep in the body while preserving the surrounding healthy tissues.

## 5.3 HADRON THERAPY

Since its first use, radiotherapy has seen numerous technological improvements, which have rapidly entailed better clinical results. The main goal was to improve the ratio between an optimal dose in the tumour and a dose as low as possible in the healthy tissues.

Within this framework, protons and carbon ions offer a better physical dose distribution.

### 5.3.1 Interaction Mechanisms

Charged particles possess a much greater mass than electrons and, if accelerated, are consequently characterized by strong interactions with the matter they pass through. As they cross the material, charged particles

lose energy primarily by *inelastic collisions* with the atomic electrons, resulting in ionization and atomic excitation. On the contrary, the amount of energy lost to *Coulomb interactions* with the nuclei inside the material is very small [54]. For charged particles other than electrons, the mean ionization energy loss (or *Electronic Stopping Power*) can be described by the Bethe–Bloch equation [55]:

$$-\frac{dE}{dx} = 2\pi N_A r_e^2 m_e c^2 \rho \frac{Z}{A} \frac{z^2}{\beta^2} \left[ \ln \left( \frac{2m_e \gamma^2 v^2 W_{\max}}{I^2} \right) - 2\beta^2 - \delta - 2\frac{C}{Z} \right], \quad (71)$$

where, in order of appearance,  $N_A$  is the Avogadro number,  $r_e$  the classical electron radius, and  $m_e$  its mass,  $\rho$  the density of the absorbent material,  $Z$  the atomic number of the absorbent material,  $A$  the mass number of the absorbing material,  $z$  the charge of the incident particle in units of  $e$ ,  $\beta = v/c$  (where  $v$  is velocity of the incident particle in the medium and  $c$  the speed of light),  $\gamma = 1/\sqrt{1 - \beta^2}$ ,  $W_{\max}$  the maximum energy transferred in a single collision,  $I$  the average excitation potential,  $\delta$  the correction of density (high energy), and  $C$  is the shell correction (low energy). The stopping power for protons and carbon ions as a function of the energy of the beam is shown in Fig. 22. The  $1/\beta^2$  dependence of the stopping power results in greater energy loss as the kinetic energy of the particle decreases, resulting in the characteristic *Bragg Peak*. Since energy losses are statistical processes, the particle range is not the same for all particles constituting the beam (*range straggling* or *energy straggling*). The effect is the broadening of the Bragg peak.

Regarding anticancer treatments, one of the main aims is to have a full irradiation coverage of the target tumor volume. Longitudinally this is achieved by superimposing different beams with slightly different energies and weights, as depicted in Fig. 23, generating a Spread Out Bragg Peak (*SOBP*) that deposits the wanted dose in the treatment volume.

## 5.4 BIOLOGICAL EFFECTS

At the tissue level, the microscopic spatial energy distribution plays a key role in determining the biological effects caused by a type of radiation. For equal absorbed dose, the biological response varies according to the type of particle that makes up the beam.

The Linear Energy Transfer (*LET*) is the average energy deposited by the particle per unit length ( $\text{keV}/\mu\text{m}$ ) in the absorber medium (cell/tissue):

$$\text{LET} = \frac{dE}{dx}. \quad (72)$$

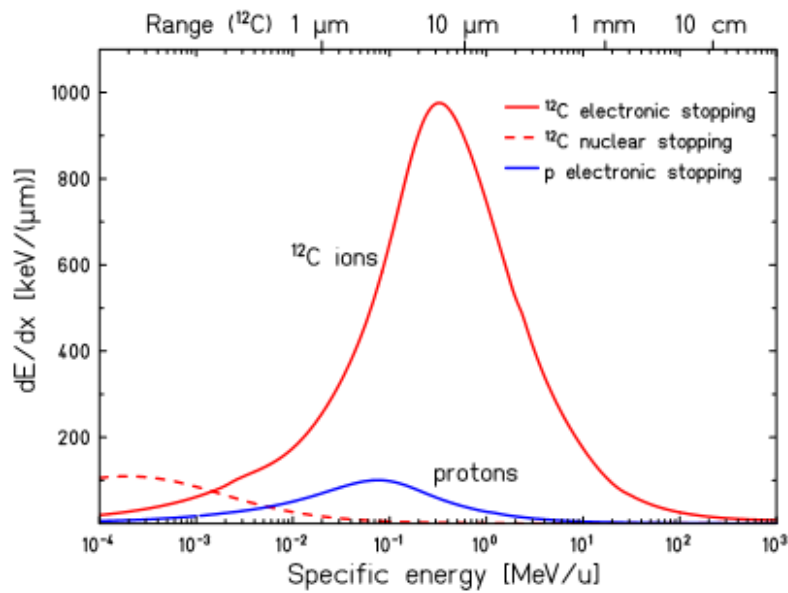


Figure 22: Stopping power of protons and carbon ions as a function of their energy [56].

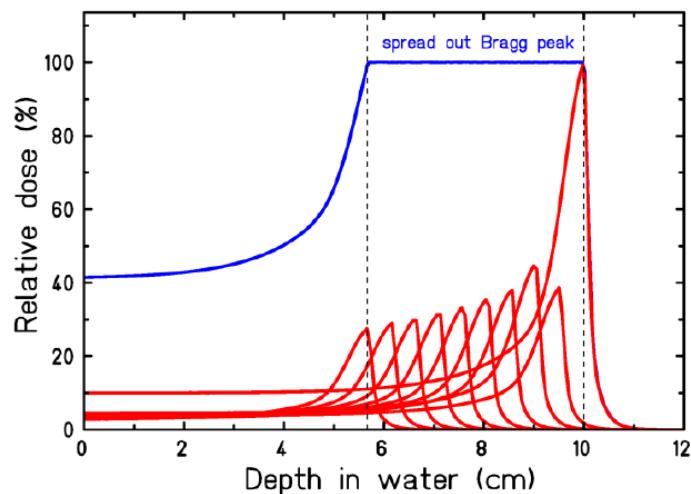
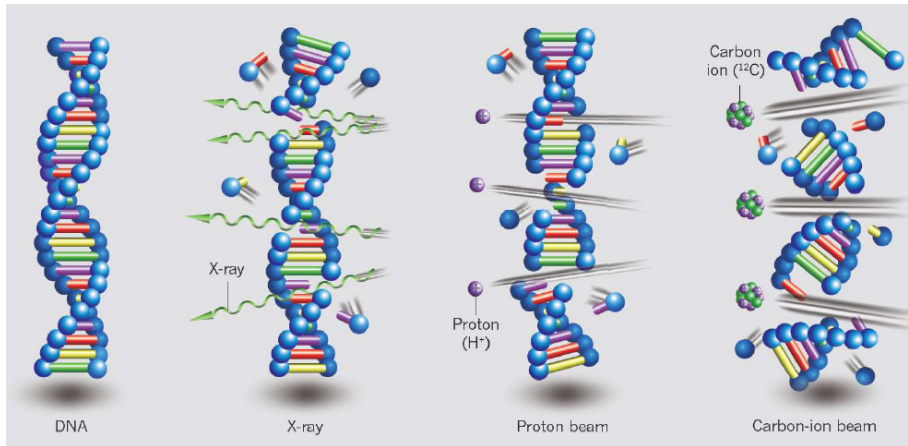


Figure 23: The principle of the construction of a Spread Out Bragg Peak (SOBP) in hadron therapy [57].

By interacting with biological tissues, the radiation damages the DNA of the cells. Damage to DNA can be of two types: damage to the single strand of DNA (*Single-strand break*, SSB) or damage to the double strand of DNA (*Double-strand break*, DSB). Mortality is linked to the type of damage induced in the DNA chain: particularly important is clustered damages, especially double-stranded ones, as the cell will have greater difficulty in



**Figure 24:** Schematic representation of DNA damage produced by x-rays, protons and carbon-ions. [58].

repairing them. High LET (carbon ions) radiation causes greater and more concentrated damage to the cell nucleus (Fig. 24).

Non-lethal injuries can be repaired without any consequences, or cells can be delayed in dividing. When, instead, a lethal lesion occurs, the cells can die from apoptosis (they die before division or soon after by fragmentation into smaller bodies) or permanently lose their clonogenic capacity after the first divisions. A further distinction can be made based on the way in which the radiation damages cells. When a charged particle directly ionizes a biologically important molecule within the cell, such as DNA, it is called the *direct action* of radiation. On the other hand, when cell damage occurs as a result of ionization of intermediate molecules such as water, the action of the radiation is defined as *indirect*. Most of the damage induced by low-LET radiation (such as photons) is due to indirect action, while for high-LET radiation, such as carbon ions, the contribution of indirect action to damage is quite negligible.

Protons have a higher LET than photons, but their radiobiologic properties do not differ substantially from those of photons. Heavier ions such as carbon ions share the favorable physical properties of protons but also have a biologic advantage [59].

It is useful to introduce the Relative Biological Effectiveness (**RBE**), as the ratio between the dose of a standard radiation, x or  $\gamma$  rays ( $D_{\text{ref}}$ ), and the dose of a test radiation ( $D_{\text{test}}$ ) required to produce the same biological effect.

$$\text{RBE} = \frac{D_{\text{ref}}}{D_{\text{test}}}. \quad (73)$$

The RBE depends on many parameters including the LET of the radiation, the dose, the type of particle, the energy, the cell type and the studied endpoint (see Fig. 25). Furthermore, from experiments carried out with car-



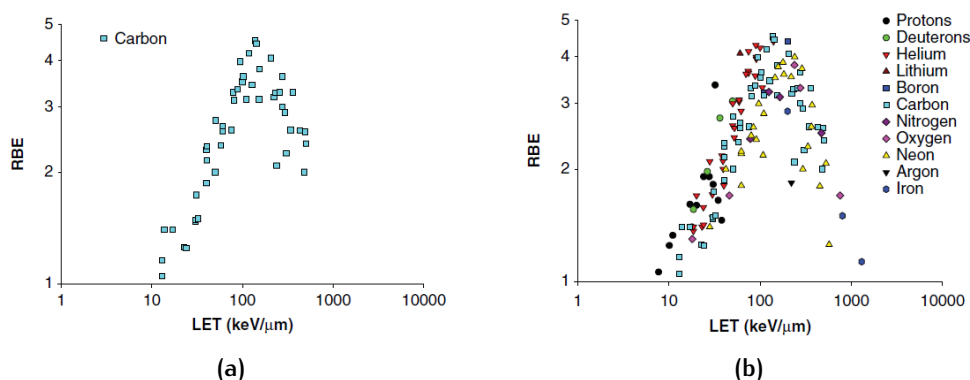


Figure 25: (a) RBE-LET plot for V79 cells for carbon ions. (b) RBE-LET plot for V79 cells for different particles type [60].

bon ions it was found that the higher dose per fraction corresponds to the lower RBE, both of the tumor and of normal tissues, even if with a different decreasing rate.

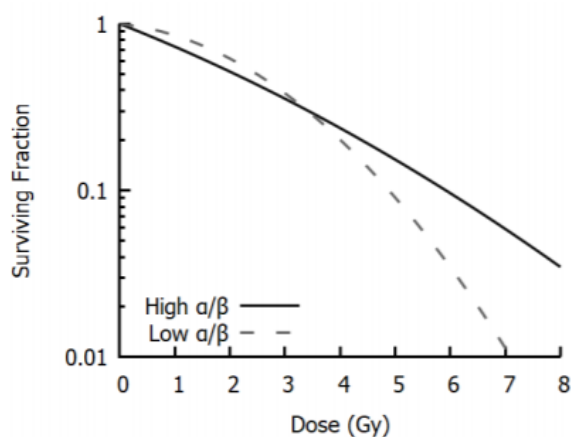


Figure 26: Linear Quadratic curves in case of high and low  $\alpha/\beta$  ratios. High  $\alpha/\beta$ : cell killing rate is constant for all doses, low  $\alpha/\beta$ : greater killing per unit dose at higher doses [61].

Usually RBE is determined considering the dose needed to reduce the clonogenic survival (CS) of irradiated cell to 10%. CS of a single cell is defined as its ability to give rise to a colony of daughter cells. It often happens that, after being damaged, a single cell is able to divide two or three times before finally losing its clonogenic capacity. For this reason, a cell is conventionally considered to have survived from a clonogenic point of view when it produces a colony of at least 50 cells.

The dose-effect relationship (see Fig. 26) is usually parameterized according to the so-called Linear Quadratic (LQ) model:

$$CS(D) = e^{-\alpha D - \beta D^2}, \quad (74)$$

where CS is the survival fraction, D is the absorbed dose, and  $\alpha$  and  $\beta$  are parameters to be determined experimentally or by means of a radiobiological model. The  $\alpha/\beta$  ratio is linked to the radiosensitivity of cells. For conventional irradiation with photons a high  $\alpha/\beta$ -ratio ( $> 6$  Gy) is common in radiosensitive cells and early responding tissues including many tumors. A low  $\alpha/\beta$ -ratio (1–6 Gy) is often observed for radioresistant cells or late responding tissue types [57].

Densely ionizing radiations give rise to a cell survival curve that depends exponentially on the radiation dose. For low-LET radiation, on the other hand, the curve shows a ‘shoulder’, which is typically correlated with DNA repair capacity. These two contributions to cell killing lend themselves to an intuitive interpretation: the  $\alpha$  term corresponds to a death from ‘single hit’ events—*i.e.* lethal damage caused by a single incident particle—whereas the  $\beta$  term corresponds to cell death from ‘multiple hits’, *i.e.* caused by the interaction of damage from different radiation tracks; this term appears in the clonogenic survival fraction as a quadratic contribution.

## 5.5 ADVANTAGES OF HADRON THERAPY

Hadron Therapy offers some important advantages with respect to x-ray radiotherapy:

- i The damage induced on the tumor tissues is generally higher; as explained above, a variety of DNA lesions are induced along the radiation track, *e.g.* DNA base damage, sites of base loss, DNA SSBs, DNA DSBs, and complex DNA damage (two or more DNA lesions in close proximity);
- ii As a consequence of point (i), HT allows the treatment of radioresistant tumors [62];
- iii Since the majority of the energy is deposited inside the tumor site due to the Bragg peak, thus maximizing the damage to cancer cells, the healthy cells in the surrounding volume are kept safe;
- iv The particle beam manages to remain more collimated along the entire path; hence, any side effects to the adjacent healthy tissues can be drastically reduced.

Unfortunately, for a long time one of the most striking disadvantages of particle therapy has been the high cost of its technical realization and operation. Large cyclotrons or synchrotrons were needed to accelerate protons and heavier ions to the energy levels required for the treatment of deep tumors. Today, thanks to advances in technology, hospital proton accelerators have been designed to overcome these limits and offer the benefits of hadron therapy to more patients. High accuracy and reproducibility of patient positioning, together with high quality images for treatment planning, are prerequisites for this type of treatment.

## 5.6 HADRON THERAPY AND HYPERTHERMIA

When looking for alternative therapies with respect to irradiation, hyperthermia (Hyp) stands out as one of the most promising solutions, and many clinical tests have already investigated it for its efficacy [63–67]. The main reason for this is that cancer cells are intrinsically sensitive to hyperthermia. The development of the tumor is indeed highly disorganized: the consequent distortion in blood perfusion leads to an environment characterized by low pH and hypoxia, which may favour cell death by temperature raise [68, 69]. Conversely, healthy tissues rarely suffer from the same conditions of hypoxia and high acidity, and are thus kept safe. The local temperature raise in tumor tissues has been realized historically by following different routes, *e.g.* bath heating [70], microwave irradiation [71], radiofrequency waves [72], focused ultrasounds [73, 74], capacitance hyperthermia [75], concentrated laser light [76], magnetic fluid hyperthermia [32, 77–84]. More recently, innovative techniques based on coupling different kinds of hyperthermia have been investigated, *e.g.* magnetic and ultrasonic hyperthermia, or magnetic and phototherapy hyperthermia. In a 2017 literature-based review by Peeken et al. [85], the authors show the current hyperthermia techniques for delivering heat and controlling the final temperature, describing the different mechanisms of hyperthermia. A different viewpoint was adopted by Datta et al. [86], who investigated the advantages of using multifunctional MNPs in local tumor magnetic fluid hyperthermia, and also discussed their role as multi-mode theranostic vectors. A few cases of hyperthermia combined to hadron therapy have recently been reported. The treatment of two patients with unresectable soft-tissue sarcomas in the lower leg was reported Datta et al. [87]; they were treated once a week with local hyperthermia via RF waves, in association with a daily proton therapy (for 7 weeks). With this technique, functional limb preservation was achieved with nearly total tumor control. In addition to this case, Maeda et al. [88] suggested that applying hyperthermia (water bath at  $T = 42.5\text{ }^{\circ}\text{C}$  for 1 hour) immediately after radiation exposure

may induce hyper-sensitization to hadron radiation, *e.g.* protons, carbon ions. As a third example, Ahmad et al. [89] investigated on this effect of cell sensitization to proton therapy by using A549 lung cancer cells treated with hyperthermia ( $T = 42.5\text{ }^{\circ}\text{C}$ , by means of a heating pad) and to proton irradiation. Albeit the results are still preliminary in nature, the authors succeeded in collecting data indicating a cell survival fraction dropping on average by 10–15%, both for doses of 2 Gy and for doses of 4 Gy. It is worth mentioning that the combined effect of radiotherapy, hyperthermia and MNPs could have an additive or synergistic action; this feature is rather common in cancer treatments involving combinations of techniques, *e.g.* radiotherapy combined with chemotherapy, hyperthermia, surgery, immunotherapy, and so forth. For example, Dong et al. [90] demonstrated a synergistic therapeutic strategy against osteosarcomas when hyperthermia is associated to elaborately catalytic Fenton reactions achieved by using nanoparticles based on  $\text{Fe}_3\text{O}_4$  and  $\text{CaO}_2$ . Likewise, Ito et al. [91] reported on a combination of antibody therapy with magnetic hyperthermia showing an additive effect against HER2-overexpressing cancer. The overall goal being that of killing tumour cells, both additive and/or synergistic effects have been shown to reduce the survival of tumor cells. Despite sparse data related to radiotherapy plus hyperthermia being available in the scientific literature, systematic studies of the possible combination of hadron therapy and hyperthermia coadiuvated with MFH for local temperature raises are still lacking.

## 5.7 EXPERIMENTAL TREATMENT PROTOCOL

The ultimate goal of the investigation was to evaluate the potential synergy or additive effect between hadron therapy and hyperthermia on a culture of pancreatic-cancer BxPC<sub>3</sub> cells. The general experimental protocol comprised three different treatment modes, in order to discriminate the effect of each component of the combined treatment: irradiation alone (C-ions or photons), MNPs and irradiation, MNPs and irradiation and hyperthermia (see Fig. 27).

The samples, *i.e.* cells either incubating MNPs or without MNPs, were irradiated by either carbon-ion beams at the synchrotron facility at CNAO (Pavia, Italy), or by means of photons using a 6 MV linear accelerator at INT (Milan, Italy). Regarding carbon-ion irradiation, T25 flasks (25 cm<sup>2</sup> surface) were used to store the cells and were later placed in a vertical position inside a water phantom (Fig. 28). This was then positioned at the isocenter on the treatment table; this location corresponded to the position of the mid spread-out Bragg peak (SOBP), at a depth of 15 cm.

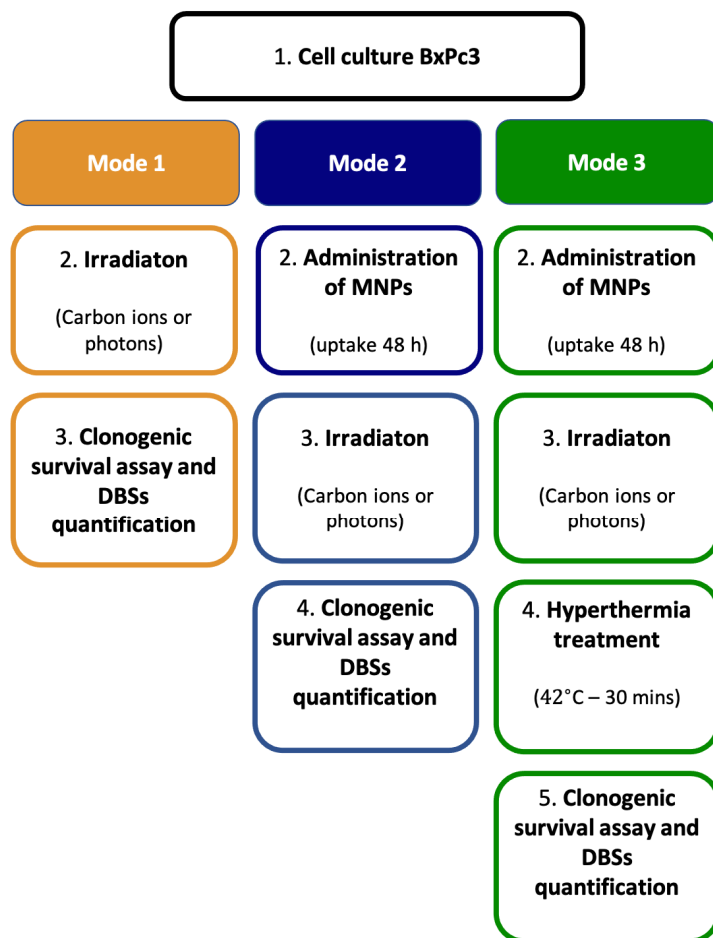


**Figure 27:** The three different treatment modalities employed in the experiments. In mode 1, the clonogenic survival (CS) was determined after simple irradiation; in mode 2, CS was determined after administering MNPs and irradiation; in mode 3, CS was determined after administering MNPs, then performing irradiation and subsequent hyperthermia (Hyp). The acronym DSB corresponds to the breaking of both strands of DNA.

The SOBP, characterized by a width of 6 cm and localized at a depth from 12 to 18 cm in water, was achieved with active beam energy modulation, employing 31 different energies (246–312 MeV/u, and a linear energy transfer (LET) of about 45 keV/ $\mu\text{m}$ ). The samples were irradiated with different doses in the range 0–2 Gy.

As to the photons, irradiation of cell cultures by means of photon-beam doses in the range 0–7 Gy was carried using a 6 MV linear accelerator (VARIAN Clinac 2100C, Varian Medical Systems, Palo Alto, USA). The flasks containing the cells were placed horizontally at the isocentre in a water phantom at a depth of 5 cm, and they were irradiated using a vertical beam field with a section equal to  $20 \times 20 \text{ cm}^2$ .

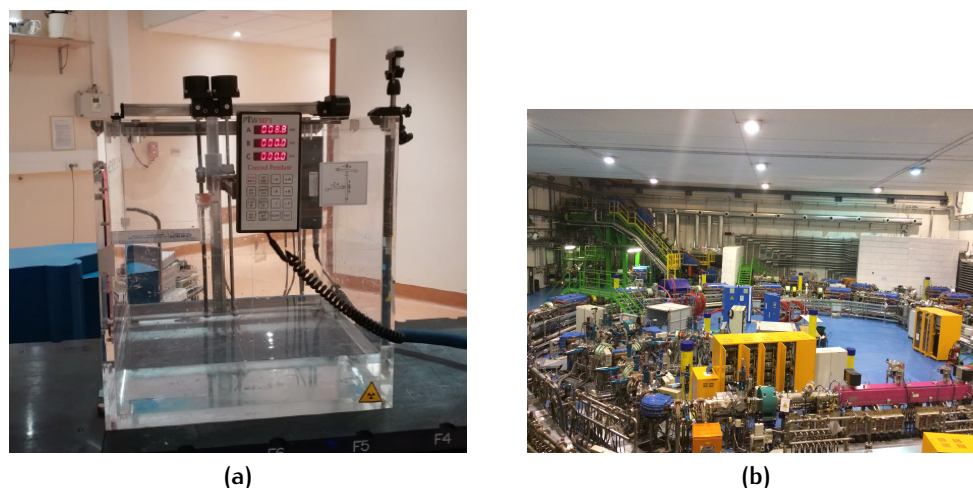


Figure 28: (a) Water phantom used at CNAO for carbon ions irradiation. (b) Synchrotron-based facility at CNAO, in Pavia, Italy.

In order to carry out a section of the hyperthermic process via magnetic fluid hyperthermia, human pancreatic adenocarcinoma BxPC<sub>3</sub> cells were fed the magnetic nanoparticles with a culture-medium concentration of 50  $\mu\text{g}/\text{ml}$ . To favour the cells' uptake and thus improve the MFH efficacy, the cells were incubated for 48h. For mode 3 in Fig. 27, *i.e.* the combined approach, hyperthermia was applied to the cell samples incubating MNPs after the irradiation. The temperature had to be increased from 37°C to 42°C, *i.e.* a temperature difference of  $\Delta T = 5^\circ\text{C}$ , at which point the temperature was kept constant; the heating was obtained both through a thermalization system, *i.e.* circulating water from a heat bath around the vials containing the sample, and magnetic hyperthermia, realized by applying an AMF of amplitude  $H = 19.5\text{ mT}$  and frequency  $f = 109.8\text{ kHz}$ . These parameters are consistent with current clinical trials [92]. The hyperthermia setup is sketched in Fig. 34. The amount of up-taken MNPs was estimated by Inductively Coupled Plasma-Optical Emission Spectrometry (ICP-OES) and found to be on average 20 pg/cell, calculated over different experiments. About 40% of the heating can be ascribed to the application of the magnetic field, whereas the remaining temperature increase is achieved by means of the thermalization system. Because of the limited cell volume, the amount of 20 pg/cell corresponds to an almost full inner part and surface of the cell; hence, the value shown here corresponds to a heat release close to the highest possible value.

In the end, the biological effect of the various different treatment modes was assessed in two ways:

- After two weeks, a clonogenic assay was performed. Clonogenic cell survival (CS) assays measure the cell's ability to bring forth a viable



colony consisting of 50 cells at least. When studying cellular sensitivity to irradiation, they represent an unparalleled gold standard [93];

- The number of non-repairable Double Strand Breaks (DSBs) per cell was estimated after 6 and after 24 hours. This was achieved through observation and counting of persistent repair foci, which are DSBs markers. This study was restricted to carbon ions irradiation.

## 5.7.1 Magnetic Nanoparticles - Synthesis and Carachterization

### 5.7.1.1 Synthesis

For this study, spherical Fe<sub>3</sub>O<sub>4</sub> core NPs coated with meso 2,3-dimercaptosuccinic acid were used. Their synthesis was performed by the group of Dr. Claudio Sangregorio at the University of Florence, by applying a thermal decomposition procedure, starting from metal-organic precursors in a high-temperature boiling solvent, in a solution with an appropriate surfactant.

In brief, Fe(acac)<sub>3</sub>, Oleylamine and Oleic Acid (8 mmol, 32 mmol and 32 mmol, respectively) have been dissolved in benzyl ether (80 mL) and stirred magnetically under a flow of nitrogen for a time interval of 15 minutes. The ensuing mixture was heated to reflux (~ 290 °C) at a heating rate of 25 °C/min; this temperature was then kept constant for 90 minutes under a blanket of nitrogen and robust stirring. The black-brown mixture was then cooled until room temperature; after this, the addition of ethanol (60 mL) caused the precipitation of a black powder.

The product was separated magnetically using a permanent magnet, then washed several times with ethanol and finally re-dispersed in toluene. In order to suspend MNPs in water (recommended for any application in biomedical field) the Oleic Acid (OA) coating was replaced by meso 2, 3-dimercaptosuccinic acid (DMSA). In particular, 400 mg of MNP@OA were dispersed in toluene (60 ml), added to a solution of DMSA (600 mg) in Dimethyl Sulfoxide (DMSO) (15 ml). Afterwards, (i) the two solution were sonicated for 1 h, and finally (ii) incubated at room temperature for a time interval of 12 h in a rotating agitator; (iii) the precipitate was separated magnetically using a permanent magnet, (iv) washed several times with DMSO first and then ethanol, and finally it was re-dispersed in milliQ water (80 ml); (v) at this point, the suspension was basified to a pH equal to 10 using sodium hydroxide, and later adjusted to a pH equal to 7.4 with the addition of hydrochloric acid to make it stable.

It is worth noting that, in addition to the good colloidal stability guaranteed by DMSA in water, DMSA coating MNPs are widely used in the biomedical field because this coating allow high MNPs uptake rates by different type of cell lines, thanks to a favourable interaction with the cell membrane [94, 95].

### 5.7.1.2 XRD

The nature of the iron oxide obtained at the end of the synthesis procedure was confirmed as magnetite by X-ray Diffraction (XRD) analysis. A Bruker D8 Advance diffractometer was used to make all the measurements; this instrument was equipped with a graphite monochromator, it used  $\text{CuK}\alpha$  radiation ( $\lambda = 1.54178 \text{ \AA}$ ) and operated in  $\vartheta$ - $2\vartheta$  Bragg-Brentano geometry at 40 kV and 40 mA. Results are shown in Fig. 29: the peaks of the

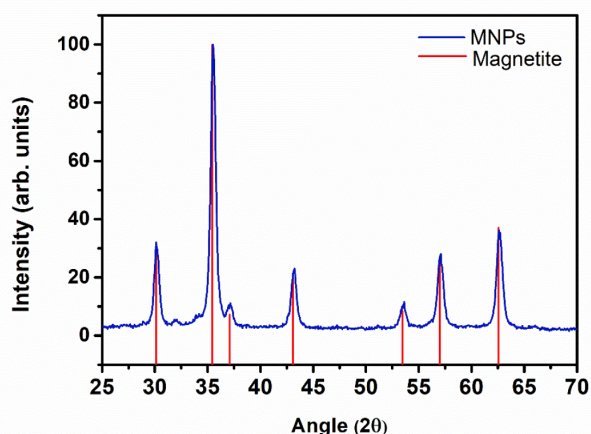


Figure 29: Powders XRD patterns of  $\text{Fe}_3\text{O}_4$  MNP; comparison of diffraction peaks with the reference pattern (red vertical bars) of magnetite (JCPDS 19-0629).

spectrum of the sample match the reference pattern (JCPDS 19-0629) as regards both position and intensity. The peaks are those characteristic of the face-centered-cubic structure, typical of inverse-spinel (magnetite, maghemite). The lattice parameter,  $a$ , and the mean crystallite diameters,  $d_{\text{XRD}}$ , were evaluated by means of the T.O.P.A.S.<sup>®</sup> [96] software (Bruker) using a method called *Fundamental Parameter Approach*, by taking into account a cubic space group  $\text{Fd-}3\text{m}$  (magnetite). The lattice parameter ( $a = 8.387 \text{ \AA}$ ) is not far from the one that would be expected for magnetite ( $8.396 \text{ \AA}$ ); this suggests a low degree of surface oxidation of the magnetic nanoparticles, which should reasonably consist of a magnetite core surrounded by a thin maghemite shell. This deduction will be confirmed and completed by the magnetic measurements reported in Section 5.7.1.5. Scherrer analysis yielded a crystallite diameter of  $d_{\text{XRD}} = 18.7 \pm 0.4 \text{ nm}$ , comparable to the one derived by TEM measurement (a detail that will be shown in the following section). These features suggest that the magnetic nanoparticles are single crystals, and that they present a high degree of crystallinity.



### 5.7.1.3 TEM

For a qualitative evaluation of the particles shape and the measurements of the core size, Transmission Electron Microscopy (TEM) was employed. In particular, the core morpho-dimensional characteristics were studied using a CM12 PHILIPS TEM (LaF<sub>6</sub> source, operating at 100 kV). A representative TEM image is reported in Fig. 30: this clearly shows the almost spherical shape of the particles; from the histogram of the size distributions, a value for the core diameter of  $d_{\text{TEM}} = 19.2 \pm 3.6$  nm was extracted.

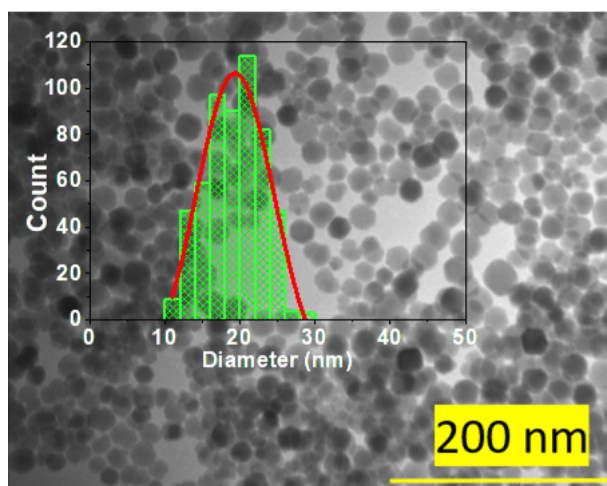


Figure 30: TEM image of magnetite MNPs. Histogram reporting the core size distribution was obtained by TEM statistical analysis, and fitted with a Log-Normal function.

### 5.7.1.4 DLS

The Dynamic Light Scattering (DLS) technique was used to estimate the MNP hydrodynamic size and Z-potential (Fig. 31). Measurements were carried out by means of a Malvern Zetasizer ZS, by Malvern Instruments Ltd., UK. The successful DMSA functionalization was confirmed by  $d_{\text{DLS}} = 27 \pm 8$  nm at pH 7.4. The Z-potential measurements show that the surface charge of the MNPs is negative,  $Z_{\text{pot}} = -30.5 \pm 7.5$  mV at pH 7.4. The negative surface charge is attributed to the carboxyl groups of the DMSA molecules and the high zeta potential value justifies the stability of the sample in water.

### 5.7.1.5 Magnetic Measurements

Magnetic characterization of the sample was performed by means of a SQUID magnetometer (Quantum Design MPMS) operating in the 2–350 K temperature range with applied fields up to 5 T. The powdered sample was

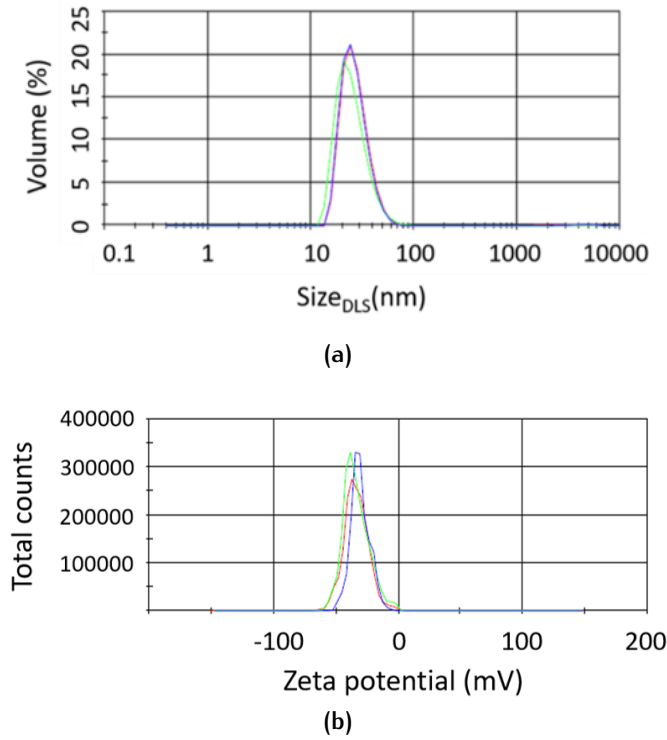


**Figure 31:** (a) DLS diameter ( $d_{DLS}$ ) measurements at pH 7.4. (b) Zeta potential measurements at pH 7.4. Three different measurements have been performed (green, blue, red lines).

hosted in a Teflon-tape and then pressed in a pellet to keep the nanocrystallites from aligning to a preferential orientation under the magnetic field. The ensuing magnetization values were normalized by the weight of the amount of ferrite inside the sample, and expressed in  $\text{Am}^2/\text{kg}$  of ferrite. Hysteresis loops were acquired at both low ( $T = 5 \text{ K}$ ) and high temperature ( $T = 300 \text{ K}$ ) in the field range  $\pm 5 \text{ T}$  (Fig. 32).

At  $T = 5 \text{ K}$ , the MNPs showed a hysteretic behavior with a coercive field  $\mu_0 H_c = 30 \pm 2 \text{ mT}$  (see the inset in Fig. 32), while a negligible opening-up of the hysteresis loop is observed at  $T = 300 \text{ K}$  (less than  $0.3 \text{ mT}$ , comparable to the remaining field). These results indicate that the magnetic nanoparticles have a superparamagnetic behavior, as expected for magnetite-based magnetic nanoparticles of comparable size. The saturation magnetization  $M_s$  has a value of  $83 \text{ Am}^2/\text{kg}$  at  $5 \text{ K}$  and  $74 \text{ Am}^2/\text{kg}$  at  $300 \text{ K}$ , *i.e.* a very high value for both temperatures; moreover, this value represents about about the 90% of the bulk value of  $84 \text{ Am}^2/\text{kg}_{\text{Fe}_3\text{O}_4}$  and very close to the  $\gamma - \text{Fe}_2\text{O}_3$  value of  $78 \text{ Am}^2/\text{kg}$  at room temperature [97]).

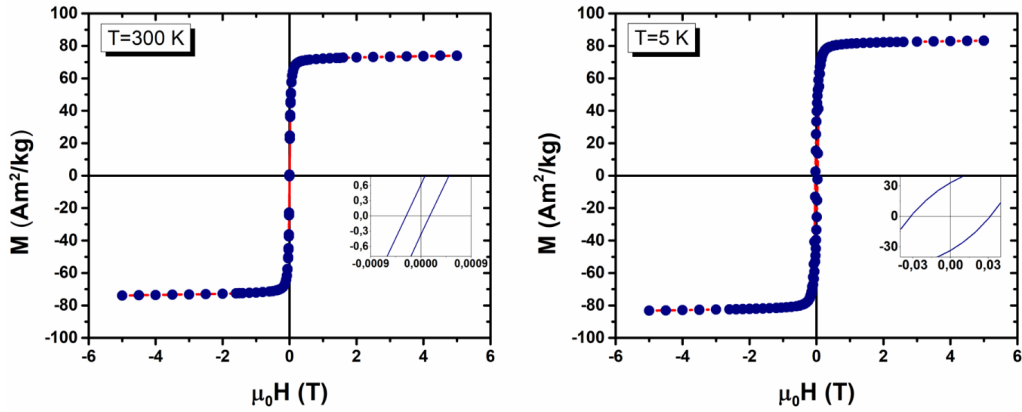


Figure 32: Hysteresis loop measured at 300 K (left) and 5 K (right), in the field range  $\pm 5$  T. In the insets: low field regions.

### 5.7.2 BxPC3 tumor cell line

BxPC<sub>3</sub> cells were obtained from ICLC (Interlab Cell Line Collection, Genova, Italy). Cells were maintained at  $T = 37$  K in a humidified atmosphere containing 5% CO<sub>2</sub> in air as exponentially growing cultures in RPMI 1640 media (Roswell Park Memorial Institute, Sigma–Aldrich) supplemented with 10% fetal bovine serum (FBS, Sigma–Aldrich) and gentamicin (50 mg/ml) (Sigma–Aldrich).

To calculate the *generation time* ( $T_g$ ), *i.e.* the time span used by cells to divide into two daughters, it is necessary to count the number of cells in the flask every 24 hours, considering that we started from a certain inoculum measured at zero time, so that we could create the growth curve

$$N(t) = N_0 2^{t/T_g}, \quad (75)$$

where  $N(t)$  is the number of cells at time  $t$ ,  $N_0$  is the initial number at time  $t = 0$ ,  $T_g$  is the duration of the entire cell cycle (generation time), which determines the time required to double the cell population. In these conditions, the doubling time was  $T_g = 35 \pm 2$  hours.

To determine the Plating Efficiency (PE) it is necessary to calculate the ratio between  $N$ , the number of cells present in the flask at time  $t$  ( $t \sim 2$  weeks), and  $N_0$ , the number of cells from the initial inoculum ( $t = 0$ ):

$$PE = \frac{N}{N_0}. \quad (76)$$

Macroscopically, and with the aid of an optical microscope, it is possible to count surviving cell colonies. It should be remembered that clonogenic survival of one cell is defined as its capability of originating a colony con-

sisting of at least fifty individuals. In these conditions, the plating efficiency was about 50%.

### 5.7.2.1 Toxicity and cellular uptake of magnetic nanoparticles

Some preliminary evaluations were performed to determine the optimal absorption time and the concentration of MNP in the cell culture medium to be used for the treatment of hyperthermia. To assess the effect of MNPs on cell proliferation, BxPC<sub>3</sub> cells in the logarithmic growth phase were treated with MNPs at different concentrations (0, 50, 100  $\mu\text{g}/\text{ml}$ ) and with different uptake times (24 hours and for 48 hours). The results are presented in Table 4. The cells survival obtained for the samples with uptake of the nanoparticles for 24 hours and for 48 hours are almost the same. Moreover, the concentration of 50  $\mu\text{g}/\text{ml}$  seems to cause the same cytotoxicity of the concentration 100  $\mu\text{g}/\text{ml}$ .

The citotoxic effect of MNPs was also investigated for uptake values equal to 0, 10, 25, 50, 100  $\mu\text{g}/\text{ml}$  with  $t_{\text{uptake}} = 24$  hours. As can be ob-

**Table 3:** Results of experiments performed to determine the optimal concentration of MNPs in the cell culture medium. Clonogenic cell survival and its associated error ( $\sigma_{\text{survival}}$ ) quantified after 2 weeks, varying the concentration of MNPs in culture medium for  $t_{\text{uptake}} = 24$  hours.

Concentration $\mu\text{g}/\text{ml}$	Uptake hours	Survival	$\sigma_{\text{survival}}$
0	24	1.00	0.10
10	24	0.88	0.09
25	24	0.68	0.07
50	24	0.41	0.04
100	24	0.38	0.04

served in Table 3, cell survival (after 15 days from uptake process) drops as the concentration of MNPs increases, reaching approximately a plateau for  $c > 50$   $\mu\text{g}/\text{ml}$ . Indeed, the concentration of 50  $\mu\text{g}/\text{ml}$  and of 100  $\mu\text{g}/\text{ml}$  seems to cause the same cytotoxicity effects, probably due to an upper limit for the uptake due to the internal volume of the small cells. Finally, we used  $c = 50$   $\mu\text{g}/\text{ml}$  because with lower  $c$  the amount of up-taken MNPs is too low to allow a magnetic hyperthermia treatment, and for  $c > 50$   $\mu\text{g}/\text{ml}$  MFH efficacy does not increase. Tests had been performed for  $c = 10$   $\mu\text{g}/\text{ml}$  and  $c = 25$   $\mu\text{g}/\text{ml}$ , but the measured uptakes amounted to 4 pg/cell and 12 pg/cell, *i.e.* an insufficient amount for the cell to warm up. Cell toxicity

**Table 4:** Results of experiments performed to determine the optimal uptake time and the concentration of MNPs in the cell culture medium are shown.

Concentration $\mu\text{g/ml}$	Uptake hours	Survival	$\sigma_{\text{survival}}$
0	24	1.00	0.10
	48	1.00	0.10
50	24	0.42	0.04
	48	0.40	0.04
100	24	0.38	0.04
	48	0.38	0.04

was also measured by Trypan Blue assay after 48 hours (cell viability) and was around 3% for MNP-concentration of 50  $\mu\text{g/ml}$ .

It is worth noticing that the toxicity is commonly evaluated in literature with a viability assay, and not with a cell survival assay. However, from a radiobiological point of view, the latter assay gives the most interesting information, since it refers to the cell reproductive ability and not only to the cell state being either alive or dead. The evaluations of the efficacy of the hyperthermia and hadron therapy treatment that are presented in the following paragraphs were carried out using a clonogenic assay.

Moreover, to assess whether the presence of the particles affected the cell cycle, the samples were subjected to flow cytometry. Cell cycle distribution is measured after 48 h of incubation with MNPs at a concentration of 50 and 100  $\mu\text{g/ml}$ . For cytofluorimetric analysis the cell samples are treated with Ribonuclease A (100  $\mu\text{g/ml}$  – Sigma–Aldrich) for 30' at 37 °C and then stained with propidium iodide (50  $\mu\text{g/ml}$  – Sigma–Aldrich) for about 12–14 hours. The flowcytometer BD ACCURI C6 is used for the experiments and at least 20000 cells are counted at each point. The proportion of cells at different phases is gated and calculated using the ModFit Lt software.

There were no significant variations in the values of the different cell phases for all samples (see Table 5), treated with MNPs for 48 hours and not treated (control). Similar results have been found in several works, such as Ma et al. [98] and Calero et al. [99], who concluded that the incorporation of MNPs into cells does not alter the cell cycle.

### 5.7.3 Optimization of the experimental setup

The apparatus for magnetic hyperthermia experiments is the MagneTherm™ set-up by Nanotherics. This instrument allows the operator to work at 10

**Table 5:** Cell cycle analysis of BxPC<sub>3</sub> cells measured by flow cytometry after 48 h from the treatment with MNP (50 and 100  $\mu\text{g/ml}$ ).

Sample	G <sub>1</sub> Phase	S Phase	G <sub>2</sub> /M Phase	Apoptosis
Control	59.83 %	25.40 %	13.77 %	
MNPs - 50 $\mu\text{g/ml}$	57.11 %	21.54 %	13.25 %	8.0 %
MNPs - 100 $\mu\text{g/ml}$	56.9 %	21.43 %	13.13 %	8.5 %

different AMF frequencies (in the range 109–990 kHz), as it is equipped with two possible coils (9 and 17 turns, see Fig. 33) and 5 capacitors. The

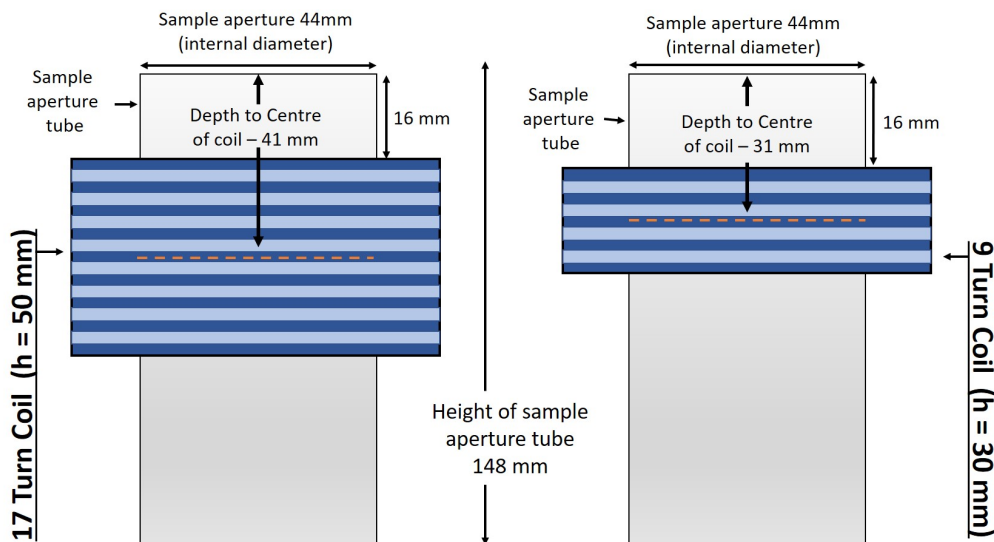


**Figure 33:** Schematization of NanoTherics MagneTherm™ setup for Magnetic Fluid Hyperthermia experiments: two coils with 17 and 9 turns (coil A and B, respectively). The homogeneity of the AMF is limited to a cylindrical region of space in the middle of the coil, with  $r \sim 8.5$  mm and  $h \sim 1$  cm for coil A, and  $r \sim 8$  mm and  $h \sim 0.5$  cm for coil B.

hyperthermic treatment used on the BxPC<sub>3</sub> cells in this project involved the application of an alternating magnetic field working at 109.8 kHz and amplitude 19.5 mT.

The typical setup involved in hyperthermic treatments is sketched in Fig. 34. An Optocon™ optical fibre thermometer was used to measure the temperature of the samples; the thermometer was placed at the centre of the sample, itself stored inside an Eppendorf PCR Tube (known as *mini-*

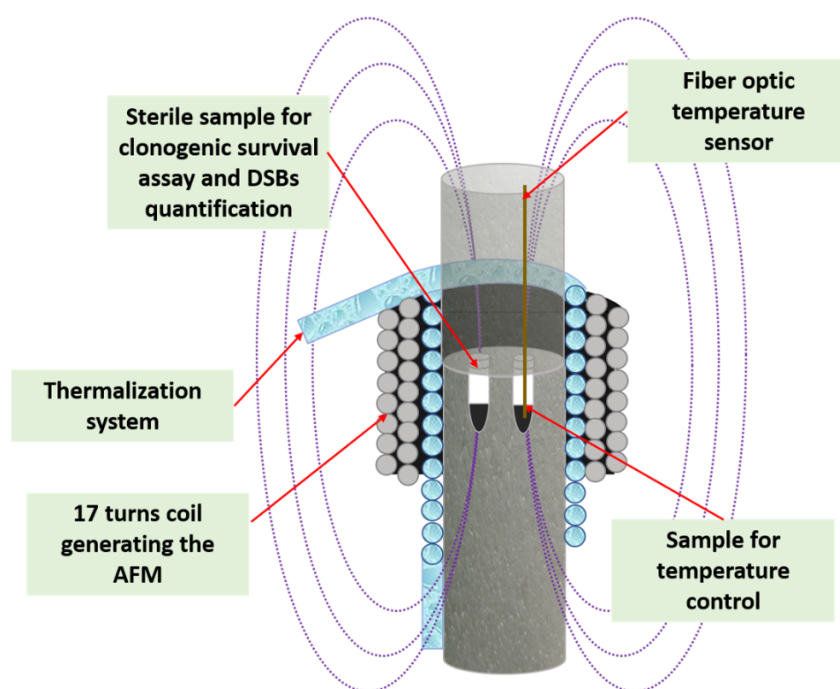


Figure 34: Representation of the hyperthermia setup. The setup consists of a heat bath, *i.e.* a thermalization system that circulates water around the two vials where the samples are stored. One of the vials is sterile, and is employed for the clonogenic survival assay and DSBs detection; the second vial is used to register the temperature by means of a optic-fiber probe.

*Eppendorf*). Two Eppendorf Tubes of volume 0.2 ml could be fitted inside the sample holder. For survival studies, the clonogenic assay must be kept sterile; hence, the temperature was detected in a *twin-sentinel* sample placed next to the actual sample used for the assay. Eppendorf tubes had to be used instead of the much bigger alternative offered by the T25 flasks that were used for the irradiation treatment. This was necessary because of the heat insulation and coil geometry, whose small inner diameter of 44 mm limited the available room. For the same reason, the pelletization process had to be done after the irradiation, to transfer the samples from the T25 flasks to the mini-Eppendorfs (as explained below). To stabilize the starting temperature of the sample to the physiological value of 37 °C, a custom thermalization system was placed inside the MagneTherm™ coil; this system is based on a Lauda Alpha A thermostat, and was inserted together with a polystyrene sample holder so that the sample could be centred in the homogeneity region of the field, to minimize the dissipation of heat.



### 5.7.3.1 Clonogenic survival evaluation

**CARBON IONS IRRADIATION EXPERIMENTS** At first, the effect of combining Hadron Therapy (HT) + Magnetic Nanoparticles (MNPs) + Hyperthermia (Hyp) was assessed by performing a clonogenic assay two weeks after the experiment. Survival data of the BxPC<sub>3</sub> cells treated with the three different modes are shown in Fig. 35, as described in Fig. 27:

- Carbon-ion (0–2 Gy) irradiation only (HT, orange circles);
- Administering of magnetic nanoparticles (uptake 48 hours) followed by carbon-ion irradiation (HT + MNP, navy blue triangles);
- Irradiation of culture cells containing MNPs by means of C ions, combined with hyperthermia treatment for 30 minutes<sup>1</sup> at 42 °C (HT + MNP + Hyp, green stars).

The results for each of the protocols were averaged over four independent measurements.

The following observations hold:

- i) at 0 Gy dose, *i.e.* unirradiated samples, clonogenic survival (CS) decreases from 1 to  $0.40 \pm 0.04$  when MNPs are added, due to a MNPs toxicity at 15 days. A further decrease of CS to  $0.24 \pm 0.02$  is observed when also Hyp is applied (mode 3, green stars);
- ii) if carbon ions irradiation alone is applied (orange circles), the CS decreases on increasing the dose, according to the law:  $CS \propto e^{-\alpha D}$ , where D stands for the dose;
- iii) once MNPs are added and irradiation is performed (mode 2 - navy blue triangles), a decrease of CS with respect to the protocol based on irradiation by itself (mode 1) is observed at all doses;
- iv) as Hyp is added further (mode 3), the CS undergoes a further decrease for all values of the dose.

These observations allow one to deduce that:

- a considerable MNPs toxicity is present; this could therefore add a potential therapeutic effect (although not synergistic);
- when compared to Hadron Therapy alone, the effect of hyperthermia on tumor cells is to yield additional killing.

<sup>1</sup> We set the overall duration for the hyperthermic treatment to 30 minutes; this value was extracted from a variety of scientific articles involving BxPC<sub>3</sub> cells [100] or different cell lines [101]. Some authors prolong the procedure up to a whole hour: we were unable to apply a similar protocol because of access limitations to hospital facilities.



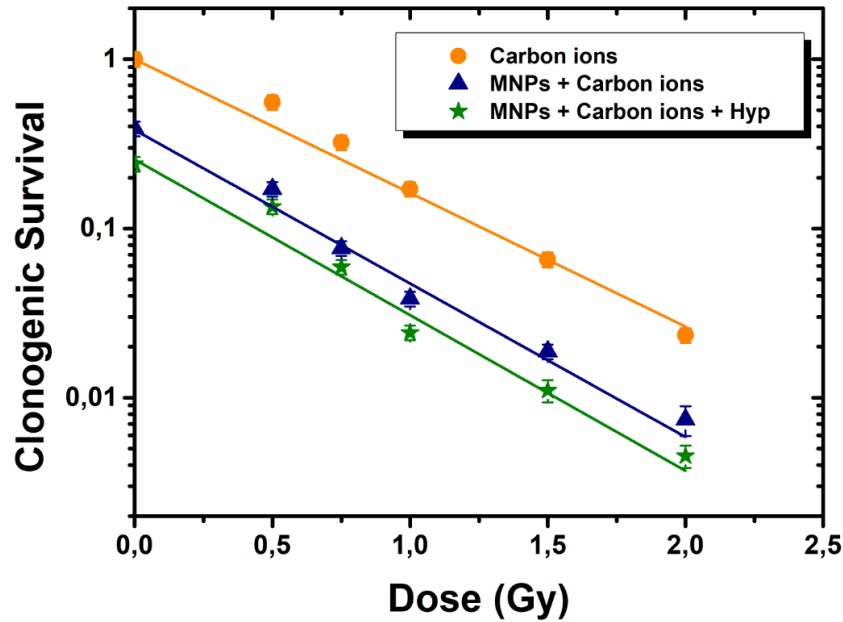


Figure 35: Clonogenic survival of BxPC<sub>3</sub> cells culture for 3 different protocols (see text): hadron therapy only (orange circles), hadron therapy + MNPs administration (navy blue triangles), hadron therapy + MNPs administration + Hyp (green stars). An additive effect of magnetic NPs administration and Hyp is distinguished. The best fit of the CS(D) curves according to the law  $CS \propto \exp(-\alpha D)$  is shown in solid lines. From the fits, one can derive the following values:  $\alpha_{\text{C-ions}} = 1.82 \pm 0.06 \text{ Gy}^{-1}$ ;  $\alpha_{\text{MNPs+C-ions}} = 2.09 \pm 0.15 \text{ Gy}^{-1}$ ;  $\alpha_{\text{MNPs+C-ions+Hyp}} = 2.11 \pm 0.20 \text{ Gy}^{-1}$ .

**PHOTONS IRRADIATION EXPERIMENTS** Experiments at a linear particle accelerator (Linac) at INT were carried out so as to compare the effect of a treatment based on hadron therapy and hyperthermia with a more conventional one consisting of photon irradiation and hyperthermia. Fig. 36 shows survival data of BxPC<sub>3</sub> cells exposed to different doses of 6 MV photons (0–7 Gy) and to Hyp at 42 °C for 30 minutes, as averaged over two independent experiments.

In a similar way to CNAO experiments, three treatment modes were used:

- photon irradiation alone (orange circles);
- photon irradiation after administering MNPs for 48 h (navy blue triangles);
- photon irradiation on cells incubating MNPs with a 30-minute hyperthermia treatment at 42 °C (green stars).

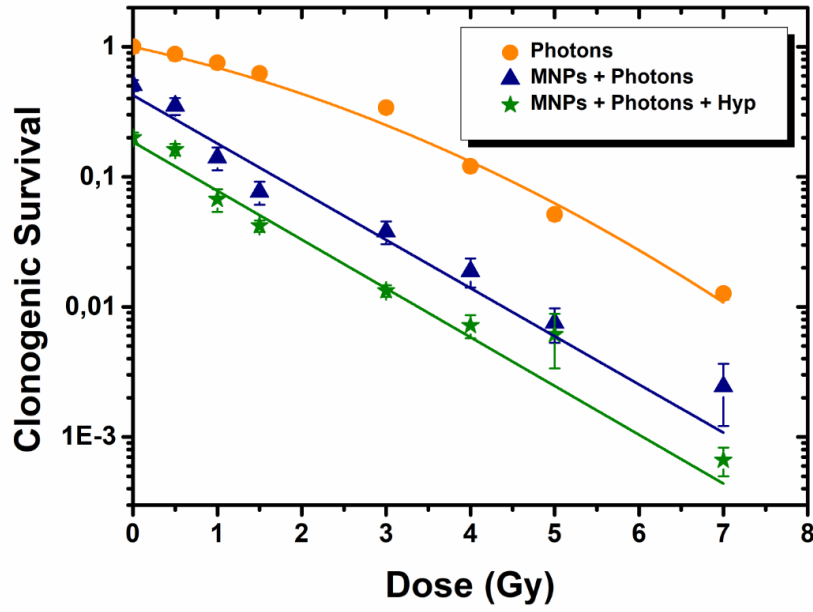


Figure 36: Clonogenic survival (CS) of BxPC<sub>3</sub> cells both incubating and non incubating MNPs, exposed to photon irradiation in the energy range 0–7 Gy, either combined or not-combined with hyperthermia. The solid lines represent the best fit for the clonogenic survival (CS) curve versus the radiation dose  $D$ . In the case of photons alone, this obeys the law  $CS \propto \exp(-\alpha D - \beta D^2)$ ; for the other two treatments, this obeys  $CS \propto \exp(-\alpha D)$ . The fits yield the following results:  $\alpha_{\text{Photons}} = 0.32 \pm 0.06 \text{ Gy}^{-1}$ ;  $\beta_{\text{Photons}} = 0.05 \pm 0.01 \text{ Gy}^{-2}$ ;  $\alpha_{\text{MNPs+Photons}} = 0.85 \pm 0.09 \text{ Gy}^{-1}$ ;  $\alpha_{\text{MNPs+Photons+Hyp}} = 0.86 \pm 0.06 \text{ Gy}^{-1}$

The following observations can be made:

- i) as in the scenario with HT only, the clonogenic survival (CS) for unirradiated samples—*i.e.* a dose equal to 0 Gy—decreases from 1 to  $0.50 \pm 0.05$  when MNPs are added; moreover, an additional CS decrease of  $0.20 \pm 0.02$  is observed when hyperthermia (Hyp) is applied as well (mode 3);
- ii) if only photon irradiation is applied, the clonogenic survival decreases as soon as the dose is incremented according to the linear quadratic model:  $CS \propto e^{-\alpha D - \beta D^2}$ ;
- iii) at all doses, the addition of the MNPs decreases the clonogenic survival as compared to irradiation with photons only, confirming the results found for hadron therapy (HT);
- iv) when the MNPs are added, the CS *vs* D model changes to  $CS \propto e^{-\alpha D}$ , which corresponds to a modification of the cells' response to pho-

ton irradiation; thus the typical shoulder of the dose-survival curves, found after treatment with radiation alone, is removed;

- v) as in HT, once Hyp is added, the CS drops further; the dose-survival curve obeys the law  $\propto e^{-\alpha D}$  in this case as well.

Therefore, also in this case we can conclude that: (i) there is a toxicity linked to MNPs, comparable to the HT case; (ii) Hyp grants an additional killing effect on tumor cells as compared to photon irradiation by itself.

**COMPARISON BETWEEN PHOTONS AND CARBON IONS** When carbon-ion-based radiotherapy is administered, the ensuing survival fractions are lower than those for the photon-irradiated samples; this had already been observed for different types of tumors [102–104] and other pancreatic tumor cell lines [105]. This observation thus strengthens the conclusion that carbon-ion radiotherapy leads to a higher efficacy with respect to standard photon-based radiotherapy.

As reported in Section 5.3.1, carbon ions and other types of high-LET particle radiation are characterized by the presence of a *Bragg Peak*, where the majority of the dose is deposited. The interesting feature of the Bragg peak is that its depth within the target tissue can be tuned at will. This high degree of customizability in the dose profile allows medical practitioners to subject the tumor to maximum doses with high accuracy, allowing for minimal adverse effects in the surrounding tissues.

For carbon-ion and photon irradiations, the  $\alpha$  values were determined and can be found in the captions of Fig. 35 and Fig. 36. As could be expected,  $\alpha$  values were significantly smaller for photons than for carbon ions; this reflects a steeper decline of the initial slope of the survival curves for high-LET beams. Remarkably, a higher relative biological effectiveness (RBE) has been proven for particle radiation, surpassing conventional photon therapy in terms of increased cytotoxic effect. Moreover, by comparing cell survival data after carbon and photon irradiations, we managed to determine the relative biological effectiveness (RBE) of carbon ions as the ratio between the reference radiation dose (6 MeV photon) and the carbon ion irradiation required to produce the same biological effect. For a clonogenic survival amounting to 10%, the relative biological effectiveness of the CNAO carbon-ion beam was about 3.5 (Fig. 37). From this finding, one can infer that the use of hadrons against pancreatic tumors could be a promising cancer therapy. Until now, the RBE values reported for C ions in the scientific literature are few, but they all seem to agree with our conclusions. As was shown by El Shafie et al. [48], the RBE of carbon-ion irradiation for a BxPC<sub>3</sub> cell line ranged from 1.5 to 3.5, depending on the dose and the survival level; around a decade ago, Oonishi et al. published data that confirmed an increased RBE of carbon ions irradiation for the same

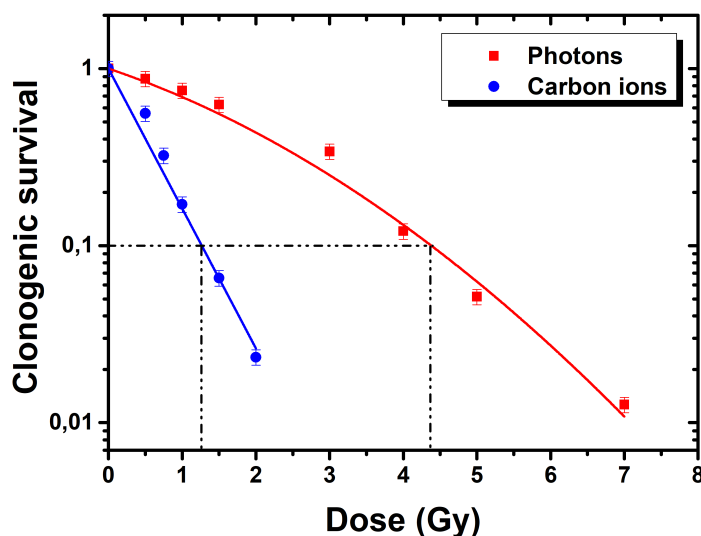


Figure 37: Evaluation of relative biological effectiveness (RBE) for carbon ions. In red, the CS versus Dose profile obtained with photon irradiation; in blue, the one for carbon ions.

cell line [106]. Remarkably, since the presence of magnetic nanoparticles causes the cell mortality rate to grow and, in the case of photons, it modifies the dose-survival response law, we guess that they have a radiosensitizing and possibly synergistic effect on BxPC<sub>3</sub> cells. Similar results were obtained with gold nanoparticles and x-rays by Li et al. [107], Liu et al. [108] and Wang et al. [109], on 4T1, EMT-6 murine breast carcinoma and HeLa cells, respectively. In a perspective, Goel et al. [110] report progress in nanoparticles-mediated radiosensitization.

### 5.7.3.2 Double Strand Breaks Evaluation

The evaluation of Double Strand Breaks, *i.e.* a break in double-stranded DNA in which both strands have been cleaved, is limited to carbon ions irradiation.

The kinetics of DNA-DSB rejoining has been evaluated by means of  $\gamma$ -H2AX and 53BP1 foci formation by immunofluorescence analysis. Both  $\gamma$ -H2AX (phosphorylation at Ser-139) and 53BP1 are signatures of DNA double-strand breaks whose role as markers has been thoroughly validated [87, 88].

The results were collected over four experiments carried out at CNAO, in Pavia. The analysis was carried out after exposing BxPC<sub>3</sub> pancreatic tumor cells to 0.75 and 1.5 Gy, and later harvested 6 and 24 hours after

the three different treatment modes. In Fig. 38 we report the normalized *foci/cell* values at different doses. The following observations hold:

- as expected, carbon-ion radiation alone (mode 1) increases the number of DSBs with respect to control, *i.e.* untreated, samples (Ctrl, Fig. 38a); this difference is more striking at 6 hours from treatment, indicating that at 24 hours cells repair is more efficient for both DSBs markers used;
- at zero dose, the hyperthermia treatment (mode 3) causes the number of double-strand breaks at 6 hours to further increase with respect to samples without hyperthermia (mode 1 and 2 treatments, Fig. 38b);
- at 0.75 Gy, hyperthermia causes the number of double-strand breaks to significantly increase after 6 hours, both for  $\gamma$ -H2AX and 53BP1 foci; on the other hand, at 1.5 Gy the differences in the number of double strand breaks between the three different treatments are minimal;
- at 24 hours, the number of double-strand breaks is lower for both doses and for all treatment modes.

These results were similar to those reported by Ma et al. [98] and suggest that the combination of magnetic nanoparticles (MNPs) + hyperthermia (Hyp) has a radiosensitisation effect that inhibits repair mechanisms of cellular DNA.

The available scientific literature supports the notion that the hyperthermic effect depends on the linear energy transfer of ionizing radiation; despite this, the potential molecular mechanism underlying hyperthermia radiosensitization to particle radiation still remains poorly known and scarcely investigated. As to low-LET radiations, a major contribution in the unravelling of such a mechanism(s) was provided by Chinese hamster ovary (CHO) cell lines that were grown with a specific defect in the two processes devoted to the repair of radiation-induced DNA double strand breaks, non homologous end joining (NHEJ) and homologous recombination (HR). In this respect, allowing CHO wild-type cells together with a panel of repair-defective counterparts to be irradiated with protons (LET = 1 keV/ $\mu$ m, 42.5 °C water bath, 1 h) and carbon ions (LET = 13–70 keV/ $\mu$ m; 42.5 °C water bath, 1 hour) led to a demonstration that HR gives a prevalent contribution over NHEJ in radiosensitization; in addition, this probably affects the processing of a subset of DNA DSBs lesions [88]. It is interesting to point out that, at the molecular level, hyperthermia ( $T > 41$  °C) was shown to inhibit HR in human and mouse cells, leaving some of the most relevant players in this process affected: *e.g.* delaying recruitment of RAD51 at foci induced by radiation, degrading BRCA2, inactivating RPA, reducing the

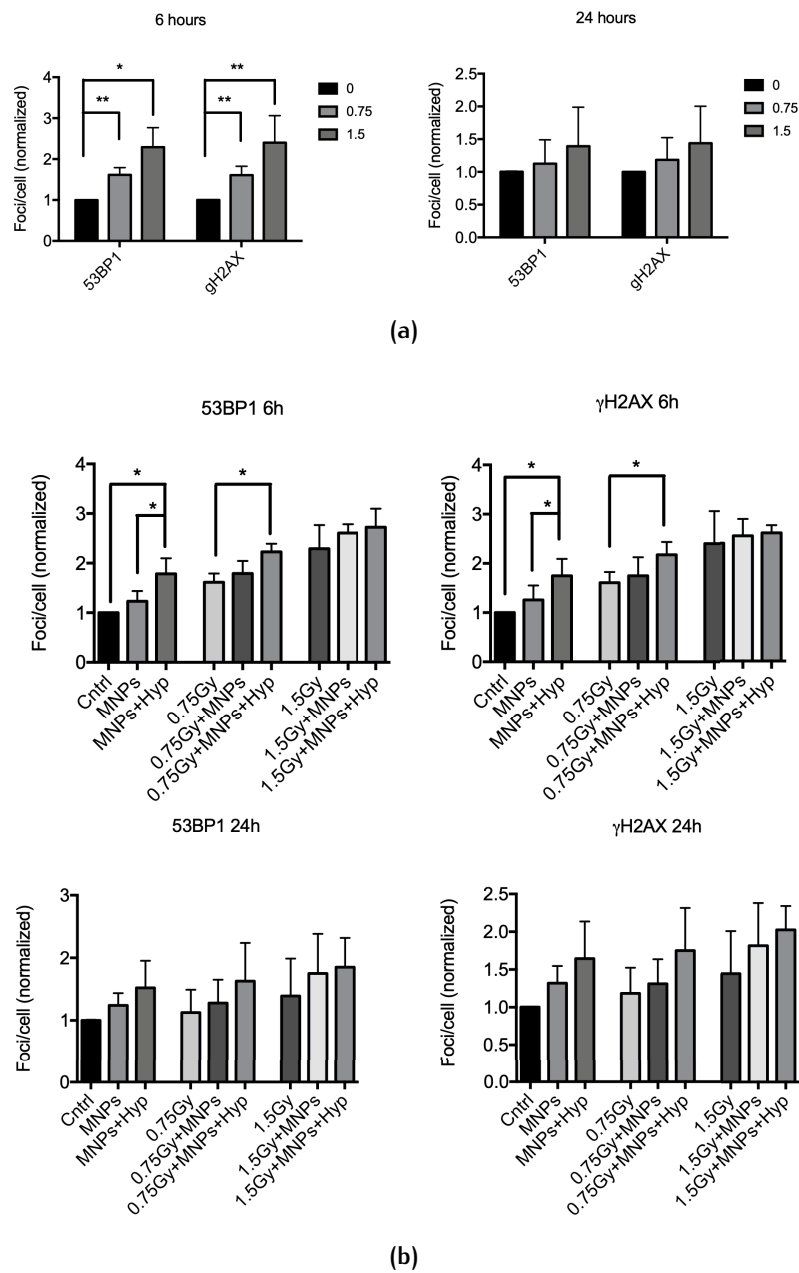


**Figure 38:** Analysis of 53BP1 and  $\gamma$ -H2AX foci induction after 6 and 24 hours from the exposure to 0.75 and 1.5 Gy of carbon-ions alone (a) and in combination with MNPs uptake and/or Hyp in BxPC3 pancreatic tumor cells (b). \* indicates  $p < 0.05$ , \*\* indicates  $p < 0.01$  (one-way ANOVA and Tukey's multiple comparison post-test).

level of the MRN complex, etc [111]. Moreover, since heat seems to be the culprit behind the pleiotropic effect on cells, it seems sensible that cytotoxic or sensitizing effects of hyperthermia cannot be attributed to the deactivation of a single DNA repair mechanism, but rather to an influence over

many pathways on multiple levels [111, 112], such as cell cycle progression and activation of checkpoints.

## 5.8 CONCLUSIONS

In this chapter, the results of the Hadromag project, funded by the Italian National Institute of Nuclear Physics, have been presented. In particular, the anti-tumor efficacy of a combination of carbon-ion therapy and hyperthermia applied to pancreatic adenocarcinoma cells BxPC<sub>3</sub> has been evaluated. A significant part of the heating power was provided through Magnetic Fluid Hyperthermia (40% of the total heating), assisted by magnetite nanoparticles with core diameter of 19 nm and coated with an organic biocompatible ligand, namely DMSA (meso 2, 3-dimercaptosuccinic acid). The hadron carbon ions therapy was shown to have RBE  $\sim 3.5$ , thus confirming a greater efficacy with respect to photons therapy. The clonogenic survival results with respect to simple irradiation of culture cells, clearly show:

- at all hadron therapy/photon irradiation doses, an additional toxicity/killing effect of about 50–60% due to the cellular uptake of the magnetic nanoparticles;
- a significant killing effect of hyperthermia for both irradiation protocols, consisting in an additional 15–30% of total clonogenic survival. In addition to this, at 6 hours after hadron-therapy irradiation with a 0.75 Gy-dose plus administration of magnetic nanoparticles and hyperthermia, the number of DNA-DSBs was observed to increase significantly as compared to the sample exposed to irradiation only.

The increased efficacy of Hadron Therapy combined with hyperthermia paves the way for future preclinical studies. Strengthened by these encouraging results, it is clear that this combination will have to be further investigated, with the goal of finally translating it into clinical applications. At the moment, the author of this thesis participates in the INFN Prothyp project, a continuation of the Hadromag project that investigates the effectiveness of the combined treatment of hyperthermia and proton radiation. The energy of the proton beam is between 131.5 MeV/u and 164.8 MeV/u, so as to obtain a SOBP of 12 to 18 cm in water (similar to that of carbon ions) and the cells are subjected to a dose between 0–6 Gy. The results are not presented in this thesis, since unfortunately, due to the health emergency created with SARS Covid-19, it was not possible to access the irradiation facilities and the laboratories, therefore, at the moment only 2 of the 4 scheduled experiments have been carried out.





# 6

---

## COATING EFFECTS IN NANOPARTICLES

---

**S**UPERPARAMAGNETIC nanoparticles attract a lot of interest in the field of applied medicine, as they can be used, among the rest, for biosensing, drug delivery, MRI contrast agents, and so forth.

The scientific community constantly endeavours to find new synthesis methods; the ultimate goal is to improve the efficiency of nanoparticles both from the point of view of their magnetic properties, and with respect to the characteristics required for an *in vivo* application. In general, stability and biocompatibility can be taken for granted, as the NPs are stabilized with polymer chains. Coating the nanoparticles also offers the possibility of functionalizing the nanoparticles. In this chapter an experimental investigation of  $^1\text{H}$  nuclear magnetic resonance relaxometry of magnetic nanoparticles is proposed, aimed at evaluating the possible effect of the coating on the relaxometric properties of NP systems.

### 6.1 RATIONALE

Imaging techniques play a pivotal role in various branches of medicine. In particular, the role of Magnetic Resonance Imaging (MRI) was paramount, as it combines a variety of assets. Among them, the use of non-ionizing radiation, the lack of any constraint on the penetration depth and the ability to acquire 3D images with a spatial resolution down to a few micrometers. The process of reconstructing MRI acquisitions mainly originates from the analysis of NMR signals due to the protons in the water molecules making up different organs/tissues/liquids, which are subjected to appropriate gradients of the magnetic field.

As explained in section 4.4, from a typical MRI experiment carried out with a classical spin-echo sequence, the collected signal is:

$$S(t) \propto \rho(^1\text{H}) e^{-\frac{TE}{T_2}} \left(1 - e^{-\frac{TR}{T_1}}\right) e^{-bD} \quad (77)$$

where  $\rho(^1\text{H})$  is the proton density,  $D$  the diffusion coefficient,  $b$  a constant,  $TE$  and  $TR$ , known respectively as *echo time* and *repetition time*, are user-defined parameters. Contrast agents (CAs)—*i.e.* biodegradable and biocompatible materials with tailor-made features in terms of geometry, magnetic properties and interactions with water—can be injected into the body so as to increase the image contrast. Indeed, the presence of CAs causes both  $T_1$  and  $T_2$ —*i.e.* the nuclear relaxation times of protons—to decrease, thus yielding a local increase ( $T_1$ -relaxing CAs) or decrease ( $T_2$ -relaxing CAs) of the NMR signal in the areas of the body where the agent is most present. The magnetic resonance image produced by these areas will then appear with unequal brightness and darkness. Contrast agents can be classified in terms of their contrast-generating mechanism of action: paramagnetic, superparamagnetic, chemical exchange saturation transfer, direct detection. Among the paramagnetic CAs—*i.e.* contrast agents that include a metal ion that has unpaired electrons—those based on Gd(III) and Mn(II) and Fe(III) complex stand out, thanks to their high magnetic susceptibility. The effect of this compound is much more pronounced on  $T_1$ . For example, it was observed that the addition of 1 mM Gd-DOTA in gray matter at 1.5 T increases  $1/T_1$  of +428% and  $1/T_2$  of +41% [113]. Superparamagnetic CAs are colloidal materials composed of particles in a suspension. The theory of nuclear relaxation in the presence of superparamagnetic nanoparticles has been presented in section 4.4. Usually superparamagnetic CAs have a very high  $r_2/r_1$  ratio and predominantly affect  $T_2$  ( $T_2$ -relaxing CAs); furthermore, they can be classified according to their size in USPIO (Ultrasmall superparamagnetic iron oxide,  $d < 50$  nm), SPIO (small superparamagnetic iron oxide  $50$  nm  $< d < 1$   $\mu\text{m}$ ) and MPIO (micron-sized particles of iron oxide,  $d > 1$   $\mu\text{m}$ ) nanoparticles. Chemical exchange saturation transfer (CEST) are molecules with exchangeable protons/water molecules that resonate at a frequency displaced by the chemical shift, different from the bulk water signal. They generate contrast in MRI images thanks to the transfer of their spin polarization to the protons of bulk water.

Finally, direct detection agents (DDAs) are  $^{13}\text{C}$ ,  $^{23}\text{Na}$ ,  $^{14}\text{N}$ ,  $^{31}\text{P}$ ,  $^{19}\text{F}$ . They can be directly detected, as they possess a nuclear magnetic moment of spin, and in general have an almost nil background, but this method unfortunately suffers from poor sensitivity. A separate discussion must be made for the  $^{19}\text{F}$ , which is a promising candidate as a DDA, given its natural abundance, its high gyromagnetic ratio (40.08 MHz/T) and sensitivity (83% of  $^1\text{H}$ ).

Superparamagnetic nanoparticles (NPs), on the contrary, essentially cause the  $T_2$  relaxation time of the solvent nuclei to decrease, and owe their properties to synthesis procedures developed only in recent times. These yield NPs with low toxicity, and grant the experimentalist ample synthesis control on the shape, the size, and the surface of the magnetic nanoparticles (MNPs). These features altogether make them very versatile from an applicative point of view [114]. The efficiency of such particles for diagnostics has indeed been proved to depend on several magnetic (nature of metal ion, spin topology, magnetic anisotropy), morphological/structural (core diameter, shape, crystallinity degree, coating thickness) and chemical (water exchange dynamics, mainly due to coating hydrophilicity, permeability and thickness) parameters [115–121]. Moreover, an extraordinary asset of MNPs is their reactive surface, as this can be exploited to anchor several molecules, with potentially different functionalities. This can be achieved in at least two ways: on the one hand, the surface of the nanoparticle can be functionalized with specific targeting agents, such as antigens and antibodies; on the other hand, they can be loaded with cargo such as radiotracers, fluorescent dyes, drugs, etc. Many research groups have investigated this possibility for the last two decades [122]. In the ideal scenario, these goal of these nanosystems would be to selectively reach the targeted organs and tissues, cause an enhancement of the image contrast in that specific area and, at the same time, release a drug or heat that region by means of MFH to induce cell death. Thus, these nanoparticles can combine properties that would be useful in diagnostics with other properties compatible with therapy, making them potential theranostic agents.

In this chapter we investigated the relaxometric, magnetic and morpho-dimensional properties of two series of water-dispersed  $\gamma$ -Fe<sub>2</sub>O<sub>3</sub> superparamagnetic nanoparticles (with mean diameters  $d_{\text{TEM}} = 17 \pm 2.5$  nm and  $d_{\text{TEM}} = 8 \pm 0.4$  nm) coated with four different kinds of biocompatible negative polyelectrolytes. The goal of the study was to investigate how the behaviour of the MNP suspensions is influenced by the different types of polymer coatings in terms of  $T_1$  and  $T_2$ , *i.e.* their <sup>1</sup>H NMR relaxation times, both longitudinal and transverse, respectively. The relaxation times were also proved to be influenced by the size of the nanoparticles' magnetic core. These conclusions were published in [123].

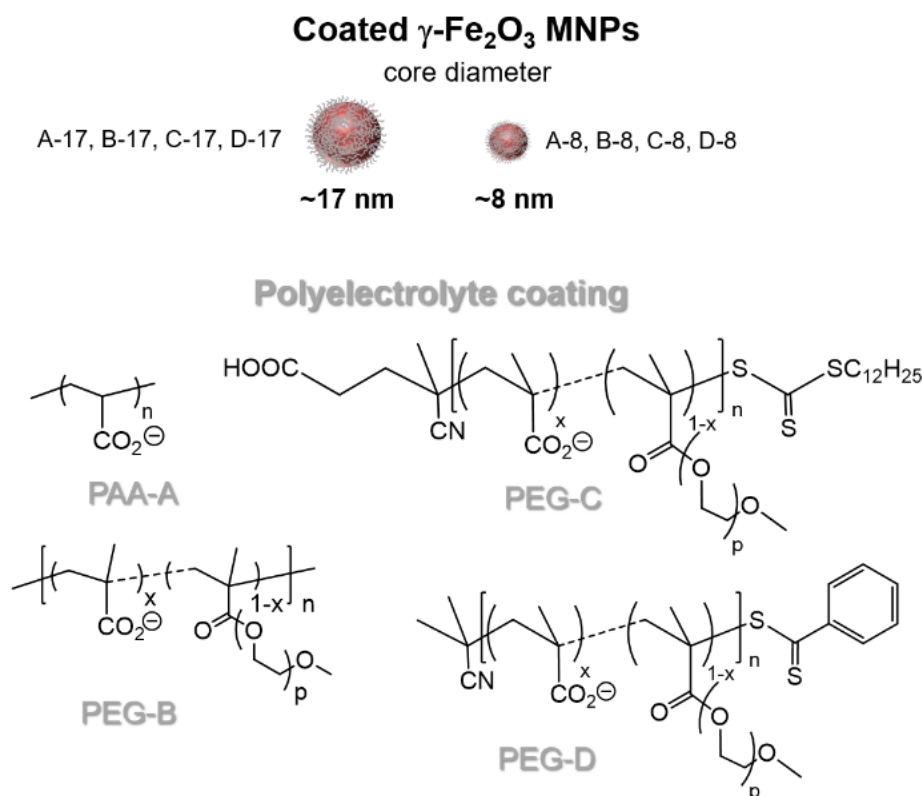


Figure 39: Structures of the investigated MNPs as a function of their core diameter and polyelectrolyte coating, depicted as PAA-A (poly(methacrylic acid)), PEG-B (PMAA-g-PEG<sub>2000</sub>), PEG-C and PEG-D (P(MAA-stat-MAPEG<sub>2000</sub>) with two different transfer agent).

## 6.2 SUPERPARAMAGNETIC NANOPARTICLES: SYNTHESIS AND CHARACTERIZATION

### 6.2.1 Fabrication Procedure of MNPs

Four different MNP polyelectrolyte coatings have been used:

- (i) Poly(acrylic acid), named PAA-A (average  $M_n = 1800 \text{ g mol}^{-1}$ ), purchased from Sigma-Aldrich (St. Louis, MO, USA) and used as received;
- (ii) A copolymer issued from the random esterification of poly(methacrylic acid) (PMAA) chains with polyethylene glycol (PEG<sub>2000</sub>), PMAA-g-PEG<sub>2000</sub>, named PEG-B ( $M_n = 5.86 \times 10^4 \text{ g mol}^{-1}$ );
- (iii)-(iv) Two types of comb-like polymers fabricated by means of reversible addition-fragmentation chain transfer (RAFT) based on PMMA and

poly(ethylene glycol) methyl ether methacrylate (MAPEG<sub>2000</sub>) with two different chain transfer agents, (PMAA-stat-MAPEG<sub>2000</sub>), named respectively PEG-C for the hydrophobic transfer agent (with  $M_n = 3.99 \times 10^4 \text{ g mol}^{-1}$ ) and PEG-D for the hydrophilic transfer agent (which has  $M_n = 2.87 \times 10^4 \text{ g mol}^{-1}$ ) [124, 125].

Low-diameter maghemite-based MNPs (samples A-8, B-8, C-8 and D-8, with PAA-A, PEG-B, PEG-C and PEG-D coatings, respectively), having average magnetic core size  $d_{\text{TEM}} \approx (8.0 \pm 0.4) \text{ nm}$ , were synthesized following Massart's protocol. This relies on the coprecipitation of iron(II) and iron(III) chloride salts in the presence of ammonium hydroxide [126]. High-diameter maghemite-based nanoparticles (samples A-17, B-17, C-17 and D-17, with PAA-A, PEG-B, PEG-C and PEG-D coatings, respectively), having average magnetic core  $d_{\text{TEM}} \approx (17.0 \pm 2.5) \text{ nm}$ , were prepared by a modified version of Massart's method [127]. The method can be briefly described as follows: iron-chloride salts were dissolved in an HCl acidic solution ( $2 \text{ mol L}^{-1}$ ) and deoxygenated. 6.6 mL of a  $\text{FeCl}_3 \cdot 6\text{H}_2\text{O}$  solution ( $1 \text{ mol L}^{-1}$ ) and 1.7 mL of a  $\text{FeCl}_2 \cdot 4\text{H}_2\text{O}$  solution ( $2 \text{ mol L}^{-1}$ ) were subsequently mixed together and heated in an argon atmosphere up to  $70^\circ\text{C}$ . After intense stirring, 64.4 mL of a  $1 \text{ mol L}^{-1}$  tetrapropylammonium hydroxide was injected at a rate of  $0.7 \text{ mL min}^{-1}$  using a syringe pump; they were later mixed for an 20 additional minutes. An acidic solution of iron nitrate was then employed to oxidize the two suspensions to maghemite, and they were later redispersed in nitric acid [126]. Magnetic decantation steps were performed successively to purify the dispersion. A narrow polydispersity was achieved by means of selective precipitation, sorting the NPs by size [128]. The different types of polyelectrolytes were selected for their biocompatibility so as to allow *in cellulo* MRI, and they were coated following a protocol already described in the scientific literature [125]. The polymer powder was then added to the acidic dispersion of maghemite magnetic nanoparticles (0.06 wt.%). For instance, for 2.5 mL of iron-oxide suspension, either 5 mg of PAA-A or 15 mg of PEG-B, PEG-C, PEG-D were added. A  $1.4 \text{ mol L}^{-1}$  solution of ammonium hydroxide was dripped and stirred in the solution to yield a pH above 8. The excess polyelectrolytes were removed by means of dialysis against Millipore water; this was carried out using a Spectra/Por<sup>TM</sup> membrane (regenerated cellulose) with an 8–10 kDa or 300 kDa cut-off over 48 h, while the solution stabilized at a pH around 7 after neutralization.

### 6.2.2 Morphological Characterization

#### TEM

The nanoparticles' morphology was investigated using TEM, *i.e.* transmis-

sion electron microscopy. A MO-Jeol 123So (80 kV) TEM equipped with a GATAN Orius 11 Megapixel Camera was used to record the images. A few drops of the nanosystem suspension were deposited onto perforated carbon-coated copper grids (300 mesh) from Agar Oxford Instruments. Taking avail of the ImageJ software, more than three hundred NPs were counted from a statistical point of view; fitting the results to a log-normal distribution allowed us to extrapolate both the average diameter and its standard deviation. The distribution follows this definition:

$$P_x(x, \mu_y, \sigma_y) = \frac{1}{x\sqrt{2\pi}\sigma_y} \exp\left[-\frac{1}{2}\left(\frac{\ln x - \mu_y}{\sigma_y}\right)^2\right] \quad (78)$$

where  $x$  maps to all the different values of the diameter,  $\sigma_y$  is the standard deviation and  $\mu_y = \ln(d_{\text{TEM}})$ , with  $d_{\text{TEM}}$  being the average diameter. For both series, the size distribution for each sample is within 16% of the average value, a large enough range to comprise the mean values of other samples within the same series.

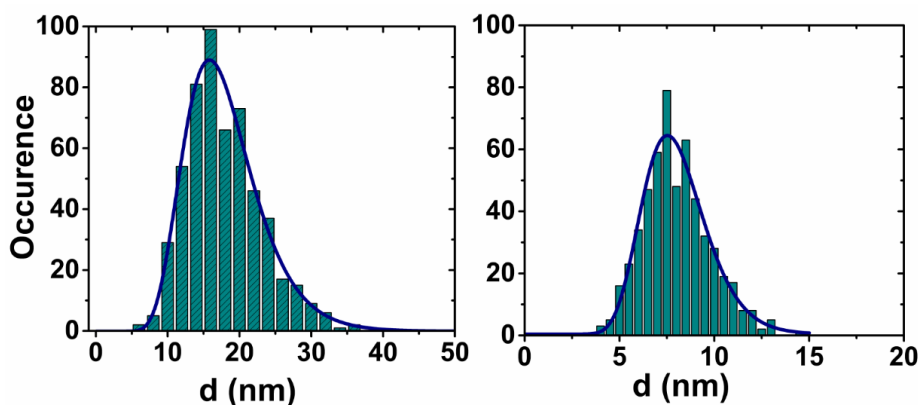


Figure 40: Core-size distribution associated to the two nanoparticle series investigated as obtained by TEM (A-8 on the right and A-17 on the left). A log-normal function was used to fit the results; the mean and the standard deviation can be found in Table 6.

### AFM and DLS

The morphology of the magnetic nanoparticles from the first series of samples, associated to a wide diameter, was also analyzed by Tapping Mode Atomic Force Microscopy (AFM). This technique enabled the evaluation of the overall size of the MNPs, *i.e.* the diameter of the magnetic core together with its coating. The measurements were carried out on a Bruker Nanoscope Multimode IIIa AFM system, using a Si rectangular cantilever (NSG01, NTMDT, length of 120  $\mu\text{m}$ , spring constant of 2.5 N/m and a resonance frequency around 130 kHz). To prepare the samples, a drop of very

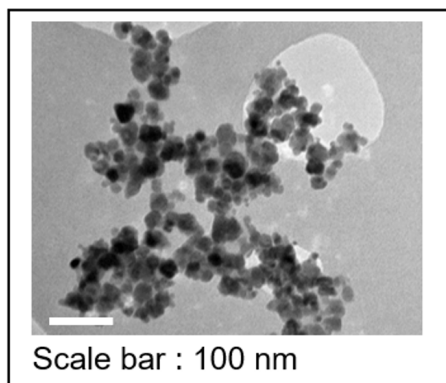


Figure (42) Representative images of sample A-17 obtained by means of bright field TEM.

Sample	$d_{\text{TEM}}$ nm
First series	$17.0 \pm 2.5$
Second series	$8.0 \pm 0.4$

Table (6) Mean diameters  $\pm$  standard deviation of the inorganic cores for the first and second series, obtained by TEM.

diluted aqueous solution of magnetic nanoparticles was allowed to dry on a mica substrate.

As expected,  $d_{\text{AFM}}$ , the average diameter of the magnetic NPs as measure by AFM, is greater than the diameter estimated from the TEM data. This can be ascribed to the presence of the polymeric coating, whose thickness, calculated as  $[(d_{\text{AFM}} - d_{\text{TEM}})/2]$ , *i.e.* by subtracting the diameters obtained through the two different techniques, is in the order of 1 to 1.5 nm, depending on the sample. The hydrodynamic diameters of the magnetic NPs have been estimated by means of a Zetasizer Nano ZS ZEN 3600 (Malvern Instruments, Worcestershire, UK), at  $T = 25^\circ\text{C}$ , and were averaged over three different acquisitions; in addition, a Cumulant algorithm was applied to fit correlograms. The results derived from a lognormal fitting of a histogram of the mean volume. The same instrument allowed to determine the electrophoretic mobility of the nanoparticles, and the zeta-potential,  $\zeta$ , was derived using Smoluchowski's approximation. The measurements were acquired over three experiments at  $25^\circ\text{C}$  in disposable folded-capillary cells. The presence of acrylate units on the four polyelectrolytes caused all of the samples to exhibit a negative zeta-potential. In particular, the zeta-potential ranges from  $-28$  to  $-48$  mV, which indicates a good colloidal stability. Furthermore, the hydrodynamic diameters of the magnetic nanoparticles from the first series (core of 17 nm) were shown to vary but slightly with the nature of the stabilizing polyelectrolyte, and they kept within a range of 71 to 85 nm. The increase in the diameter is compatible with the presence of the polyelectrolyte and a solvation layer on the surface of the NPs, especially when compared with the one measured via the TEM experiment. Similarly, the 8-nm nanoparticles samples stabilized by the PAA have an hydrodynamic diameter bigger than the one estimated by TEM, *i.e.* 21 nm;

this results is coherent with the presence of both the polyelectrolyte and the solvation layer as well.

### 6.2.3 Magnetic Characterization

The DC magnetic measurements were performed by means of a vibrating-sample magnetometer (PPMS Quantum Design Ltd., San Diego, CA, USA) and a Superconducting Quantum Interference Device magnetometer (MPMS by Quantum Design Ltd., San Diego, CA, USA) working in the 2–300 K temperature range and  $-5 \leq \mu_0 H \leq +5$  T magnetic field range. To acquire the Zero Field Cooled (ZFC) and Field Cooled (FC) magnetizations, the sample was placed in a 5 mT probe magnetic field after cooling it with and without applying the field. The magnetic material content inside the samples could not be estimated with accuracy because of the small quantity of synthesized products. This inaccuracy, together with the large experimental error in the sample weight, granted us just a rough estimate of the saturation magnetization.

The ZFC and FC magnetization curves for samples A-17 and A-8 are reported in Fig. 42; these were measured in powder form. The temperature corresponding to the maximum in the ZFC curve, commonly identified as the blocking temperature of the system, is  $T_B \approx 45$  K for the smaller-diameter magnetic NPs. For the magnetic NPs with the larger diameter, the maximum broadens towards the end of the temperature range, *i.e.* for  $T_B > 260$ –300 K; this seems to corroborate the fact that this sample series is in a sort of transition between “blocked/unblocked” (superparamagnetic) regimes at room temperature.  $T_B$  is proportional to the competing interplay between the magnetization reversal process and the magnetic energy barrier ( $E_a \approx K_{\text{eff}}V$ , see section 2.5); the former, in turn, increases with the volume ( $V$ ) of the MNPs and the effective anisotropy constant ( $K_{\text{eff}}$ ). The striking differences in the  $T_B$  temperature values associated to the two series may be due to this dependence, and to the broader volume distribution of first series. The magnetization curves acquired at low (2.5 K) and high (300 K) temperatures are shown in Fig. 43 for the 17 nm series.

To better compare their shape features, the curves are normalized to the corresponding value of the saturation magnetization ( $M_s$ ). Samples of the 17-nm series present a similar coercivity ( $\mu_0 H_C = 35$  mT) at a low temperature, a similar magnetic remanence,  $M_R/M_s = 0.3$  at 2.5 K, and a similar susceptibility,  $\chi$ , at 300 K, with the exception of D-17, which has slightly higher  $\chi$  and  $M_R$  values. Conversely, a different approach to saturation in the high-field region is observed among the samples, especially for low temperatures; sorting them from slowest to fastest in terms of saturation velocity yields the following sequence: C-17, B-17, A-17 and D-17.



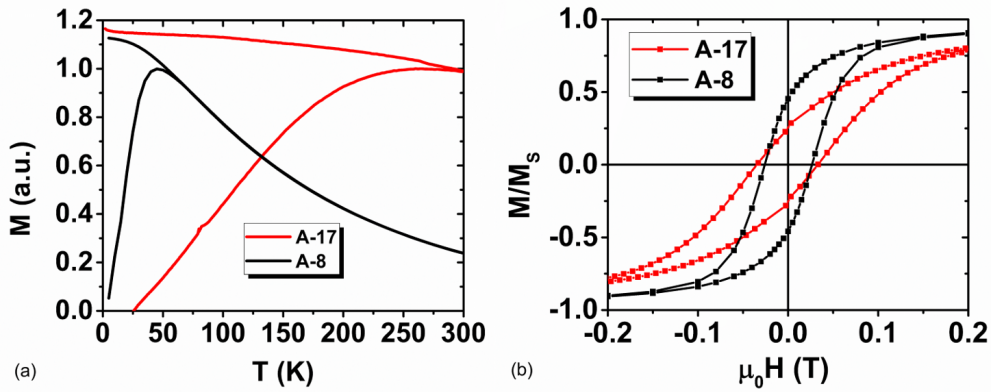


Figure 42: a) ZFC/FC magnetization curves collected with a magnetic field  $\mu_0 H = 5 \cdot 10^{-3}$  T and (b) low field hysteresis loops at 2.5 K for A-17 and A-8.

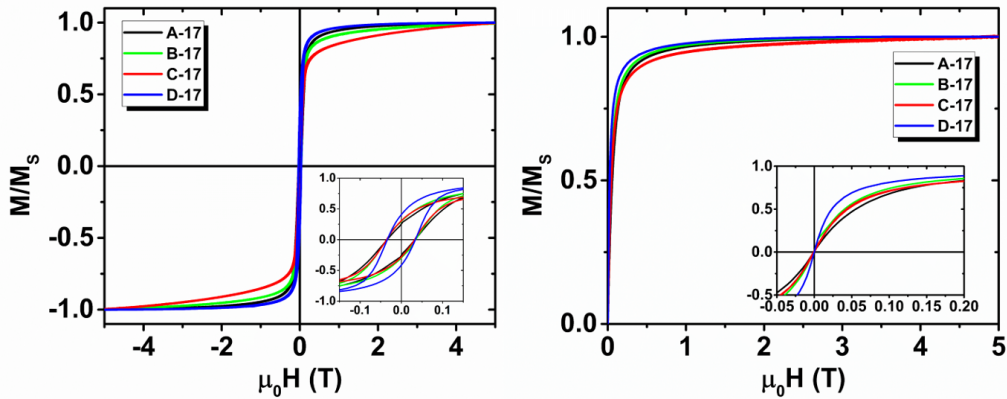


Figure 43: Magnetization curves at 2.5 K (left panel) and 300 K (right panel) for the first series. Details at low magnetic fields are shown in the insets.

### 6.3 $^1\text{H}$ NMR RELAXATION

The NMR-dispersion profiles were collected at room temperature by measuring the  $T_1$  and  $T_2$  relaxation times, varying the Larmor frequency of the investigated nuclei from 10 kHz up to 60 MHz. For low-frequency relaxation measurements (from 0.01 MHz to 7.2 MHz), a Smartracer Stellar NMR relaxometer was used to apply the Fast-Field-Cycling technique. Likewise, a Stellar Spinmaster Fourier transform nuclear magnetic resonance spectrometer was employed for high-frequency relaxation measurements (up to 60 MHz). For  $\nu_L < 7.2$  MHz, pre-polarized Saturation Recovery (for  $T_1$ ) and spin-echo (for  $T_2$ ) sequences were adopted. For frequencies  $\nu_L > 7.2$  MHz, non-pre-polarized Saturation Recovery (SR) and Carr Purcell Meiboom Gill (CPMG) pulse sequences were used for the  $T_1$  and  $T_2$  measurements, respectively.

### 6.3.1 Fast-Field-Cycling technique

The SMARTracer has a small, highly homogeneous electromagnet that enables rapid magnetic field switches, which are necessary for FFC. This Fast-Field-Cycling technique works by applying to the sample different fields consecutively, switching from one to another in a short time (2–3 ms), by modulating the current that circulates into the coil that generates the field itself. Three fields are utilized for the measurements: a *polarization field*  $B_{POL}$ , a *relaxation field*  $B_{RLX}$  and an *acquisition field*  $B_{ACQ}$  ( $B_{RLX} < B_{ACQ} < B_{POL}$ ). In FFC measurements, a lower limit of the measurable relaxation times need to be taken into account, since it is impossible to measure relaxation times faster than the dead time of the apparatus (approximately pre-polarized SE sequence allows to measure  $8 < T_2 < 100$  ms). In details,

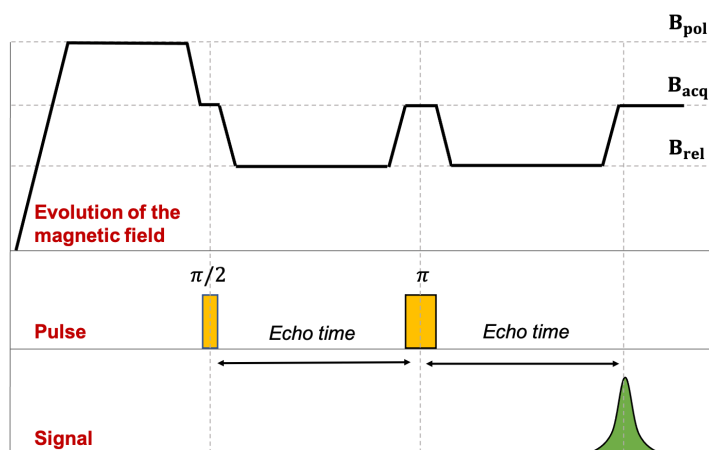


Figure 44: Pre-polarized Spin Echo sequence for low field  $T_2$  measurements with Fast-Field Cycling technique.

the strong *polarization field*  $B_{POL}$ , amounting to about 8 mT for the *Stelar SMARTracer* relaxometer used for the measurements of this Chapter, is applied first to pre-polarize the sample along the direction of the field, in order to measure a stronger signal.  $B_{POL}$  is applied for a time  $T_{POL} \simeq 4T_1$ , thus the magnetization of the sample increases up to saturation. However, for sufficiently high  $B_{RLX}$  it is recommended to use the non-pre-polarized sequence, since in a pre-polarized acquisition the signal is collected by observing the evolution of the magnetization between  $B_{POL}$  and  $B_{RLX}$ . In fact,  $B_{RLX}$  is the field where the measurement of the relaxation time is performed ( $\omega_L = \gamma_1 B_{RLX}$ ). The field value is then set to  $B_{ACQ}$ , allowing to obtain a measurable FID signal.

### 6.3.2 Longitudinal relaxation time $T_1$ measurements

The Bloch equation allows one to track the evolution of the longitudinal component  $M_z$  of the magnetization after the application of an RF pulse. As was seen in section 4.2, this can be described as

$$M_z(t) = M_{z,0} \left(1 - e^{-\frac{t}{T_1}}\right). \quad (79)$$

On a nuclear spin system with magnetization oriented along the  $\hat{z}$  direction of the static magnetic field  $H_0$ , the *Saturation Recovery* sequence consists in the successive application of two  $\pi/2$  pulses (Fig. 45), in order to bring the magnetization into the plane with the first pulse of excitation and to measure how much magnetization has been recovered along  $\hat{z}$  in the time  $t$  that separates the two pulses with the second pulse, called *reading*. The

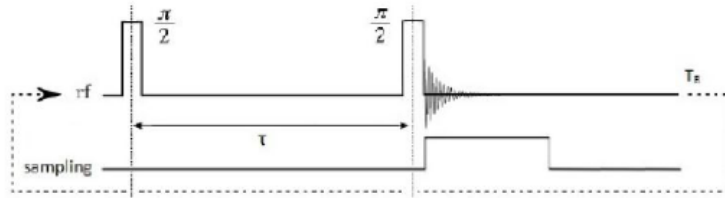


Figure 45: Saturation Recovery sequence for  $T_1$  measurements.

time  $T_1$  can be determined by varying the delay  $t$  between the two pulses and inverting Eq. (79).

### 6.3.3 Transverse relaxation time $T_2$ measurements

The  $T_2$  time, either *spin-spin* or *transverse relaxation* time, describes the decay of the magnetization in the plane due to the presence of magnetic field inhomogeneities that alter the precession speed of the single nuclear magnetic moments, moving away from the Larmor one. These inhomogeneities are due to the fact that each nucleus, in addition to the presence of the external field  $H_0$ , is influenced by the presence of the magnetic moments of the neighbouring nuclei. The spin system thus precesses with speeds distributed approximately symmetrically around the Larmor frequency  $\omega_0$ . In the reference frame rotating at  $\omega_0$ , therefore, some spins will precess clockwise and others counterclockwise, depending on whether their precession speed is lower or higher than  $\omega_0$ . This phase shift causes the magnetization  $M_{x,y}$  to decay with time  $T_2$ :

$$M_{x,y}(t) = M_{x,y,0} e^{-\frac{t}{T_2}}. \quad (80)$$

The dephasing effect of the transverse components is enhanced if the external magnetic field  $H_0$  is not homogeneous on the whole volume where the sample is located. In the latter case, if  $T_2'$  is used to quantify the contribution to the spin dephasing due to field inhomogeneities, after having perturbed the system, the transverse magnetisation  $M_{x,y}$  decays with the  $T_2^*$  time constant:

$$\frac{1}{T_2^*} = \frac{1}{T_2} + \frac{1}{T_2'} \quad (81)$$

To cancel the effect of the inhomogeneity of  $H_0$  and isolate the relaxation of  $M_{x,y}$  due to the spin-spin interaction alone, the so-called *Spin Echo* (SE) sequence developed by Hahn is used. This sequence includes a first  $\pi/2$  pulse, followed by a  $\pi$  pulse after a time interval  $\tau_{\text{echo}}$ . The second pulse has a refocusing effect and at time  $2\tau_{\text{echo}}$  it is possible to observe the signal. The echo signal turns out to be

$$M_{x,y}(2\tau_{\text{echo}}) = M_{xy,0} e^{-\frac{2\tau_{\text{echo}}}{T_2}} \quad (82)$$

The Eq. (82) above is valid only if the spins remain fixed in their positions during the echo time. In case of diffusion within the sample volume, they experience different inhomogeneities of the static magnetic field. This causes a partial recovery of the phase shift with consequent loss of signal. This effect is particularly evident in liquids for relatively large values of  $2\tau_{\text{echo}}$ . In fact, it can be shown that, taking into account diffusion, the  $M_{x,y}$  measured with an SE sequence results in:

$$M_{x,y}(2\tau_{\text{echo}}) = M_{xy,0} e^{-\frac{2\tau_{\text{echo}}}{T_2}} e^{-\gamma_I^2 G^2 D \frac{(2\tau_{\text{echo}})^3}{3}}, \quad (83)$$

where  $D$  is the diffusion coefficient of the sample and  $G$  is a magnetic field gradient that models the presence of inhomogeneities. To limit the effect of diffusion in the measurement of  $T_2$ , the *Carr-Purcell-Meiboom-Gill* sequence (CPMG) is used. Unlike the SE, after the refocusing pulse, this sequence involves sending a train of  $n$   $\pi$  pulses always along the same axis each separated from the preceding with  $2\tau_{\text{echo}}$ . It follows that for  $t = 2n\tau_{\text{echo}}$  an echo is generated. Therefore, without changing the value of echo time, the relaxation of the  $M_{x,y}$  is reconstructed by using a single sequence:

$$M_{x,y}(t) = M_{xy,0} e^{-\frac{t}{T_2}} e^{-\gamma_I^2 G^2 D (2\tau_{\text{echo}})^2 \frac{t}{12n^2}}, \quad (84)$$

where  $n$  is the number of refocusing  $\pi$  pulses. CPMG sequences were used in this measurements to estimate the  $T_2$  relaxation times of MNPs.

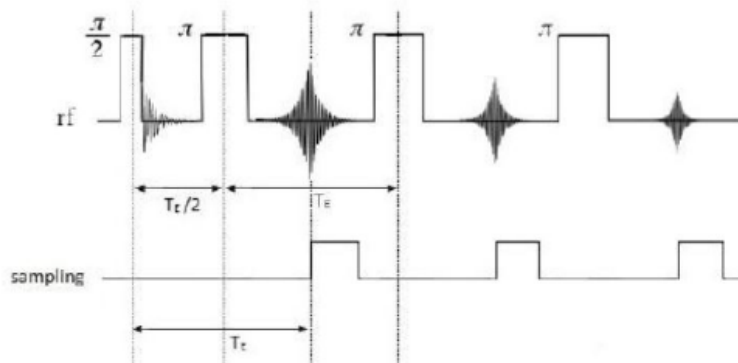
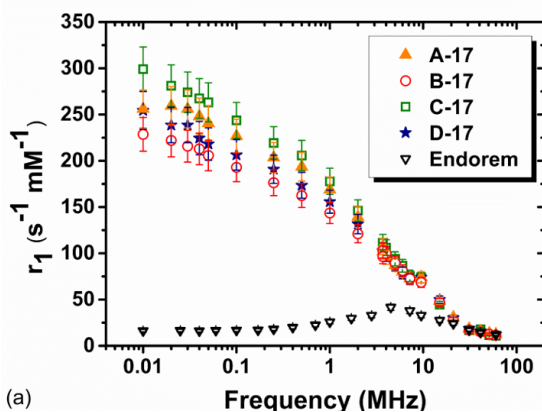


**Figure 46:** Carr-Purcell-Meiboom-Gill sequence for  $T_2$  measurements. This sequence includes a first  $\pi/2$  pulse, followed by a train of  $\pi$  pulses. The signal follows an exponential decay law with a typical time  $T_2$  - see Eq. (81).

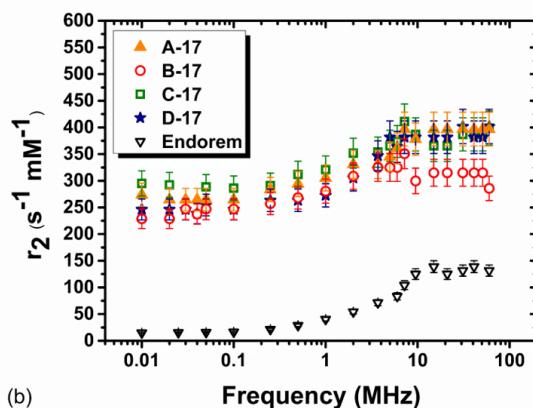
#### 6.3.4 NMRD profiles

**17-NM SERIES** In Fig. 47, the longitudinal relaxivity profile, *i.e.*  $r_1$ , as measured on the 17 nm MNP series is shown. All the samples feature a continuous increase of the longitudinal relaxivity as the Larmor frequencies decrease; moreover, no maximum is detected experimentally. A qualitative explanation for this behaviour can be offered by taking into account the energy associated to the internal magnetic anisotropy of the crystal at a low frequency. The lack of a maximum is common for spherical particles based on maghemite with diameters  $d_{\text{TEM}}$  greater than approximately 15 nm. However, in our case the flattening of the  $r_1(\nu)$  curves at a low frequency is not observed, despite this being expected for systems with high anisotropy (*i.e.* when the anisotropy energy is large enough to prevent any precession of the magnetic moment of super-paramagnetic crystals [129]).

The overall of the transverse relaxivity versus frequency curve (Fig. 47) is similar across all samples. At high magnetic fields,  $\mu_0 H \simeq 1.41$  T (and thus close to the clinical one),  $r_2 \simeq 285 \text{ mM}^{-1} \text{ s}^{-1}$  for sample B-17, whereas for samples A-17, C-17, and D-17,  $r_2 \simeq 400 \text{ mM}^{-1} \text{ s}^{-1}$ . For Larmor frequencies above the threshold  $\nu_L > 5\text{--}10$  MHz, sample B-17 features values of  $r_2$  smaller than in the other samples, slightly reflecting discrepancies in  $r_1$  as well. A lower magnetization value in the case of sample B-17 could possibly be caused by the spin disorder induced by the different polymer, or due to agglomeration effects. Table 7 provides a summary of  $r_1$ ,  $r_2$  and  $r_2/r_1$  values at 60 MHz and 15 MHz. The values are compared to those obtained using Endorem, a commercial  $T_2$  contrast agent that still provides a good reference for assessing the relaxation efficiency of relaxing  $T_2$  superparam-



(a)



(b)

Figure 47: NMRD profiles collected at room temperature for the first series (17 nm) of polymer-coated MNPs, with the Larmor frequency ranging between  $0.01 \leq \nu_L \leq 60$  MHz: longitudinal  $r_1$  (a) and transverse  $r_2$  (b). As a reference, the relaxivity values of Endorem reported by Basini et al. are shown [116].

agnetic nanoparticles, in spite of being discontinued from 2012. The  $r_2/r_1$  value is above 2, which indicates that all the ferrofluids act as negative contrast agents. This value is the conventional threshold which allows one to distinguish  $T_1$ - and  $T_2$ -relaxing agents [130].

**8-NM SERIES** The relaxivity profiles of the 8 nm series of MNPs are presented in Fig. 48. The longitudinal relaxivity  $r_1$  of this series of MNPs behaves as expected for ultrasmall superparamagnetic particles. The maximum of the longitudinal relaxivity occurs in the range 1–20 MHz, and undergoes a slight decrease by a factor of  $\simeq 4$  at 60 MHz. The maximum associated to sample A-8 is shifted towards higher frequencies, which would suggest a slightly smaller size. At low field, a slight dispersion around 300–400 kHz can be seen across all samples. This indicated that their magnetization is not completely locked along the magnetic *easy axis*, at least

**Table 7:** Longitudinal  $r_1$  and transverse  $r_2$  relaxivity values at 15 and 60 MHz, for the 1st series (diameter = 17 nm) of MNPs aqueous dispersions at room temperature. For comparison,  $r_1$  and  $r_2$  values of Endorem and the ratio  $r_2/r_1$  are reported.

Sample	Frequency MHz	$r_1$ $\text{mM}^{-1}\text{s}^{-1}$	$r_2$ $\text{mM}^{-1}\text{s}^{-1}$	$r_2/r_1$
A-17	60	12.4 (1.0)	396.8 (31.7)	32.0
	15	48.4 (3.9)	396.8 (31.7)	8.2
B-17	60	11.3 (0.9)	285.7 (22.8)	25.3
	15	47.1 (3.8)	314.9 (25.2)	6.7
C-17	60	10.9 (0.9)	398.7 (31.9)	36.6
	15	44.5 (3.6)	365.5 (29.2)	8.2
D-17	60	12.6 (1.0)	401.8 (32.1)	31.9
	15	49.9 (4.0)	381.7 (30.5)	7.6
Endorem	60	12.3 (1.0)	131.6 (10.5)	10.7
	15	27.5 (2.2)	138.9 (11.1)	5.0

at room temperature. In Table 8, a comparison between the relaxivities of  $\gamma\text{-Fe}_2\text{O}_3$  nanoparticles and those obtained with Endorem is presented.

For all samples, the  $r_2$  vs frequency behavior (Fig. 48) is similar, and at a high magnetic field  $\mu_0H \simeq 1.41\text{ T}$ ,  $r_2$  reaches the value  $\simeq 125\text{ mM}^{-1}\text{s}^{-1}$ . Thus, at the typical clinical frequency of  $\simeq 60\text{ MHz}$ , the transverse relaxometric performance of these samples is comparable to that obtained with Endorem. In addition, the  $r_2$  relaxation profile against frequency is not far from that of the CA Endorem, although the commercial compound features lower values for  $\nu < 7\text{ MHz}$ . Interestingly, the  $r_2/r_1$  ratio at  $\nu_L = 60\text{ MHz}$  reaches a value of  $\simeq 8$  for our MNPs and  $\simeq 11$  for the commercial compound. The  $r_2/r_1$  values at 60 and 15.1 MHz are close to those obtained with Endorem; this suggests that the two substances feature very similar efficiencies as  $T_2$  CAs.

**ANALYSIS OF NMRD PROFILES** The heuristic model due to Roch *et al.* was used in order to analyze the NMR longitudinal relaxivity profiles—*i.e.*  $r_1$  versus frequency—at room temperature. For reference, see Eq. (69) in section 4.5.0.3. In principle, this model would be valid for an ensemble of single nanoparticles, but we could use it thanks to the values of  $r_1$  and  $r_2$  coinciding for each sample at low frequencies, approximately  $\nu < 0.1\text{ MHz}$ , as ensured by the absence of particle aggregation at the dilution level used for the NMR experiments.



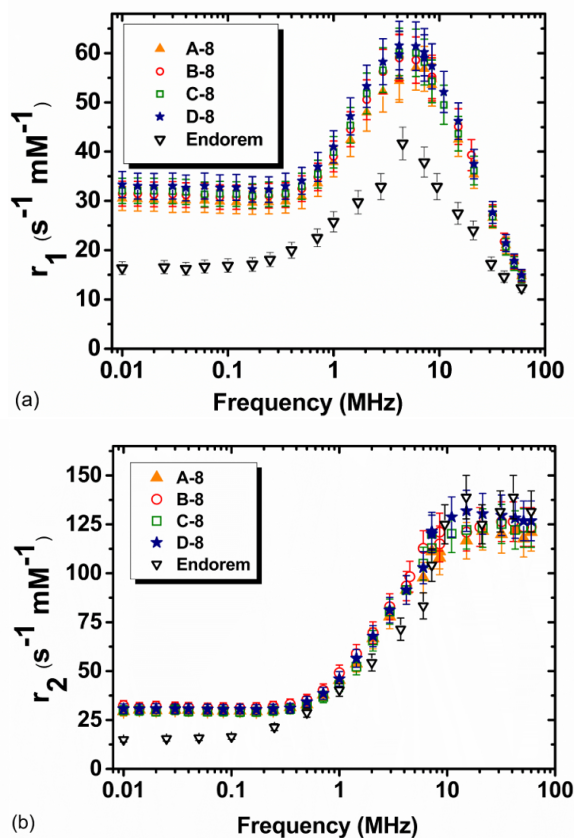


Figure 48: NMRD profiles collected at room temperature for the second series (8 nm) of polymer-coated MNPs, with the Larmor frequency ranging between  $0.01 \leq \nu_L \leq 60$  MHz: longitudinal  $r_1$  (a) and transverse  $r_2$  (b). As a reference, the relaxivity values of Endorem reported by Basini et al. are shown [116].

For this model to be valid, the nanoparticles should have a mean diameter below 20 nm. Probably, for this reason, the experimental data associated to the 17 nm samples could not be fitted, possibly since their size was close to the limit of validity of Roch's model. Moreover, the broad size distribution for all samples (see Fig. 40) made the whole fitting process rather difficult. Another demonstration that Roch's model does not apply to this series of magnetic nanoparticles lies in the fact that it did not predict any increase in the longitudinal relaxivity profile  $r_1$  for the lowest frequencies, as shown in the experimental results. On the contrary, for the second series of samples, corresponding to smaller magnetic nanoparticles, we managed to fit the experimental  $r_1$  values. The curves obtained from the Roch's model to fit the  $r_1$  profiles for specimens A-8, B-8, C-8, and D-8 are reported in Fig. 49. Among the physically relevant figures, at least the following four can be mentioned: the magnetic core radius  $r$ ; the saturation magnetiza-



**Table 8:** Longitudinal  $r_1$  and transverse  $r_2$  relaxivity values at 15 and 60 MHz, for the 2nd series (diameter= 8 nm) of MNPs aqueous dispersions at room temperature. For comparison,  $r_1$  and  $r_2$  values of Endorem and the ratio  $r_2/r_1$  are reported.

Sample	Frequency MHz	$r_1$ $\text{mM}^{-1}\text{s}^{-1}$	$r_2$ $\text{mM}^{-1}\text{s}^{-1}$	$r_2/r_1$
A-8	60	14.7 (1.2)	121.0 (9.7)	8.2
	15	42.5 (3.4)	116.7 (9.3)	2.7
B-8	60	14.7 (1.2)	123.7 (9.9)	8.4
	15	45.1 (3.6)	121.1 (9.7)	2.7
C-8	60	14.5 (1.2)	123.1 (9.9)	8.5
	15	43.6 (3.5)	122.1 (9.8)	2.8
D-8	60	14.9 (1.2)	126.7 (10.1)	8.5
	15	46.2 (3.7)	131.9 (10.6)	2.9
Endorem	60	12.3 (1.0)	131.6 (10.5)	10.7
	15	27.5 (2.2)	138.9 (11.1)	5.0

tion  $M_s$ ; the minimum-approach distance  $R$ , *i.e.* the distance between the nanoparticle's magnetic center and the protons from bulk water; the Néel relaxation time  $\tau_N$ . All these figures can be obtained from the experimental results shown in Fig. 49 fitted according to Eq. (69). The saturation magnetization parameter  $M_s$  in the fitting procedure can vary in the range 60-70  $\text{Am}^2/\text{kg}_{\gamma\text{-Fe}_2\text{O}_3}$ ; these values could be expected from literature data corresponding to particles with comparable sizes, and was substantially confirmed by the magnetic measurements on our samples. For the particle radius, by considering the size distribution width, we fixed an upper limit of  $r \approx 5\text{nm}$ . For the water diffusion coefficient, we used the theoretical value  $D = 2.3 \cdot 10^{-9}\text{m}^2\text{s}^{-1}$  at 293 K.

## 6.4 CONCLUSIONS

The dependence of the MRI contrast efficiency (*i.e.* the nuclear relaxivities) on the organic coating of maghemite-based MNPs was investigated by means of nuclear magnetic resonance relaxometry. In details, MNPs dispersed in water with two different diameters ( $d_{\text{TEM}} \approx 8 \pm 0.4\text{ nm}$  and  $\approx 17 \pm 2.5\text{ nm}$ ) and four different coatings, *i.e.* PAA, PMAA-g-PEG and two P(MAA-stat-MAPEG) with different transfer agents were employed. A

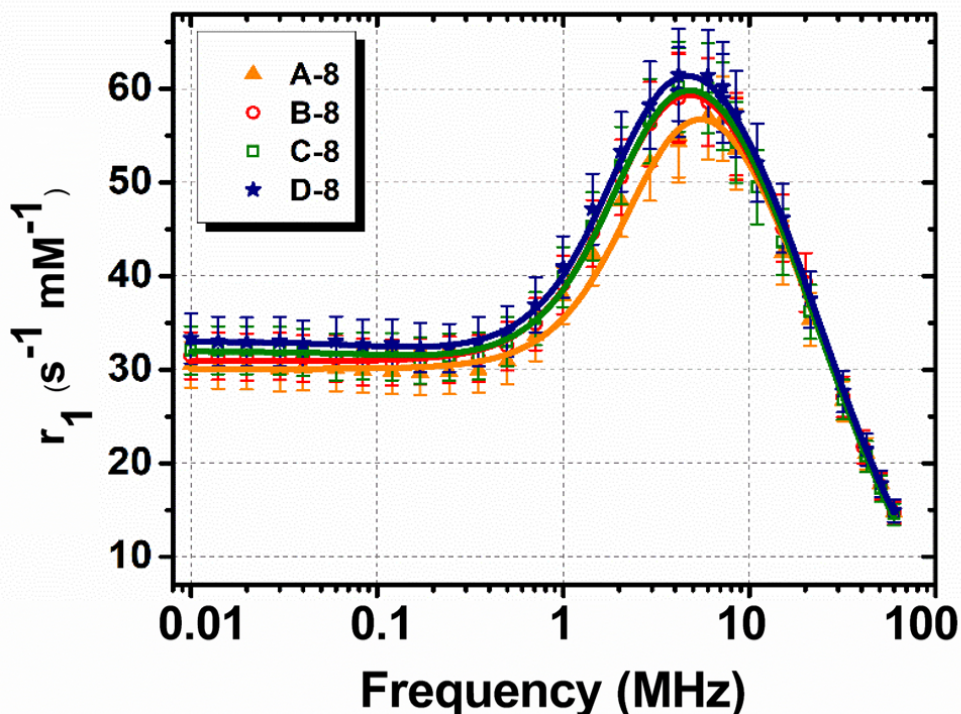


Figure 49: Room-temperature NMRD longitudinal  $r_1$  profiles for the 8 nm series of polymer-coated MNPs; different samples are shown as different symbols. The Larmor frequencies vary in the range  $0.01 \leq \nu_L \leq 60$  MHz. The best fits given by the application of Roch's model are shown as solid-line curves.

structural, morpho-dimensional and magnetic characterization of the nanoparticles was carried out by means of TEM, AFM and DC magnetometry experiments. The magnetization curves, especially those at low temperatures, displayed a different approach to saturation as the coating was varied, with the the sample coated with hydrophobic P(MAA-stat-MAPEG) having the slowest  $M_s$  approaching rate, followed by that coated with PMAA-g-PEG. This evidence suggests that the hydrophobic P(MAA-stat-MAPEG) and PMAA-g-PEG coatings favor higher spin disorder at the particle surface.

Samples having the same core size but different coatings have the same  $r_1$ -NMRD profile; this indicates that the coating type used in this work does not influence the longitudinal relaxometric properties in an evident manner. For transverse relaxivities, we observed a similar trend, except for the PMAA-g-PEG-coated sample from the 17 nm series, which had a lower  $r_2$ , especially for  $\nu_L > 5$ –10 MHz. Moreover, all investigated samples showed high  $r_2$  values at 60 MHz ( $\approx 120 \text{ mM}^{-1}\text{s}^{-1}$  for  $d_{\text{TEM}} \approx 8$  nm and

300–400 mM<sup>-1</sup>s<sup>-1</sup> for  $d_{\text{TEM}} \approx 17$  nm), which were comparable to or higher than the transverse relaxivity obtained with the commercial compound Endorem. Hence, our samples have proved to be promising superparamagnetic T<sub>2</sub> contrast agents for magnetic resonance imaging, in particular when  $d_{\text{TEM}} \approx 17$  nm. This conclusion is strengthened by the values reached by  $r_2/r_1$  ratio, which gives a general indication on the behavior of magnetic nanoparticles when they are used as contrast-enhancing agents. In our case, experiments carried out at the customary clinical frequency  $\nu_L \simeq 60$  MHz on the sample series with the larger diameter yielded  $r_2/r_1$  values that were three times as large as that obtained with Endorem. This allows us to envision a possible reduction in the dose of superparamagnetic CA in clinical use.



---

## CONCLUSIONS AND PERSPECTIVES

---

**I**N this PhD thesis, the multifunctional modalities of iron oxide magnetic nanoparticles are investigated, both as contrast agents in magnetic resonance imaging (MRI), and as heat mediator in magnetic fluid hyperthermia (MFH). In particular, two main research topics have been delved upon, namely the application of MFH and Hadron Therapy (HT) on cancer cells, and the role of the coating surrounding the nanoparticle core in nuclear magnetic resonance (NMR) relaxometry.

As to the role of magnetic nanoparticles as anti-tumoral therapy mediators, the INFN project *Hadromag*, in which the author was involved for the whole duration of the PhD program, has led to encouraging results. In particular, the combination of carbon-ion radiation and MNP-mediated hyperthermia has been performed *in vitro* on pancreatic BxPC<sub>3</sub> tumor cells. The experimental protocol included three different modes, in order to distinguish the contribution of radiation and that of hyperthermia, namely *irradiation only*, *irradiation after administering magnetic nanoparticles*, and *irradiation on culture cells containing magnetite nanoparticles combined with hyperthermia treatment*, carried out for 30 minutes at 42 °C, using an alternating magnetic field (frequency  $f = 109.8$  kHz and amplitude  $H = 19.5$  mT). The irradiation with C ions was performed thanks to the collaboration with the National Center for Oncological Hadron Therapy (CNAO) in Pavia, which is the only centre in Italy that uses hadron therapy with both protons and carbon ions to treat tumors. More in detail, a spread-out Bragg peak was obtained by active beam modulation in which thirty-one different energies (246–312 MeV/u, Linear Energy Transfer of about 45 keV/ $\mu$ m) were used; the cells were positioned inside a water phantom in the mid spread-out Bragg peak, and the samples underwent irradiation at different doses in the range 0–2 Gy. As a comparison, 0–7 Gy of irradiation with a photon beam were obtained with a 6 MV VARIAN Clinac linear accelerator at the Fondazione IRCCS Istituto Nazionale dei Tumori in Milano. The clonogenic survival (CS) results, evaluated after 14 days from the treatment, with respect to simple irradiation of culture cells, leads to the following conclusions:

- the toxicity linked to the MNPs cellular uptake leads to an additive killing effect of about 50–60%, for all HT/photon irradiation doses;
- hyperthermia contributes a significant killing effect, consisting in an additive 15–30% of the overall clonogenic survival, for both irradiation protocols; the action of the magnetic nanoparticles could possibly become synergistic when radiation therapy is delivered by photons;
- a significant enhancement of double-strand breaks (DSBs) in the DNA was observed 6 hours after hadron-therapy irradiation with a 0.75 Gy dose, and the administration of magnetic nanoparticles and hyperthermia, as compared to the sample which underwent irradiation only.

This shows that the combination of hadron therapy and hyperthermia applied immediately afterwards leads to an increased efficacy, and it paves the way for future preclinical—and hopefully clinical—studies. As to the future, the author is currently involved in the INFN *Prothyp* project, which sees the collaboration of the same oncological centers and universities research groups involved in the project presented in this thesis. The project aims at investigating the effect of the combination of protons and MNP-mediated hyperthermia on the same BxPC<sub>3</sub> cells. Moreover, for both carbon ions and protons, *in vivo* studies are planned to confirm the results obtained in these *in vitro* studies. Furthermore, with regards to the nanoparticles employed, research is still ongoing to understand which size works best, together with the best coating, so as to guarantee the greatest possible cellular uptake and the highest SAR, which would then increase the thermal release due to the application an alternating magnetic field.

The rationale of the second section is that coating and functionalizing MNPs can influence their magnetic properties, an aspect that is mainly due to the surface spin canting induced by the coating ligands. The relaxivities, defined as the relaxation rate of the nuclear magnetization of solvent molecules (*i.e.* water) that lie around MNPs, depend on the energy associated to the magnetic anisotropy, which is itself modified by the presence of a coating; thus, ultimately, the coating can indirectly and significantly modify the relaxation process. Moreover, it can act by slowing the rotation of the particles and perturbing the diffusion of solvent molecules close to the surface of the MNPs. For this study, we investigated aqueous dispersions of two series of maghemite ( $\gamma\text{-Fe}_2\text{O}_3$ ) superparamagnetic nanoparticles, with mean diameters  $d_{\text{TEM}} = 17 \pm 2.5$  nm and  $d_{\text{TEM}} = 8 \pm 0.4$  nm coated with four different types of biocompatible negative polyelectrolytes: poly(acrylic acid), a copolymer issued from the random esterification of poly(methacrylic acid) (PMAA) chains with poly(ethylene glycol), two comb-like polymers fabricated by reversible addition-fragmentation chain transfer based on

PMMA and poly(ethylene glycol) methyl ether methacrylate with two different chain transfer agents.

The morpho-dimensional, magnetic and relaxometric properties has been evaluated for both series; this made it possible to carry out an inter-series comparison based on the MNPs size and an intra-series analysis based on the different coatings. By increasing the size of the spherical superparamagnetic nanoparticles, a change in the NMR  $r_1$  dispersion profile occurs: all bigger samples show a continuous increase of the longitudinal relaxivity, consequently lowering the Larmor frequencies, with no detectable maximum. For example, the PAA-coated MNPs with  $d_{\text{TEM}} = 17$  nm at  $\nu_L \sim 60$  MHz show  $r_1 \approx 12 \text{ mM}^{-1}\text{s}^{-1}$  and  $r_2 \approx 400 \text{ mM}^{-1}\text{s}^{-1}$ , while at  $\nu_L \sim 0.01$  MHz,  $r_1 \approx 300 \text{ mM}^{-1}\text{s}^{-1}$  and  $r_2 \approx 270 \text{ mM}^{-1}\text{s}^{-1}$ ; the PAA-coated MNPs with  $d_{\text{TEM}} = 8$  nm at  $\nu_L \sim 60$  MHz show  $r_1 \approx 15 \text{ mM}^{-1}\text{s}^{-1}$  and  $r_2 \approx 120 \text{ mM}^{-1}\text{s}^{-1}$ , while at  $\nu_L \sim 0.01$  MHz,  $r_1 \approx 30 \text{ mM}^{-1}\text{s}^{-1}$  and  $r_2 \approx 30 \text{ mM}^{-1}\text{s}^{-1}$ . Moreover, the NMRD profiles show the same behavior for samples with the same core size but with different coatings, indicating that the type of coating used in this work does not evidently influence the longitudinal and trasversal relaxometric properties. Furthermore, by comparing our  $r_1$  and  $r_2$  with the ones of Endorem, a commercial compound of magnetite nanoparticles with a size range between 6 and 9 nm, coated with a polymeric dextran, we can say that our samples are promising superparamagnetic  $T_2$  contrast agents for MRI, especially in the case with  $d_{\text{TEM}} = 17$  nm. In our case, for the latter, and at the most used clinical frequency ( $\nu_L \sim 60$  MHz), the  $r_2/r_1$  values were three times larger than the one for Endorem, which exhibits  $r_1 \approx 12 \text{ mM}^{-1}\text{s}^{-1}$  and  $r_2 \approx 130 \text{ mM}^{-1}\text{s}^{-1}$ , allowing us to envision a possible superparamagnetic CA dose reduction in clinical use.

As to the future perspectives on this research topic, in addition to the promising physical properties shown in this thesis for the selection of MNPs that was studied, several conditions must be met for any MNPs before moving to the clinical practise. Among them, a test of the particles' toxicity, together with the contrast efficiencies of the particles in a biological medium. For this reason, *in vitro* e *in vivo* studies should be performed. Moreover, the author is currently involved in similar research on magnetic nanoparticles of smaller diameter than those studied in this thesis. If a coating effect on nuclear magnetic relaxivities exists at all, be it small as it may, it is expected to be more visible in smaller nanoparticles, where surface effects are greater.





---

## LIST OF PUBLICATIONS

---

### PUBLISHED

- [1] C. Tapeinos, F. Tomatis, M. Battaglini, A. Larrañaga, A. Marino, I. A. Telleria, M. Angelakeris, D. Debellis, F. Drago, F. Brero, et al. "Cell Membrane-Coated Magnetic Nanocubes with a Homotypic Targeting Ability Increase Intracellular Temperature due to ROS Scavenging and Act as a Versatile Theranostic System for Glioblastoma Multiforme". In: *Advanced healthcare materials* 8.18 (2019), p. 1900612.
- [2] M. Avolio, A. Guerrini, F. Brero, C. Innocenti, C. Sangregorio, M. Cobianchi, M. Mariani, F. Orsini, P. Arosio, and A. Lascialfari. "In-gel study of the effect of magnetic nanoparticles immobilization on their heating efficiency for application in Magnetic Fluid Hyperthermia". In: *Journal of Magnetism and Magnetic Materials* 471 (2019), pp. 504–512.
- [3] M. Avolio, H. Gavilán, E. Mazario, F. Brero, P. Arosio, A. Lascialfari, and M. P. Morales. "Elongated magnetic nanoparticles with high-aspect ratio: A nuclear relaxation and specific absorption rate investigation". In: *Physical Chemistry Chemical Physics* 21.34 (2019), pp. 18741–18752.
- [4] F. Brero, M. Basini, M. Avolio, F. Orsini, P. Arosio, C. Sangregorio, C. Innocenti, A. Guerrini, J. Boucard, E. Ishow, et al. "Coating Effect on the  $^1\text{H}$ —NMR Relaxation Properties of Iron Oxide Magnetic Nanoparticles". In: *Nanomaterials* 10.9 (2020), p. 1660.
- [5] F. Brero, M. Albino, A. Antocchia, P. Arosio, M. Avolio, F. Berardinelli, D. Bettega, P. Calzolari, M. Ciocca, M. Corti, et al. "Hadron therapy, magnetic nanoparticles and hyperthermia: A promising combined tool for pancreatic cancer treatment". In: *Nanomaterials* 10.10 (2020), p. 1919.
- [6] J. Wells, D. Ortega, U. Steinhoff, S. Dutz, E. Garaio, O. Sandre, E. Natividad, M. M. Cruz, F. Brero, P. Southern, et al. "Challenges and recommendations for magnetic hyperthermia characterization

measurements". In: *International Journal of Hyperthermia* 38.1 (2021), pp. 447–460.

### SUBMITTED

- [1] F. Lizzi, A. Agosti, F. Brero, R. F. Cabini, M. E. Fantacci, S. Figini, A. Lascialfari, F. Laruina, P. Oliva, S. Piffer, et al. "Quantification of pulmonary involvement in COVID-19 pneumonia by means of a cascade of two U-nets: training and assessment on multiple datasets using different annotation criteria". In: *International Journal of Computer Assisted Radiology and Surgery* (2021).

### IN PROGRESS

- [1] J. Boucard, M. Basini, A. Guerrini, F. Brero, I. Marangon, C. Innocenti, F. Gazeau, A. Lascialfari, E. Ishow, C. Sangregorio, and L. Lartigue. "Magnetic dipolar interactions and their effect on theranostic properties in magnetofluorescent nanoassemblies." In: ().

# Cell Membrane-Coated Magnetic Nanocubes with a Homotypic Targeting Ability Increase Intracellular Temperature due to ROS Scavenging and Act as a Versatile Theranostic System for Glioblastoma Multiforme

Christos Tapeinos,\* Francesca Tomatis, Matteo Battaglini, Aitor Larrañaga, Attilio Marino, Iker Aguirrezabal Telleria, Makis Angelakeris, Doriana Debellis, Filippo Drago, Francesca Brero, Paolo Arosio, Alessandro Lascialfari, Andrea Petretto, Edoardo Sinibaldi, and Gianni Ciofani\*

In this study, hybrid nanocubes composed of magnetite ( $\text{Fe}_3\text{O}_4$ ) and manganese dioxide ( $\text{MnO}_2$ ), coated with U-251 MG cell-derived membranes (CM-NCubes) are synthesized. The CM-NCubes demonstrate a concentration-dependent oxygen generation (up to 15%), and, for the first time in the literature, an intracellular increase of temperature ( $6^\circ\text{C}$ ) due to the exothermic scavenging reaction of hydrogen peroxide ( $\text{H}_2\text{O}_2$ ) is showed. Internalization studies demonstrate that the CM-NCubes are internalized much faster and at a higher extent by the homotypic U-251 MG cell line compared to other cerebral cell lines. The ability of the CM-NCubes to cross an in vitro model of the blood-brain barrier is also assessed. The CM-NCubes show the ability to respond to a static magnet and to accumulate in cells even under flowing conditions. Moreover, it is demonstrated that  $500\ \mu\text{g mL}^{-1}$  of sorafenib-loaded or unloaded CM-NCubes are able to induce cell death by apoptosis in U-251 MG spheroids that are used as a tumor model, after their exposure to an alternating magnetic field (AMF). Finally, it is shown that the combination of sorafenib and AMF induces a higher enzymatic activity of caspase 3 and caspase 9, probably due to an increment in reactive oxygen species by means of hyperthermia.

Dr. C. Tapeinos, M. Battaglini, Dr. A. Marino, Prof. G. Ciofani  
Smart Bio-Interfaces


Istituto Italiano di Tecnologia  
56025 Pontedera, Italy  
E-mail: christos.tapeinos@iit.it; gianni.ciofani@iit.it

F. Tomatis, Prof. G. Ciofani  
Department of Mechanical and Aerospace Engineering  
Politecnico di Torino  
10129 Torino, Italy

M. Battaglini  
The Biorobotics Institute  
Scuola Superiore Sant'Anna  
56025 Pontedera, Italy

Dr. A. Larrañaga  
Department of Mining-Metallurgy Engineering and Materials  
Science & POLYMAT  
University of the Basque Country  
48013 Bilbao, Spain

Dr. I. A. Telleria  
Department of Chemical and Environmental Engineering  
Engineering School of the University of the Basque Country (UPV/EHU)  
48013 Bilbao, Spain

 The ORCID identification number(s) for the author(s) of this article can be found under <https://doi.org/10.1002/adhm.201900612>.

© 2019 The Authors. Published by WILEY-VCH Verlag GmbH & Co. KGaA, Weinheim. This is an open access article under the terms of the Creative Commons Attribution License, which permits use, distribution and reproduction in any medium, provided the original work is properly cited.

The copyright line for this article was changed on 13 June 2020 after original online publication.

DOI: 10.1002/adhm.201900612

Adv. Healthcare Mater. 2019, 8, 1900612

1900612 (1 of 19)

Prof. M. Angelakeris  
Department of Physics  
Aristotle University of Thessaloniki  
54124 Thessaloniki, Greece

D. Debellis  
Electron Microscopy Facility  
Istituto Italiano di Tecnologia  
16163 Genova, Italy

F. Drago  
Nanochemistry Department  
Istituto Italiano di Tecnologia  
16163 Genova, Italy

F. Brero  
Department of Physics and INSTM  
Università degli Studi di Pavia  
27100 Pavia, Italy

Prof. P. Arosio, Prof. A. Lascialfari  
Department of Physics and INSTM  
Università degli Studi di Milano  
20133 Milano, Italy

Dr. A. Petretto  
Core Facilities-Clinical Proteomics and Metabolomics Laboratory  
IRCCS Istituto Giannina Gaslini  
16147 Genova, Italy

Dr. E. Sinibaldi  
Center for Micro-BioRobotics  
Istituto Italiano di Tecnologia  
56025 Pontedera, Italy

© 2019 The Authors. Published by WILEY-VCH Verlag GmbH & Co. KGaA, Weinheim



Cite this: *Phys. Chem. Chem. Phys.*,  
2019, 21, 18741

## Elongated magnetic nanoparticles with high-aspect ratio: a nuclear relaxation and specific absorption rate investigation†

Matteo Avolio,<sup>a</sup> Helena Gavilán,<sup>b</sup> Eva Mazario,<sup>b</sup> Francesca Brero,<sup>a</sup>  
Paolo Arosio,<sup>c</sup> Alessandro Lascialfari<sup>c</sup> and M. Puerto Morales<sup>b</sup>

Medical application of nanotechnology implies the development of nanomaterials capable of being functional in different biological environments. In this sense, elongated nanoparticles (e-MNPs) with high-aspect ratio have demonstrated more effective particle cellular internalization, which is favoured by the increased surface area. This paper makes use of an environmentally friendly hydrothermal method to produce magnetic iron oxide e-MNPs, starting from goethite precursors. At high temperatures ( $T_d$ ) goethite transforms into hematite, which subsequently reduces to magnetite when exposed to a hydrogen atmosphere for a certain time. It is shown that by adjusting  $T_d$  it is possible to obtain  $\text{Fe}_3\text{O}_4$  e-MNPs with partially controlled specific surface area and magnetic properties, attributed to different porosity of the samples. The particles' efficiencies for diagnostic and therapeutic purposes (in magnetic resonance imaging and magnetic fluid hyperthermia, respectively) are very good in terms of clinical standards, some samples showing transversal proton nuclear relaxivity  $r_2$  ( $B_0 = 1.33 \text{ T}$ ) =  $340 \text{ s}^{-1} \text{ mM}^{-1}$  and specific absorption rate  $\text{SAR} > 370 \text{ W g}^{-1}$  at high field amplitudes ( $B_0 = 55 \text{ mT}$ ). Direct correlations between the SAR, relaxivity, magnetic properties and porosity of the samples are found, and the physico-chemical processes underneath these correlations are investigated. Our results open the possibility of using very efficient high-aspect ratio elongated nanoparticles with optimized chemico-physical properties for biomedical applications.

Received 18th June 2019,  
Accepted 2nd August 2019

DOI: 10.1039/c9cp03441b

rsc.li/pccp

### Introduction

Magnetic nanoparticles (MNPs) are being used for several biomedical applications already in clinics and are promising tools to strongly improve diagnostics and cancer therapy in the coming years.<sup>1–4</sup> In particular, MNPs can be utilized as contrast agents in Magnetic Resonance Imaging (MRI), allowing one to obtain higher image contrast and more generally clearer diagnostic information.<sup>5,6</sup> These systems shorten the nuclear relaxation times of the  $^1\text{H}$  nuclei in the region where they accumulate, thus allowing better tissue contrast. For cancer therapy, instead, MNPs are already used for the treatment of glioblastoma multiforme (see *e.g.* results reported on [www.Magforce.com](http://www.Magforce.com)). Such

treatment is being developed and extended to prostate cancer, and to some other poor-prognosis tumours,<sup>7</sup> becoming known as Magnetic Fluid Hyperthermia (MFH). MFH is based on the use of MNPs, which are first injected into the tumour and then exposed to an alternating magnetic field (AMF), which allows local heat release that weakens or kills the tumour cells.

The AMF amplitude  $H$  and frequency  $f$  suitable for application to patients must satisfy the Brezovich criterion,  $Hf < 4.85 \times 10^8 \text{ A m}^{-1} \text{ s}^{-1}$ , to avoid any side effects.<sup>8</sup> During the exposure to the AMF, MNPs transfer thermal energy from the field to the tumour due to strong interactions between their magnetic moments and the field.<sup>9–11</sup>

The most widely used MNPs are composed of a magnetic core of iron oxides, typically magnetite ( $\text{Fe}_3\text{O}_4$ ) or maghemite ( $\gamma\text{-Fe}_2\text{O}_3$ ), which are preferred due to their high magnetization coming from a ferrimagnetic structure, and their high biocompatibility.<sup>12</sup> Recently, other ferrites that include cobalt, manganese or nickel in their composition were studied for similar applications,<sup>13–15</sup> as such elements provide advantageous magnetic features,<sup>16</sup> however their cytotoxicity is still unclear.<sup>17</sup>

Magnetic cores used in biomedical applications are typically covered by organic moieties, like *e.g.* sugars or polymers, in order to guarantee biocompatibility, to prevent MNPs from aggregation,

<sup>a</sup> Dipartimento di Fisica, INFN and INSTM, Università degli Studi di Pavia, Via Bassi 6, 27100 Pavia, Italy. E-mail: [matteo.avolio01@universitadipavia.it](mailto:matteo.avolio01@universitadipavia.it)

<sup>b</sup> Departamento de Energía, Mediambiente y Salud, Instituto de Ciencia de Materiales de Madrid, ICMN/CSIC, Cantoblanco, 28049 Madrid, Spain

<sup>c</sup> Dipartimento di Fisica, INFN and INSTM, Università degli Studi di Milano, Via Celoria 16, 20133 Milano, Italy

† Electronic supplementary information (ESI) available: Additional information about the synthesis, XRD patterns and crystal size analysis, IR absorption spectra and DLS data, and partially reduced samples with mixed compositions of hematite–magnetite. See DOI: 10.1039/c9cp03441b



Contents lists available at ScienceDirect

Journal of Magnetism and Magnetic Materials

journal homepage: [www.elsevier.com/locate/jmmm](http://www.elsevier.com/locate/jmmm)

## Research articles

## In-gel study of the effect of magnetic nanoparticles immobilization on their heating efficiency for application in Magnetic Fluid Hyperthermia

Matteo Avolio<sup>a,\*</sup>, Andrea Guerrini<sup>b</sup>, Francesca Brero<sup>a</sup>, Claudia Innocenti<sup>b</sup>, Claudio Sangregorio<sup>b,c</sup>, Marco Cobianchi<sup>a</sup>, Manuel Mariani<sup>a</sup>, Francesco Orsini<sup>d</sup>, Paolo Arosio<sup>d</sup>, Alessandro Lascialfari<sup>d</sup><sup>a</sup> Dipartimento di Fisica, INFN and INSTM, Università degli Studi di Pavia, Via Bassi 6, 27100 Pavia, Italy<sup>b</sup> Dipartimento di Chimica and INSTM, Università degli studi di Firenze, Via della Lastruccia 6, Sesto F.no (FI), Italy<sup>c</sup> ICCOM-CNR, Via della Lastruccia 6, Sesto F.no(FI), Italy<sup>d</sup> Dipartimento di Fisica, INFN and INSTM, Università degli Studi di Milano, Via Celoria 16, 20133 Milano, Italy

## ARTICLE INFO

**Keywords:**  
Magnetic Fluid Hyperthermia  
Magnetic nanoparticles  
Superparamagnetism  
Specific Absorption Rate  
Relaxation times  
Brownian motion

## ABSTRACT

Recent studies on magnetic nanoparticles (MNPs) used for Magnetic Fluid Hyperthermia treatments have shown that Brownian rotation is suppressed when they are confined within a cell. To investigate this effect we conducted a systematic study of the Specific Absorption Rate (SAR) of colloidal suspensions of MNPs in water and gels at different agarose concentration. SAR measurements were conducted by varying the frequency ( $f = 110\text{--}990\text{ kHz}$ ) and amplitude (up to  $17\text{ kA/m}$ ) of the applied alternating magnetic field (AMF). MNP samples with different diameter ( $d = 10, 14, \text{ and } 18\text{ nm}$ ) were used. Our results show that Néel relaxation dominates SAR with negligible contribution from Brownian motion for smaller MNPs ( $d = 10\text{ nm}$ ). For the largest MNPs ( $d = 18\text{ nm}$ ) we observed a more significant SAR decrease in gel suspensions as compared to those in solution. In particular, when applying AMFs as the ones used in a clinical setting ( $16.2\text{ kA/m}$  at  $f = 110\text{ kHz}$ ), we measured SAR value of  $67\text{ W/g}$  in solution and  $25\text{ W/g}$  in gel. This experimental finding demonstrates that investigation of MNPs properties should be conducted in media with viscosity similar to the one found in mammalian tissues.

## 1. Introduction

Hyperthermia is an antitumoral therapy consisting in a temperature rise up to  $43\text{ }^\circ\text{C}$ , with the aim of damaging cancer cells by denaturing their basic molecular structures, such as DNA or enzymes [1,2]. This aim is achieved for instance by the so-called Magnetic Fluid Hyperthermia (MFH), that employs magnetic nanoparticles (MNPs), with the advantage of producing the temperature rise only within the neoplastic region where they are located. In this technique, colloidal solutions of biocompatible MNPs dispersed in physiological liquids and injected e.g., directly inside the tumour, release heat once exposed to an alternating magnetic field (AMF) operating at safe values of frequency and amplitude [3,4].

In most cases, for in vivo applications, MNPs consist of a magnetic core made of iron oxides, known to have a low toxicity [3,5], coated by organic biocompatible moieties. The core size is generally so small (the equivalent diameter typically is less than  $20\text{ nm}$ ) that the MNPs result to be superparamagnetic [1,6,7]. In the superparamagnetic regime the MNPs magnetization, also called superspin, can fluctuate between the

two opposite directions of the easy axis determined by the magnetic anisotropy, with a characteristic relaxation time,  $\tau_N$ . According to the Néel model for non-interacting particles  $\tau_N$  depends on the core volume of the particles ( $V$ ), the anisotropy constant ( $K_u$ ) and the temperature of the system ( $T$ ), and its expression is given by the Arrhenius law:

$$\tau_N = \tau_0 e^{K_u V / (k_B T)} \quad (1)$$

In Eq. (1)  $\tau_0$  is generally assumed of the order of  $10^{-9}\text{ s}$  [8,9] and  $k_B$  is the Boltzmann constant.

In a solvent the superspin orientation can change also through the physical process of rotation of the entire particle, which occurs in a characteristic time called Brown relaxation time  $\tau_B$  [10] expressed by:

$$\tau_B = \frac{3\eta V_h}{k_B T} \quad (2)$$

where  $V_h$  is the hydrodynamic volume of the particles and  $\eta$  is the local viscosity of the medium. Thus, an effective relaxation time  $\tau$  that accounts for both Néel and Brown mechanisms can be defined as:

\* Corresponding author.

E-mail address: [matteo.avolio01@universitadipavia.it](mailto:matteo.avolio01@universitadipavia.it) (M. Avolio).<https://doi.org/10.1016/j.jmmm.2018.09.111>

Received 22 June 2018; Received in revised form 21 September 2018; Accepted 28 September 2018

Available online 29 September 2018

0304-8853/ © 2018 Elsevier B.V. All rights reserved.



Article

# Hadron Therapy, Magnetic Nanoparticles and Hyperthermia: A Promising Combined Tool for Pancreatic Cancer Treatment

Francesca Brero <sup>1,\*</sup> , Martin Albino <sup>2</sup> , Antonio Antocchia <sup>3</sup>, Paolo Arosio <sup>4</sup> , Matteo Avolio <sup>1</sup>, Francesco Berardinelli <sup>3</sup>, Daniela Bettega <sup>4</sup>, Paola Calzolari <sup>4</sup>, Mario Ciocca <sup>5</sup>, Maurizio Corti <sup>1</sup>, Angelica Facoetti <sup>5</sup>, Salvatore Gallo <sup>4</sup> , Flavia Groppi <sup>6</sup>, Andrea Guerrini <sup>2</sup> , Claudia Innocenti <sup>2,7</sup> , Cristina Lenardi <sup>4,8</sup> , Silvia Locarno <sup>4</sup> , Simone Manenti <sup>6</sup> , Renato Marchesini <sup>4</sup>, Manuel Mariani <sup>1</sup>, Francesco Orsini <sup>4</sup> , Emanuele Pignoli <sup>9</sup>, Claudio Sangregorio <sup>2,7,10</sup>, Ivan Veronese <sup>4</sup> and Alessandro Lascialfari <sup>1,\*</sup>

<sup>1</sup> Dipartimento di Fisica and INFN, Università degli Studi di Pavia, 27100 Pavia, Italy; matteo.avolio01@universitadipavia.it (M.A.); maurizio.corti@unipv.it (M.C.); manuel.mariani@unipv.it (M.M.)

<sup>2</sup> Dipartimento di Chimica, Università di Firenze and INSTM, 50019 Sesto Fiorentino (FI), Italy; martin.albino@unifi.it (M.A.); andrea.guerrini@sns.it (A.G.); claudia.innocenti@unifi.it (C.I.); claudio.sangregorio@iccom.cnr.it (C.S.)

<sup>3</sup> Dipartimento di Scienze and INFN, Università Roma Tre, 00146 Roma, Italy; antonio.antocchia@uniroma3.it (A.A.); francesco.berardinelli@uniroma3.it (F.B.)

<sup>4</sup> Dipartimento di Fisica and INFN, Università degli Studi di Milano, 20133 Milano, Italy; paolo.arosio@unimi.it (P.A.); daniela.bettega@mi.infn.it (D.B.); paola.calzolari@unimi.it (P.C.); salvatore.gallo@unimi.it (S.G.); cristina.lenardi@mi.infn.it (C.L.); silvia.locarno@unimi.it (S.L.); renato.marchesini@alice.it (R.M.); francesco.orsini@unimi.it (F.O.); ivan.veronese@unimi.it (I.V.)

<sup>5</sup> Fondazione CNAO, 27100 Pavia, Italy; mario.ciocca@cnao.it (M.C.); angelica.facoetti@cnao.it (A.F.)

<sup>6</sup> Dipartimento di Fisica, Università degli Studi di Milano and INFN, Lab. LASA, 20090 Segrate (MI), Italy; flavia.groppi@mi.infn.it (F.G.); simone.manenti@mi.infn.it (S.M.)

<sup>7</sup> ICCOM-CNR, 50019 Sesto Fiorentino (FI), Italy

<sup>8</sup> C.I.Ma.I.Na., Centro Interdisciplinare Materiali e Interfacce Nanostrutturati, 20133 Milano, Italy

<sup>9</sup> Fondazione IRCSS Istituto Nazionale dei tumori, 20133 Milano, Italy;

emanuele.pignoli@istitutotumori.mi.it

<sup>10</sup> INFN, Sezione di Firenze, 50019 Sesto Fiorentino (FI), Italy

\* Correspondence: francesca.brero01@universitadipavia.it (F.B.); alessandro.lascialfari@unipv.it (A.L.); Tel.: +39-0382-987-483 (F.B. & A.L.)

Received: 31 August 2020; Accepted: 18 September 2020; Published: 25 September 2020



**Abstract:** A combination of carbon ions/photons irradiation and hyperthermia as a novel therapeutic approach for the in-vitro treatment of pancreatic cancer BxPC3 cells is presented. The radiation doses used are 0–2 Gy for carbon ions and 0–7 Gy for 6 MV photons. Hyperthermia is realized via a standard heating bath, assisted by magnetic fluid hyperthermia (MFH) that utilizes magnetic nanoparticles (MNPs) exposed to an alternating magnetic field of amplitude 19.5 mTesla and frequency 109.8 kHz. Starting from 37 °C, the temperature is gradually increased and the sample is kept at 42 °C for 30 min. For MFH, MNPs with a mean diameter of 19 nm and specific absorption rate of  $110 \pm 30 \text{ W/g}_{\text{Fe}_3\text{O}_4}$  coated with a biocompatible ligand to ensure stability in physiological media are used. Irradiation diminishes the clonogenic survival to an extent that depends on the radiation type, and its decrease is amplified both by the MNPs cellular uptake and the hyperthermia protocol. Significant increases in DNA double-strand breaks at 6 h are observed in samples exposed to MNP uptake, treated with 0.75 Gy carbon-ion irradiation and hyperthermia. The proposed experimental protocol, based on the



Article

# Coating Effect on the $^1\text{H}$ —NMR Relaxation Properties of Iron Oxide Magnetic Nanoparticles

Francesca Brero <sup>1,\*</sup>, Martina Basini <sup>2</sup>, Matteo Avolio <sup>1</sup>, Francesco Orsini <sup>2</sup>, Paolo Arosio <sup>2</sup>, Claudio Sangregorio <sup>3,4</sup>, Claudia Innocenti <sup>3,4</sup>, Andrea Guerrini <sup>4</sup>, Joanna Boucard <sup>5</sup>, Eléna Ishow <sup>5</sup>, Marc Lecouvey <sup>6</sup>, Jérôme Fresnais <sup>7</sup>, Lénia Lartigue <sup>5</sup> and Alessandro Lascialfari <sup>1,2</sup>

<sup>1</sup> Dipartimento di Fisica and INFN, Università degli Studi di Pavia, Via Bassi 6, 27100 Pavia, Italy; matteo.avolio01@universitadipavia.it (M.A.); alessandro.lascialfari@unipv.it (A.L.)

<sup>2</sup> Dipartimento di Fisica and INFN, Università degli Studi di Milano, Via Celoria 16, 20133 Milano, Italy; martina.basini@gmail.com (M.B.); francesco.orsini@unimi.it (F.O.); paolo.ariosio@unimi.it (P.A.)

<sup>3</sup> ICCOM-CNR, via Madonna del Piano 10, 50019 Sesto Fiorentino (FI), Italy; csangregorio@iccom.cnr.it (C.S.); claudia.innocenti@unifi.it (C.I.)

<sup>4</sup> Dipartimento di Chimica "U. Schiff" and INSTM, Università degli Studi di Firenze, Via della Lastruccia 3-13, 50019 Sesto Fiorentino (FI), Italy; andrea.guerrini@sns.it

<sup>5</sup> CNRS, CEISAM UMR 6230, Université de Nantes, F-44000 Nantes, France; joanna.boucard@laposte.net (J.B.); elena.ishow@univ-nantes.fr (E.I.); lenia.lartigue@univ-nantes.fr (L.L.)

<sup>6</sup> CSPBAT-UMR CNRS 7244, Université Sorbonne Paris Nord, 74 rue Marcel Cachin, 93017 Bobigny, France; marc.lecouvey@univ-paris13.fr

<sup>7</sup> CNRS, Laboratoire de Physico-chimie des Electrolytes et Nanosystèmes Interfaciaux, Sorbonne Université, PHENIX—UMR 8234, CEDEX 05 F-75252 Paris, France; jerome.fresnais@sorbonne-universite.fr

\* Correspondence: francesca.brero01@universitadipavia.it; Tel.: +39-0382-987-483

Received: 24 June 2020; Accepted: 19 August 2020; Published: 24 August 2020



**Abstract:** We present a  $^1\text{H}$  Nuclear Magnetic Resonance (NMR) relaxometry experimental investigation of two series of magnetic nanoparticles, constituted of a maghemite core with a mean diameter  $d_{\text{TEM}} = 17 \pm 2.5$  nm and  $8 \pm 0.4$  nm, respectively, and coated with four different negative polyelectrolytes. A full structural, morpho-dimensional and magnetic characterization was performed by means of Transmission Electron Microscopy, Atomic Force Microscopy and DC magnetometry. The magnetization curves showed that the investigated nanoparticles displayed a different approach to the saturation depending on the coatings, the less steep ones being those of the two samples coated with P(MAA-*stat*-MAPEG), suggesting the possibility of slightly different local magnetic disorders induced by the presence of the various polyelectrolytes on the particles' surface. For each series,  $^1\text{H}$  NMR relaxivities were found to depend very slightly on the surface coating. We observed a higher transverse nuclear relaxivity,  $r_2$ , at all investigated frequencies ( $10 \text{ kHz} \leq \nu_L \leq 60 \text{ MHz}$ ) for the larger diameter series, and a very different frequency behavior for the longitudinal nuclear relaxivity,  $r_1$ , between the two series. In particular, the first one ( $d_{\text{TEM}} = 17$  nm) displayed an anomalous increase of  $r_1$  toward the lowest frequencies, possibly due to high magnetic anisotropy together with spin disorder effects. The other series ( $d_{\text{TEM}} = 8$  nm) displayed a  $r_1$  vs.  $\nu_L$  behavior that can be described by the Roch's heuristic model. The fitting procedure provided the distance of the minimum approach and the value of the Néel reversal time ( $\tau \approx 3.5 \div 3.9 \cdot 10^{-9}$  s) at room temperature, confirming the superparamagnetic nature of these compounds.

**Keywords:** magnetic nanoparticles; Superparamagnetism; Nuclear Magnetic Resonance; Magnetic Resonance Imaging; coating; polyelectrolytes

## Challenges and recommendations for magnetic hyperthermia characterization measurements

J. Wells<sup>a</sup> , D. Ortega<sup>b,c</sup> , U. Steinhoff<sup>a</sup> , S. Dutz<sup>d</sup> , E. Garaio<sup>e</sup>, O. Sandre<sup>f,g</sup> , E. Natividad<sup>h</sup> , M. M. Cruz<sup>i</sup>, F. Brero<sup>j</sup> , P. Southern<sup>k,l</sup> , Q. A. Pankhurst<sup>k,l</sup> , S. Spassov<sup>m</sup>  and the RADIOMAG consortium

<sup>a</sup>Physikalisch-Technische Bundesanstalt, Berlin, Germany; <sup>b</sup>Condensed Matter Physics department, Faculty of Sciences, Campus Universitario Río San Pedro s/n, Cádiz, Spain; <sup>c</sup>IMDEA Nanociencia, Ciudad Universitaria de Cantoblanco, Madrid, Spain; <sup>d</sup>Technische Universität Ilmenau, Institut für Biomedizinische Technik und Informatik, Ilmenau, Germany; <sup>e</sup>Nafarroako Unibertsitate Publikoan, Pamplona, Spain; <sup>f</sup>Université de Bordeaux, Pessac, France; <sup>g</sup>CNRS, Laboratoire de Chimie des Polymères Organiques, Pessac, France; <sup>h</sup>Instituto de Nanociencia y Materiales de Aragón (INMA), CSIC-Universidad de Zaragoza, Zaragoza, Spain; <sup>i</sup>BiolSI, Faculdade de Ciências, Universidade de Lisboa, Lisboa, Portugal; <sup>j</sup>Dipartimento di Fisica, Università degli studi di Pavia, Pavia, Italy; <sup>k</sup>Healthcare Biomagnetics Laboratory, University College London, London, UK; <sup>l</sup>Resonant Circuits Limited, London, UK; <sup>m</sup>Centre de Physique du Globe de l'Institut Royal Météorologique, Dourbes, Belgium

### ABSTRACT

**Purpose:** The localized heating of magnetic nanoparticles (MNPs) *via* the application of time-varying magnetic fields – a process known as magnetic field hyperthermia (MFH) – can greatly enhance existing options for cancer treatment; but for broad clinical uptake its optimization, reproducibility and safety must be comprehensively proven. As part of this effort, the quantification of MNP heating – characterized by the specific loss power (SLP), measured in W/g, or by the intrinsic loss power (ILP), in Hm<sup>2</sup>/kg – is frequently reported. However, in SLP/ILP measurements to date, the apparatus, the analysis techniques and the field conditions used by different researchers have varied greatly, leading to questions as to the reproducibility of the measurements.

**Materials and Methods:** An interlaboratory study (across  $N = 21$  European sites) of calorimetry measurements that constitutes a snapshot of the current state-of-the-art within the MFH community has been undertaken. Identical samples of two stable nanoparticle systems were distributed to all participating laboratories. Raw measurement data as well as the results of in-house analysis techniques were collected along with details of the measurement apparatus used. Raw measurement data was further reanalyzed by universal application of the corrected-slope method to examine relative influences of apparatus and results processing.

**Results:** The data show that although there is very good intralaboratory repeatability, the overall interlaboratory measurement accuracy is poor, with the consolidated ILP data having standard deviations on the mean of ca.  $\pm 30\%$  to  $\pm 40\%$ . There is a strong systematic component to the uncertainties, and a clear rank correlation between the measuring laboratory and the ILP. Both of these are indications of a current lack of normalization in this field. A number of possible sources of systematic uncertainties are identified, and means determined to alleviate or minimize them. However, no single dominant factor was identified, and significant work remains to ascertain and remove the remaining uncertainty sources.

**Conclusion:** We conclude that the study reveals a current lack of harmonization in MFH characterization of MNPs, and highlights the growing need for standardized, quantitative characterization techniques for this emerging medical technology.

### ARTICLE HISTORY

Received 24 August 2020  
Revised 12 February 2021  
Accepted 15 February 2021

### KEYWORDS



Thermal dosimetry; thermal ablation; quality assurance; physics; thermal dose


## 1. Introduction

Cancer remains a leading public health challenge facing humanity in the twenty first century. In 2018 there were 17 million new cases worldwide, with an anticipated increase to 27.5 million by 2040 [1]. The most established methods of cancer treatment at present are surgery, radiotherapy and chemotherapy. These techniques have shown significant progress in recent decades, and are complemented today by other more recently developed techniques such as

immunotherapy [2] or hormonotherapy [3]. Despite the progress made, there remains a significant need for innovative approaches which improve patient outcomes, while minimizing the trauma and collateral damage associated with established cancer therapies.

Magnetic field hyperthermia (MFH), also referred to as magnetic fluid hyperthermia, is an emerging technique capable of complementing or replacing established cancer therapies [4,5]. MFH requires magnetic nanoparticles (MNPs)

CONTACT J. Wells  [james.wells@ptb.de](mailto:james.wells@ptb.de)  Physikalisch-Technische Bundesanstalt, Berlin, Germany

 Supplemental data for this article can be accessed [here](#).

© 2021 The Author(s). Published with license by Taylor & Francis Group, LLC

This is an Open Access article distributed under the terms of the Creative Commons Attribution License (<http://creativecommons.org/licenses/by/4.0/>), which permits unrestricted use, distribution, and reproduction in any medium, provided the original work is properly cited.



---

## BIBLIOGRAPHY

---

- [1] S. Srinivasan, A. M. Kannan, N. Kothurkar, Y. Khalil, and S. Kuravi. *Nanomaterials for energy and environmental applications*. 2015 (cit. on p. 1).
- [2] M. Latorre and C. Rinaldi. “Applications of magnetic nanoparticles in medicine: magnetic fluid hyperthermia”. In: *Puerto Rico health sciences journal* 28.3 (2009) (cit. on p. 1).
- [3] B. Issa and I. M. Obaidat. “Magnetic nanoparticles as MRI contrast agents”. In: *Magn. Reson. Imaging* 378 (2019), p. 40 (cit. on p. 1).
- [4] D. Yoo, J.-H. Lee, T.-H. Shin, and J. Cheon. “Theranostic magnetic nanoparticles”. In: *Accounts of chemical research* 44.10 (2011), pp. 863–874 (cit. on p. 2).
- [5] O. L. Gobbo, K. Sjaastad, M. W. Radomski, Y. Volkov, and A. Prina-Mello. “Magnetic nanoparticles in cancer theranostics”. In: *Theranostics* 5.11 (2015), p. 1249 (cit. on p. 2).
- [6] P. Reimer and T. Balzer. “Ferucarbotran (Resovist): a new clinically approved RES-specific contrast agent for contrast-enhanced MRI of the liver: properties, clinical development, and applications”. In: *European radiology* 13.6 (2003), pp. 1266–1276 (cit. on p. 2).
- [7] Y. X. J. Wang. “Current status of superparamagnetic iron oxide contrast agents for liver magnetic resonance imaging”. In: *World Journal of Gastroenterology* 21.47 (2015), p. 13400 (cit. on p. 2).
- [8] *MagForce*: <https://www.magforce.com/home/> (cit. on pp. 2, 19, 20).
- [9] A. Ionescu, J. Llandro, and K. R. A. Ziebeck. *Magnetism, Magnetic Materials, and Nanoparticles*. 2019, pp. 1–51 (cit. on pp. 8, 10).
- [10] A. P. Guimarães and A. P. Guimaraes. *Principles of nanomagnetism*. Vol. 7. Springer, 2009 (cit. on pp. 8, 11).
- [11] V. K. Varadan, L. Chen, and J. Xie. *Nanomedicine: Design and Applications of Magnetic Nanomaterials, Nanosensors and Nanosystems*. John Wiley & Sons, 2008 (cit. on p. 9).

- [12] G. C. Papaefthymiou. "Nanoparticle magnetism". In: *Nano Today* 4.5 (2009), pp. 438–447 (cit. on p. 10).
- [13] C. Binns. "Medical applications of magnetic nanoparticles". In: *Frontiers of Nanoscience*. Vol. 6. Elsevier, 2014, pp. 217–258 (cit. on p. 11).
- [14] F. Burrows. "A model of magnetic hyperthermia". PhD thesis. University of York, 2012 (cit. on p. 15).
- [15] E. Alphandéry. "Iron oxide nanoparticles for therapeutic applications". In: *Drug discovery today* 25.1 (2020), pp. 141–149 (cit. on p. 18).
- [16] N. T. Thanh. *Clinical applications of magnetic nanoparticles: From Fabrication to Clinical Applications*. CRC Press, 2018 (cit. on p. 18).
- [17] X. Liu, Y. Zhang, Y. Wang, W. Zhu, G. Li, X. Ma, Y. Zhang, S. Chen, S. Tiwari, K. Shi, et al. "Comprehensive understanding of magnetic hyperthermia for improving antitumor therapeutic efficacy". In: *Theranostics* 10.8 (2020), p. 3793 (cit. on pp. 19, 22).
- [18] A. Rajan and N. K. Sahu. "Review on magnetic nanoparticle-mediated hyperthermia for cancer therapy". In: *Journal of Nanoparticle Research* 22.11 (2020), pp. 1–25 (cit. on p. 19).
- [19] P. Moroz, S. Jones, and B. Gray. "Magnetically mediated hyperthermia: current status and future directions". In: *International Journal of Hyperthermia* 18.4 (2002), pp. 267–284 (cit. on p. 19).
- [20] Y. Yagawa, K. Tanigawa, Y. Kobayashi, and M. Yamamoto. "Cancer immunity and therapy using hyperthermia with immunotherapy, radiotherapy, chemotherapy, and surgery". In: *Journal of Cancer Metastasis and Treatment* 3 (2017), pp. 218–230 (cit. on p. 19).
- [21] C. Blanco-Andujar, F. Teran, and D. Ortega. "Current outlook and perspectives on nanoparticle-mediated magnetic hyperthermia". In: *Iron oxide nanoparticles for biomedical applications*. Elsevier, 2018, pp. 197–245 (cit. on p. 19).
- [22] R. Gilchrist, R. Medal, W. D. Shorey, R. C. Hanselman, J. C. Parrott, and C. B. Taylor. "Selective inductive heating of lymph nodes". In: *Annals of surgery* 146.4 (1957), p. 596 (cit. on p. 19).
- [23] A. Jordan. "MagForce® Nanotherapy: with tumor-specific nanoparticles against cancer". In: *VDI BERICHTE* 1920 (2005), p. 111 (cit. on p. 19).
- [24] A. Jordan, R. Scholz, K. Maier-Hauff, M. Johannsen, P. Wust, J. Nadobny, H. Schirra, H. Schmidt, S. Deger, S. Loening, et al. "Presentation of a new magnetic field therapy system for the treatment of human solid tumors with magnetic fluid hyperthermia". In: *Journal of magnetism and magnetic materials* 225.1-2 (2001), pp. 118–126 (cit. on p. 19).

- [25] F. Brero, M. Albino, A. Antoccia, P. Arosio, M. Avolio, F. Berardinelli, D. Bettega, P. Calzolari, M. Ciocca, M. Corti, et al. "Hadron therapy, magnetic nanoparticles and hyperthermia: A promising combined tool for pancreatic cancer treatment". In: *Nanomaterials* 10.10 (2020), p. 1919 (cit. on pp. 19, 43).
- [26] K. Maier-Hauff, R. Rothe, R. Scholz, U. Gneveckow, P. Wust, B. Thiesen, A. Feussner, A. von Deimling, N. Waldoefner, R. Felix, et al. "Intracranial thermotherapy using magnetic nanoparticles combined with external beam radiotherapy: results of a feasibility study on patients with glioblastoma multiforme". In: *Journal of neuro-oncology* 81.1 (2007), pp. 53–60 (cit. on p. 19).
- [27] M. Johannsen, B. Thiesen, P. Wust, and A. Jordan. "Magnetic nanoparticle hyperthermia for prostate cancer". In: *International Journal of Hyperthermia* 26.8 (2010), pp. 790–795 (cit. on p. 19).
- [28] A. Jordan, R. Scholz, P. Wust, H. Fähling, and R. Felix. "Magnetic fluid hyperthermia (MFH): Cancer treatment with AC magnetic field induced excitation of biocompatible superparamagnetic nanoparticles". In: *Journal of Magnetism and Magnetic materials* 201.1-3 (1999), pp. 413–419 (cit. on p. 19).
- [29] I. A. Brezovich. "Low frequency hyperthermia: capacitive and ferromagnetic thermoseed methods". In: *Med. Phys. Monogr* 16 (1988), pp. 82–111 (cit. on p. 20).
- [30] H. Mamiya, Y. Takeda, T. Naka, N. Kawazoe, G. Chen, and B. Jeyadevan. "Practical solution for effective whole-body magnetic fluid hyperthermia treatment". In: *Journal of Nanomaterials* (2017) (cit. on pp. 20, 21).
- [31] I. M. Obaidat, B. Issa, and Y. Haik. "Magnetic properties of magnetic nanoparticles for efficient hyperthermia". In: *Nanomaterials* 5.1 (2014), pp. 63–89 (cit. on p. 20).
- [32] D. Ortega and Q. A. Pankhurst. "Magnetic hyperthermia". In: *Nanoscience* 1.60 (2013), e88 (cit. on pp. 20, 53).
- [33] R. Hergt and S. Dutz. "Magnetic particle hyperthermia—biophysical limitations of a visionary tumour therapy". In: *Journal of Magnetism and Magnetic Materials* 311.1 (2007), pp. 187–192 (cit. on p. 20).
- [34] J. Carrey, B. Mehdaoui, and M. Respaud. "Simple models for dynamic hysteresis loop calculations of magnetic single-domain nanoparticles: Application to magnetic hyperthermia optimization". In: *Journal of Applied Physics* 109.8 (2011), p. 083921 (cit. on pp. 21, 22, 24).

- [35] R. Hergt, S. Dutz, and M. Röder. “Effects of size distribution on hysteresis losses of magnetic nanoparticles for hyperthermia”. In: *Journal of Physics: Condensed Matter* 20.38 (2008), p. 385214 (cit. on p. 23).
- [36] M. Cobianchi, A. Guerrini, M. Avolio, C. Innocenti, M. Corti, P. Arosio, F. Orsini, C. Sangregorio, and A. Lascialfari. “Experimental determination of the frequency and field dependence of Specific Loss Power in Magnetic Fluid Hyperthermia”. In: *Journal of Magnetism and Magnetic Materials* 444 (2017), pp. 154–160 (cit. on p. 24).
- [37] A. Cervadoro, C. Giverso, R. Pande, S. Sarangi, L. Preziosi, J. Wosik, A. Brazdeikis, and P. Decuzzi. “Design Maps for the Hyperthermic Treatment of Tumors with Superparamagnetic Nanoparticles”. In: *PLoS ONE* 8.2 (2013), e57332 (cit. on p. 26).
- [38] R. Wildeboer, P. Southern, and Q. Pankhurst. “On the reliable measurement of specific absorption rates and intrinsic loss parameters in magnetic hyperthermia materials”. In: *Journal of Physics D: Applied Physics* 47.49 (2014), p. 495003 (cit. on p. 26).
- [39] E. Natividad, M. Castro, and A. Mediano. “Accurate measurement of the specific absorption rate using a suitable adiabatic magnetothermal setup”. In: *Applied Physics Letters* 92.9 (2008), p. 093116 (cit. on p. 27).
- [40] S. Huang, S. Wang, A. Gupta, D. Borca-Tasciuc, and S. Salon. “On the measurement technique for specific absorption rate of nanoparticles in an alternating electromagnetic field”. In: *Measurement Science and Technology* 23.3 (2012), p. 035701 (cit. on p. 27).
- [41] *RADIOMAG cost action TD1402*: <https://www.cost.eu/actions/TD1402/> (cit. on p. 27).
- [42] S. Dutz and R. Hergt. “Magnetic nanoparticle heating and heat transfer on a microscale: Basic principles, realities and physical limitations of hyperthermia for tumour therapy”. In: *International Journal of Hyperthermia* 29.8 (2013), pp. 790–800 (cit. on p. 27).
- [43] R. E. Rosensweig. “Heating magnetic fluid with alternating magnetic field”. In: *Journal of magnetism and magnetic materials* 252 (2002), pp. 370–374 (cit. on p. 27).
- [44] Y. Cheng, S. Weng, L. Yu, N. Zhu, M. Yang, and Y. Yuan. “The role of hyperthermia in the multidisciplinary treatment of malignant tumors”. In: *Integrative cancer therapies* 18 (2019), p. 1534735419876345 (cit. on p. 29).

- [45] C. Rumenapp, B. Gleich, and A. Haase. "Magnetic nanoparticles in magnetic resonance imaging and diagnostics". In: *Pharmaceutical research* 29.5 (2012), pp. 1165–1179 (cit. on p. 31).
- [46] S. Laurent, D. Forge, M. Port, A. Roch, C. Robic, L. Vander Elst, and R. N. Muller. "Magnetic iron oxide nanoparticles: synthesis, stabilization, vectorization, physicochemical characterizations, and biological applications". In: *Chemical reviews* 108.6 (2008), pp. 2064–2110 (cit. on pp. 38, 39).
- [47] A. Roch, R. N. Muller, and P. Gillis. "Theory of proton relaxation induced by superparamagnetic particles". In: *The Journal of chemical physics* 110.11 (1999), pp. 5403–5411 (cit. on p. 40).
- [48] R. A. El Shafie, D. Habermehl, S. Rieken, A. Mairani, L. Orschiedt, S. Brons, T. Haberer, K. J. Weber, J. Debus, and S. E. Combs. "In vitro evaluation of photon and raster-scanned carbon ion radiotherapy in combination with gemcitabine in pancreatic cancer cell lines". In: *Journal of Radiation Research* 54.suppl\\_1 (2013), pp. i113–i119 (cit. on pp. 44, 69).
- [49] R. Ludwig, F. J. Teran, U. Teichgraeber, and I. Hilger. "Nanoparticle-based hyperthermia distinctly impacts production of ROS, expression of Ki-67, TOP2A, and TPX2, and induction of apoptosis in pancreatic cancer". In: *International journal of nanomedicine* 12 (2017), p. 1009 (cit. on p. 44).
- [50] S. I. Eidelman and B. A. Shwartz. "Interactions of particles and radiation with matter". In: *Handbook of Particle Detection and Imaging* (2012), pp. 4–23 (cit. on p. 45).
- [51] A. L. Stockham, A. Wilkinson, and A. D. Singh. "Principles of Radiation Therapy". In: *Clinical Ophthalmic Oncology*. Springer, 2019, pp. 107–115 (cit. on p. 45).
- [52] M. Gazda and R. Lawrence. "Principles of radiation therapy, Cancer management: a multidisciplinary approach". In: *Ann Arbor: The University of Michigan* (2001) (cit. on p. 45).
- [53] E. B. Podgorsak. "External photon beams: Physical aspects". In: *Radiation Oncology Physics: A handbook for teachers and students*. Vienna: IAEA (2005), p. 169 (cit. on pp. 45, 47).
- [54] G. Battistoni, I. Mattei, and S. Muraro. "Nuclear physics and particle therapy". In: *Advances in Physics: X* 1.4 (2016), pp. 661–686 (cit. on p. 48).
- [55] J. F. Ziegler. "Stopping of energetic light ions in elemental matter". In: *Journal of Applied Physics* 85.3 (1999), pp. 1249–1272 (cit. on p. 48).

- [56] D. Schardt, T. Elsässer, and D. Schulz-Ertner. “Heavy-ion tumor therapy: Physical and radiobiological benefits”. In: *Reviews of Modern Physics* 82.1 (2010), pp. 383–425 (cit. on p. 49).
- [57] R. A. Grün. “Impact of tissue specific parameters on the prediction of the biological effectiveness for treatment planning in ion beam therapy”. In: (2014) (cit. on pp. 49, 52).
- [58] V. Marx. “Sharp shooters”. In: *Nature* 508.7494 (2014), pp. 133–138 (cit. on p. 50).
- [59] D. Schulz-Ertner and H. Tsujii. “Particle radiation therapy using proton and heavier ion beams”. In: *Journal of clinical oncology* 25.8 (2007), pp. 953–964 (cit. on p. 50).
- [60] B. S. Sørensen, J. Overgaard, and N. Bassler. “In vitro RBE-LET dependence for multiple particle types”. In: *Acta oncologica* 50.6 (2011), pp. 757–762 (cit. on p. 51).
- [61] S. J. McMahon. “The linear quadratic model: usage, interpretation and challenges”. In: *Physics in Medicine & Biology* 64.1 (2018), 01TR01 (cit. on p. 51).
- [62] J. Thariat, S. Valable, C. Laurent, S. Haghdoost, E. A. Pérès, M. Bernaudin, F. Sichel, P. Lesueur, M. Césaire, E. Petit, et al. “Hadron-therapy Interactions in Molecular and Cellular Biology”. In: *International journal of molecular sciences* 21.1 (2020), p. 133 (cit. on p. 52).
- [63] S. V. Spirou, S. A. Costa Lima, P. Bouziotis, S. Vranješ-Djurić, E. K. Efthimiadou, A. Laurenzana, A. I. Barbosa, I. Garcia-Alonso, C. Jones, D. Jankovic, et al. “Recommendations for in vitro and in vivo testing of magnetic nanoparticle hyperthermia combined with radiation therapy”. In: *Nanomaterials* 8.5 (2018), p. 306 (cit. on p. 53).
- [64] S. V. Spirou, M. Basini, A. Lascialfari, C. Sangregorio, and C. Innocenti. “Magnetic hyperthermia and radiation therapy: Radiobiological principles and current practice”. In: *Nanomaterials* 8.6 (2018), pp. 1–22 (cit. on p. 53).
- [65] N. R. Datta, S. G. Ordóñez, U. S. Gaipl, M. M. Paulides, H. Crezee, J. Gellermann, D. Marder, E. Puric, and S. Bodis. “Local hyperthermia combined with radiotherapy and-/or chemotherapy: Recent advances and promises for the future”. In: *Cancer Treatment Reviews* 41.9 (2015), pp. 742–753 (cit. on p. 53).
- [66] S. Dharmiah, J. Zeng, V. S. Rao, Z. Ouyang, T. Ma, K. Yu, H. Bhatt, C. Shah, A. Godley, P. Xia, et al. “Clinical and dosimetric evaluation of recurrent breast cancer patients treated with hyperthermia and radiation”. In: *International Journal of Hyperthermia* 36.1 (2019), pp. 985–991 (cit. on p. 53).



- [67] P. B. Elming, B. S. Sørensen, A. L. Oei, N. A. Franken, J. Crezee, J. Overgaard, and M. R. Horsman. "Hyperthermia: the optimal treatment to overcome radiation resistant hypoxia". In: *Cancers* 11.1 (2019), p. 60 (cit. on p. 53).
- [68] J. van der Zee. "Heating the patient: A promising approach?" In: *Annals of Oncology* 13.8 (2002), pp. 1173–1184 (cit. on p. 53).
- [69] G. F. Baronzio and E. D. Hager. *Hyperthermia in Cancer Treatment: A Primer*. 2006 (cit. on p. 53).
- [70] J. Overgaard. "Simultaneous and sequential hyperthermia and radiation treatment of an experimental tumor and its surrounding normal tissue in vivo". In: *International Journal of Radiation Oncology Biology Physics* 6.11 (1980), pp. 1507–1517 (cit. on p. 53).
- [71] J. C. Lin and M. F. Lin. "Microwave Hyperthermia-Induced Blood-Brain Barrier Alterations". In: *Radiation Research* 89.1 (1982), pp. 77–87 (cit. on p. 53).
- [72] B. Prasad, S. Kim, W. Cho, J. K. Kim, Y. A. Kim, S. Kim, and H. G. Wu. "Quantitative Estimation of the Equivalent Radiation Dose Escalation using Radiofrequency Hyperthermia in Mouse Xenograft Models of Human Lung Cancer". In: *Scientific Reports* 9.1 (2019), pp. 1–10 (cit. on p. 53).
- [73] A. Di Mari, S. Rametta Giuliano, E. Lanteri, et al. "Clinical use of high-intensity focused ultrasound in the management of different solid tumors". In: *WCRJ* 1 (2014), e295 (cit. on p. 53).
- [74] X. Liang, J. Gao, L. Jiang, J. Luo, L. Jing, X. Li, Y. Jin, and Z. Dai. "Nanohybrid liposomal cerasomes with good physiological stability and rapid temperature responsiveness for high intensity focused ultrasound triggered local chemotherapy of cancer". In: *ACS Nano* 9.2 (2015), pp. 1280–1293 (cit. on p. 53).
- [75] M. Abe, M. Hiraoka, M. Takahashi, S. Egawa, C. Matsuda, Y. Onoyama, K. Morita, M. Kakehi, and T. Sugahara. "Multi-institutional studies on hyperthermia using an 8-MHz radiofrequency capacitive heating device (thermotron RF-8) in combination with radiation for cancer therapy". In: *Cancer* 58.8 (1986), pp. 1589–1595 (cit. on p. 53).
- [76] A. Muller, Gerhard J and Roggan. *Laser-induced interstitial thermotherapy*. 1995 (cit. on p. 53).
- [77] P. Guardia, R. Di Corato, L. Lartigue, C. Wilhelm, A. Espinosa, M. Garcia-Hernandez, F. Gazeau, L. Manna, and T. Pellegrino. "Water-soluble iron oxide nanocubes with high values of specific absorption rate for cancer cell hyperthermia treatment". In: *ACS Nano* 6.4 (2012), pp. 3080–3091 (cit. on p. 53).

- [78] E. A. Perigo, G. Hemery, O. Sandre, D. Ortega, E. Garaio, F. Plazaola, and F. J. Teran. "Fundamentals and advances in magnetic hyperthermia". In: *Applied Physics Reviews* 2.4 (2015), p. 041302 (cit. on p. 53).
- [79] Z. W. Tay, P. Chandrasekharan, A. Chiu-Lam, D. W. Hensley, R. Dhavalikar, X. Y. Zhou, E. Y. Yu, P. W. Goodwill, B. Zheng, C. Rinaldi, and S. M. Conolly. "Magnetic Particle Imaging-Guided Heating in Vivo Using Gradient Fields for Arbitrary Localization of Magnetic Hyperthermia Therapy". In: *ACS Nano* 12.4 (2018), pp. 3699–3713 (cit. on p. 53).
- [80] D. Cabrera, A. Coene, J. Leliaert, E. J. Artés-Ibáñez, L. Dupré, N. D. Telling, and F. J. Teran. "Dynamical Magnetic Response of Iron Oxide Nanoparticles Inside Live Cells". In: *ACS Nano* 12.3 (2018), pp. 2741–2752 (cit. on p. 53).
- [81] J. Pan, P. Hu, Y. Guo, J. Hao, D. Ni, Y. Xu, Q. Bao, H. Yao, C. Wei, Q. Wu, and J. Shi. "Combined Magnetic Hyperthermia and Immune Therapy for Primary and Metastatic Tumor Treatments". In: *ACS nano* 14.1 (2020), pp. 1033–1044 (cit. on p. 53).
- [82] D. Niculaes, A. Lak, G. C. Anyfantis, S. Marras, O. Laslett, S. K. Avugadda, M. Cassani, D. Serantes, O. Hovorka, R. Chantrell, and T. Pellegrino. "Asymmetric Assembling of Iron Oxide Nanocubes for Improving Magnetic Hyperthermia Performance". In: *ACS Nano* 11.12 (2017), pp. 12121–12133 (cit. on p. 53).
- [83] A. Espinosa, R. Di Corato, J. Kolosnjaj-Tabi, P. Flaud, T. Pellegrino, and C. Wilhelm. "Duality of Iron Oxide Nanoparticles in Cancer Therapy: Amplification of Heating Efficiency by Magnetic Hyperthermia and Photothermal Bimodal Treatment". In: *ACS Nano* 10.2 (2016), pp. 2436–2446 (cit. on p. 53).
- [84] C. Xu, Y. Zheng, W. Gao, J. Xu, G. Zuo, Y. Chen, M. Zhao, J. Li, J. Song, N. Zhang, Z. Wang, H. Zhao, and Z. Mei. "Magnetic Hyperthermia Ablation of Tumors Using Injectable Fe<sub>3</sub>O<sub>4</sub>/Calcium Phosphate Cement". In: *ACS Applied Materials and Interfaces* 7.25 (2015), pp. 13866–13875 (cit. on p. 53).
- [85] J. C. Peeken, P. Vaupel, and S. E. Combs. "Integrating hyperthermia into modern radiation oncology: What evidence is necessary?" In: *Frontiers in Oncology* 7 (2017), p. 132 (cit. on p. 53).
- [86] N. R. Datta, S. Krishnan, D. E. Speiser, E. Neufeld, N. Kuster, S. Bodis, and H. Hofmann. "Magnetic nanoparticle-induced hyperthermia with appropriate payloads: Paul Ehrlich's "magic (nano)bullet" for cancer theranostics?" In: *Cancer Treatment Reviews* 50 (2016), pp. 217–227 (cit. on p. 53).



- [87] N. R. Datta, R. Schneider, E. Puric, F. J. Ahlhelm, D. Marder, S. Bodis, and D. C. Weber. "Proton Irradiation with Hyperthermia in Unresectable Soft Tissue Sarcoma". In: *International Journal of Particle Therapy* 3.2 (2016), pp. 327–336 (cit. on pp. 53, 70).
- [88] J. Maeda, Y. Fujii, H. Fujisawa, H. Hirakawa, I. M. Cartwright, M. Uesaka, H. Kitamura, A. Fujimori, and T. A. Kato. "Hyperthermia-induced radiosensitization in CHO wild-type, NHEJ repair mutant and HR repair mutant following proton and carbon-ion exposure". In: *Oncology Letters* 10.5 (2015), pp. 2828–2834 (cit. on pp. 53, 70, 71).
- [89] S. Ahmad, H. Jin, K. Sahoo, R. Griffin, T. Herman, and A. Ranjan. "Proton Therapy in Combination With Mild Hyperthermia Enhances Killing of Radio-Resistant Hypoxic Tumor Cells". In: *International Journal of Radiation Oncology\*Biophysics* 99.2 (2017), E574 (cit. on p. 54).
- [90] S. Dong, Y. Chen, L. Yu, K. Lin, and X. Wang. "Magnetic Hyperthermia–Synergistic H<sub>2</sub>O<sub>2</sub> Self-Sufficient Catalytic Suppression of Osteosarcoma with Enhanced Bone-Regeneration Bioactivity by 3D-Printing Composite Scaffolds". In: *Advanced Functional Materials* 30.4 (2020), p. 1907071 (cit. on p. 54).
- [91] A. Ito, Y. Kuga, H. Honda, H. Kikkawa, A. Horiuchi, Y. Watanabe, and T. Kobayashi. "Magnetite nanoparticle-loaded anti-HER2 immunoliposomes for combination of antibody therapy with hyperthermia". In: *Cancer Letters* 212.2 (2004), pp. 167–175 (cit. on p. 54).
- [92] H. Etemadi and P. G. Plieger. "Magnetic Fluid Hyperthermia Based on Magnetic Nanoparticles: Physical Characteristics, Historical Perspective, Clinical Trials, Technological Challenges, and Recent Advances". In: *Advanced Therapeutics* 3.11 (2020), p. 2000061 (cit. on p. 56).
- [93] E. J. Hall, A. J. Giaccia, et al. *Radiobiology for the Radiologist*. Vol. 6. Philadelphia, 2006 (cit. on p. 57).
- [94] S. Kossatz, R. Ludwig, H. Dähring, V. Ettelt, G. Rimkus, M. Marciello, G. Salas, V. Patel, F. J. Teran, and I. Hilger. "High therapeutic efficiency of magnetic hyperthermia in xenograft models achieved with moderate temperature dosages in the tumor area". In: *Pharmaceutical research* 31.12 (2014), pp. 3274–3288 (cit. on p. 57).
- [95] T. L. Moore, L. Rodriguez-Lorenzo, V. Hirsch, S. Balog, D. Urban, C. Jud, B. Rothen-Rutishauser, M. Lattuada, and A. Petri-Fink. "Nanoparticle colloidal stability in cell culture media and impact on cellular interactions". In: *Chemical Society Reviews* 44.17 (2015), pp. 6287–6305 (cit. on p. 57).

- [96] A. A. Coelho. "Topas: General Profile and Structure Analysis Software for Powder Diffraction Data". In: *Bruker AXS*. 2005 (cit. on p. 58).
- [97] M. I. Dar and S. Shivashankar. "Single crystalline magnetite, maghemite, and hematite nanoparticles with rich coercivity". In: *RSC Advances* 4.8 (2014), pp. 4105–4113 (cit. on p. 60).
- [98] J. Ma, Z. Zhang, Z. Zhang, J. Huang, Y. Qin, X. Li, H. Liu, K. Yang, and G. Wu. "Magnetic nanoparticle clusters radiosensitise human nasopharyngeal and lung cancer cells after alternating magnetic field treatment". In: *International Journal of Hyperthermia* 31.7 (2015), pp. 800–812 (cit. on pp. 63, 71).
- [99] M. Calero, M. Chiappi, A. Lazaro-Carrillo, M. J. Rodríguez, F. J. Chichón, K. Crosbie-Staunton, A. Prina-Mello, Y. Volkov, A. Villanueva, and J. L. Carrascosa. "Characterization of interaction of magnetic nanoparticles with breast cancer cells". In: *Journal of nanobiotechnology* 13.1 (2015), pp. 1–15 (cit. on p. 63).
- [100] G. Hannon, A. Bogdanska, Y. Volkov, and A. Prina-Mello. "Comparing the Effects of Intracellular and Extracellular Magnetic Hyperthermia on the Viability of BxPC-3 Cells". In: *Nanomaterials* 10.3 (2020), p. 593 (cit. on p. 66).
- [101] K. Mahmoudi, A. Bouras, D. Bozec, R. Ivkov, and C. Hadjipanayis. "Magnetic hyperthermia therapy for the treatment of glioblastoma: a review of the therapy's history, efficacy and application in humans". In: *International Journal of Hyperthermia* 34.8 (2018), pp. 1316–1328 (cit. on p. 66).
- [102] D. Habermehl, K. Ilicic, S. Dehne, S. Rieken, L. Orschiedt, S. Brons, T. Haberer, K. J. Weber, J. Debus, and S. E. Combs. "The relative biological effectiveness for carbon and oxygen ion beams using the raster-scanning technique in hepatocellular carcinoma cell lines". In: *PLoS ONE* 9.12 (2014), e113591 (cit. on p. 69).
- [103] S. E. Combs, L. Zipp, S. Rieken, D. Habermehl, S. Brons, M. Winter, T. Haberer, J. Debus, and K. J. Weber. "In vitro evaluation of photon and carbon ion radiotherapy in combination with chemotherapy in glioblastoma cells". In: *Radiation Oncology* 7.1 (2012), pp. 1–6 (cit. on p. 69).
- [104] X. Cui, K. Oonishi, H. Tsujii, T. Yasuda, Y. Matsumoto, Y. Furusawa, M. Akashi, T. Kamada, and R. Okayasu. "Effects of carbon ion beam on putative colon cancer stem cells and its comparison with x-rays". In: *Cancer Research* 71.10 (2011), pp. 3676–3687 (cit. on p. 69).

- [105] S. Dutz and R. Hergt. "Magnetic particle hyperthermia—a promising tumour therapy?" In: *Nanotechnology* 25.45 (2014), p. 452001 (cit. on p. 69).
- [106] K. Oonishi, X. Cui, H. Hirakawa, A. Fujimori, T. Kamijo, S. Yamada, O. Yokosuka, and T. Kamada. "Different effects of carbon ion beams and X-rays on clonogenic survival and DNA repair in human pancreatic cancer stem-like cells". In: *Radiotherapy and Oncology* 105.2 (2012), pp. 258–265 (cit. on p. 70).
- [107] M. Li, Q. Zhao, X. Yi, X. Zhong, G. Song, Z. Chai, Z. Liu, and K. Yang. "Au@MnS@ZnS Core/Shell/Shell Nanoparticles for Magnetic Resonance Imaging and Enhanced Cancer Radiation Therapy". In: *ACS Applied Materials and Interfaces* 8.15 (2016), pp. 9557–9564 (cit. on p. 70).
- [108] C. J. Liu, C. H. Wang, S. T. Chen, H. H. Chen, W. H. Leng, C. C. Chien, C. L. Wang, I. M. Kempson, Y. Hwu, T. C. Lai, M. Hsiao, C. S. Yang, Y. J. Chen, and G. Margaritondo. "Enhancement of cell radiation sensitivity by pegylated gold nanoparticles". In: *Physics in Medicine and Biology* 55.4 (2010), p. 931 (cit. on p. 70).
- [109] X. Wang, C. Zhang, J. Du, X. Dong, S. Jian, L. Yan, Z. Gu, and Y. Zhao. "Enhanced Generation of Non-Oxygen Dependent Free Radicals by Schottky-type Heterostructures of Au-Bi<sub>2</sub>S<sub>3</sub> Nanoparticles via X-ray-Induced Catalytic Reaction for Radiosensitization". In: *ACS Nano* 13.5 (2019), pp. 5947–5958 (cit. on p. 70).
- [110] S. Goel, D. Ni, and W. Cai. "Harnessing the Power of Nanotechnology for Enhanced Radiation Therapy". In: *ACS Nano* 11.6 (2017), pp. 5233–5237 (cit. on p. 70).
- [111] A. Oei, H. Kok, S. Oei, M. Horsman, L. Stalpers, N. Franken, and J. Crezee. "Molecular and biological rationale of hyperthermia as radio- and chemosensitizer". In: *Advanced drug delivery reviews* 163 (2020), pp. 84–97 (cit. on pp. 72, 73).
- [112] A. L. Oei, L. E. Vriend, J. Crezee, N. A. Franken, and P. M. Krawczyk. "Effects of hyperthermia on DNA repair pathways: one treatment to inhibit them all". In: *Radiation Oncology* 10.1 (2015), pp. 1–13 (cit. on p. 73).
- [113] J. Wahsner, E. M. Gale, A. Rodríguez-Rodríguez, and P. Caravan. "Chemistry of MRI contrast agents: current challenges and new frontiers". In: *Chemical reviews* 119.2 (2018), pp. 957–1057 (cit. on p. 76).

- [114] M. A. González-Gómez, S. Belderbos, S. Yañez-Vilar, Y. Piñeiro, F. Cleeren, G. Bormans, C. M. Deroose, W. Gsell, U. Himmelreich, and J. Rivas. “Development of superparamagnetic nanoparticles coated with polyacrylic acid and aluminum hydroxide as an efficient contrast agent for multimodal imaging”. In: *Nanomaterials* 9.11 (2019), p. 1626 (cit. on p. 77).
- [115] M. F. Casula, P. Floris, C. Innocenti, A. Lascialfari, M. Marinone, M. Corti, R. A. Sperling, W. J. Parak, and C. Sangregorio. “Magnetic resonance imaging contrast agents based on iron oxide superparamagnetic ferrofluids”. In: *Chemistry of Materials* 22.5 (2010), pp. 1739–1748 (cit. on p. 77).
- [116] M. Basini, A. Guerrini, M. Cobianchi, F. Orsini, D. Bettega, M. Avolio, C. Innocenti, C. Sangregorio, A. Lascialfari, and P. Arosio. “Tailoring the magnetic core of organic-coated iron oxides nanoparticles to influence their contrast efficiency for Magnetic Resonance Imaging”. In: *Journal of Alloys and Compounds* 770 (2019), pp. 58–66 (cit. on pp. 77, 88, 90).
- [117] T. Orlando, M. Albino, F. Orsini, C. Innocenti, M. Basini, P. Arosio, C. Sangregorio, M. Corti, and A. Lascialfari. “On the magnetic anisotropy and nuclear relaxivity effects of Co and Ni doping in iron oxide nanoparticles”. In: *Journal of Applied Physics* 119.13 (2016), p. 134301 (cit. on p. 77).
- [118] N. J. Johnson, S. He, V. A. Nguyen Huu, and A. Almutairi. “Compact micellization: a strategy for Ultrahigh T<sub>1</sub> magnetic resonance contrast with gadolinium-based nanocrystals”. In: *ACS nano* 10.9 (2016), pp. 8299–8307 (cit. on p. 77).
- [119] J. Fresnais, Q. Ma, L. Thai, P. Porion, P. Levitz, and A.-L. Rollet. “NMR relaxivity of coated and non-coated size-sorted maghemite nanoparticles”. In: *Molecular Physics* 117.7-8 (2019), pp. 990–999 (cit. on p. 77).
- [120] T. Vangijzegem, D. Stanicki, A. Panepinto, V. Socoliuc, L. Vekas, R. N. Muller, and S. Laurent. “Influence of experimental parameters of a continuous flow process on the properties of very small iron oxide nanoparticles (VSION) designed for T<sub>1</sub>-weighted magnetic resonance imaging (MRI)”. In: *Nanomaterials* 10.4 (Apr. 2020), p. 757 (cit. on p. 77).
- [121] S. L. Pinho, S. Laurent, J. Rocha, A. Roch, M.-H. Delville, S. Mornet, L. D. Carlos, L. Vander Elst, R. N. Muller, and C. F. Geraldes. “Relaxometric studies of  $\gamma$ -Fe<sub>2</sub>O<sub>3</sub>@SiO<sub>2</sub> core shell nanoparticles: when the coating matters”. In: *The Journal of Physical Chemistry C* 116.3 (2012), pp. 2285–2291 (cit. on p. 77).

- [122] M. Magro and F. Vianello. “Bare iron oxide nanoparticles: Surface tunability for biomedical, sensing and environmental applications”. In: *Nanomaterials* 9.11 (2019), p. 1608 (cit. on p. 77).
- [123] F. Brero, M. Basini, M. Avolio, F. Orsini, P. Arosio, C. Sangregorio, C. Innocenti, A. Guerrini, J. Boucard, E. Ishow, et al. “Coating Effect on the  $^1\text{H}$ —NMR Relaxation Properties of Iron Oxide Magnetic Nanoparticles”. In: *Nanomaterials* 10.9 (2020), p. 1660 (cit. on p. 77).
- [124] C. Linot, J. Poly, J. Boucard, D. Pouliquen, S. Nedellec, P. Hulin, N. Marec, P. Arosio, A. Lascialfari, A. Guerrini, C. Sangregorio, M. Lecouvey, L. Lartigue, C. Blanquart, and E. Ishow. “PEGylated Anionic Magnetofluorescent Nanoassemblies: Impact of Their Interface Structure on Magnetic Resonance Imaging Contrast and Cellular Uptake”. In: *ACS Applied Materials and Interfaces* 9.16 (2017), pp. 14242–14257 (cit. on p. 79).
- [125] A. Faucon, T. Maldiney, O. Clément, P. Hulin, S. Nedellec, M. Robard, N. Gautier, E. De Meulenaere, K. Clays, T. Orlando, et al. “Highly cohesive dual nanoassemblies for complementary multi-scale bioimaging”. In: *Journal of Materials Chemistry B* 2.44 (2014), pp. 7747–7755 (cit. on p. 79).
- [126] C. Ménager, O. Sandre, J. Mangili, and V. Cabuil. “Preparation and swelling of hydrophilic magnetic microgels”. In: *Polymer* 45.8 (2004), pp. 2475–2481 (cit. on p. 79).
- [127] J. Santoyo Salazar, L. Perez, O. De Abril, L. Truong Phuoc, D. Ihiwakrim, M. Vazquez, J. M. Greneche, S. Begin-Colin, and G. Pourroy. “Magnetic iron oxide nanoparticles in 10-40 nm range: Composition in terms of magnetite/maghemite ratio and effect on the magnetic properties”. In: *Chemistry of Materials* 23.6 (2011), pp. 1379–1386 (cit. on p. 79).
- [128] S. Lefebure, E. Dubois, V. Cabuil, S. Neveu, and R. Massart. “Monodisperse magnetic nanoparticles: preparation and dispersion in water and oils”. In: *Journal of Materials research* 13.10 (1998), pp. 2975–2981 (cit. on p. 79).
- [129] E. D. Smolensky, H.-Y. E. Park, Y. Zhou, G. A. Rolla, M. Marjańska, M. Botta, and V. C. Pierre. “Scaling laws at the nanosize: the effect of particle size and shape on the magnetism and relaxivity of iron oxide nanoparticle contrast agents”. In: *Journal of Materials Chemistry B* 1.22 (2013), pp. 2818–2828 (cit. on p. 87).
- [130] E. Umut. “Surface modification of nanoparticles used in biomedical applications”. In: *Modern Surface Engineering Treatments* 20 (2013), pp. 185–208 (cit. on p. 88).